PhD Dissertation

International Doctorate School in Information and Communication Technologies

DISI - University of Trento

3D CAMERA BASED ON GAIN-MODULATED CMOS AVALANCHE PHOTODIODES

Olga Shcherbakova

Advisor:

Prof. Gian-Franco Dalla Betta

Università degli Studi di Trento

Co-Advisor:

Dr. Lucio Pancheri

Università degli Studi di Trento, Fondazione Bruno Kessler

April 2013

Abstract

In the last several years, both scientific and industrial community have shown an increasing interest in range imaging due to its potential use in various application domains such as robotics, vehicle safety, gaming, mobile applications as well as many others. Among the diversity of techniques available for range detection, Time-of-Flight (TOF) offers advantages in terms of compact system realization, good performance and low required computational power. Recent works have shown a trend towards higher resolutions, with a consequent reduction of pixel size, higher modulation frequencies and demodulation contrast to allow a higher distance precision.

In this thesis we propose a new concept of range camera exploiting linear-mode avalanche photodiodes as in-pixel demodulating detectors. Due to photocurrent gain modulation, avalanche photodiodes can combine optical sensing and light signal demodulation in a single device. The main advantage of the avalanche photodiode implementation is the possibility to operate at high frequencies due to its very wide bandwidth that, in turn, influences the precision in distance measurement.

In a first stage, the concept was experimentally validated on single pixel structures. These measurement results encouraged the implementation of a time-of-flight image sensor. A 64×64 pixel array has been designed and fabricated in a $0.35\mu m$ *standard CMOS technology. The pixel pitch is 30μm with a fill-factor of 25.7%. Demodulation contrast exceeds 85% at 25MHz modulation frequency. A 3D camera system demonstrates best precision of 1.9cm and a 3D frame rate of 200fps. Additional tests performed on single pixels have shown demodulation contrast as high as 80% measured at 200MHz modulation frequency.*

Keywords

[3D imaging, Indirect Time-of-Flight, Phase-shift Time-of-Flight, CMOS Avalanche Photodiode, Linear-mode Avalanche Photodiode, Gain-modulated Avalanche Photodiode]

List of Abbreviations

APD	Avalanche Photodiode
CAPD	Current Assisted Photonic Demodulator
CCD	Charge-Coupled Device
CDS	Correlation Double Sampling
CIS	CMOS Image Sensor
CMOS	Complementary Metal Oxide Semiconductor
CSA	Charge Sensitive Amplifier
DDS	Double-Delta Sampling
D-TOF	Direct Time-of-Flight
IR	Infra-Red
IS	Image Sensor
I-TOF	Indirect Time-of-Flight
FPN	Fixed Pattern Noise
LED	Light-Emitting Diode
PMT	Photomultiplier Tube
SPAD	Single Photon Avalanche Diode
TOF	Time-of-Flight

Contents

1 Introduction **1**

1.1 The Context 1

1.2 The Problem 3

1.3 The Solution 3

1.4 Innovative Aspects 4

1.5 Structure of the Thesis 4

1.6 List of Publications 6

2 State of the Art in 3D Imaging **7**

2.1 Active distance measurement 9

2.1.1 Active triangulation 9

2.1.2 Interferometry 11

2.1.3 Time-of-Flight 12

2.2 Demodulating image sensors 17

2.2.1 Photogate-based demodulator 20

2.2.2 Current Assisted Photonic Demodulator 25

2.2.3 Pinned photodiode demodulator 27

2.2.4 Static drift field device 31

2.3 Summary 32

3 Avalanche Photodiode **35**

3.1 APD Introduction 35
3.1.1 Avalanche photodiode 35
3.1.2 Operation principle of linear-mode APD 37
3.2 Related work on APDs 38
3.3 CMOS APD implementation and characterization 42
3.4 CMOS APD application for Indirect TOF measurement 45

4 Test Pixel **51**
4.1 Phase sensitive pixel 51
4.1.1 Operation principle 52
4.1.2 Phase sensitive pixel design 53
4.2 Experimental results 59
4.2.1 Equipment 59
4.2.2 Measurements with constant light 60
4.2.3 Phase shift measurement 63
4.3 Conclusion 75

5 APD Image Sensor **77**
5.1 APD pixel 77
5.1.1 Pixel design 78
5.1.2 Pixel simulation 80
5.1.3 Pixel layout 85
5.2 APD sensor design 86
5.3 Experimental results 88
5.3.1 Setup description 89
5.3.2 General sensor characterization 91
5.3.3 Distance measurement 97

6 APD-based 3D Camera Prototype **103**

7 Conclusion **111**

7.1 Summary 112

7.2 Future work 113

Bibliography **114**

List of Tables

2.1 Performance Comparison of Different Types of Demodulating Sensors 34

3.1 Selected characteristics of available CMOS APDs 40

4.1 Main characteristics of CMOS APD used in the pixel . . . 54
4.2 In-pixel Amplifier Characteristics 55
4.3 Phase Sensitive Pixel Characteristics 58
4.4 Measurement Equipment 59
4.5 Pixel and Illuminantor Settings 64
4.6 APD and LED settings 68
4.7 APD and LED settings at 100MHz 72

5.1 In-pixel Amplifier Characteristics 80
5.2 Pixel Summary 85
5.3 Pixel Characteristics 97
5.4 Sensor Characteristics 97
5.5 Camera System Characteristics 101

6.1 3D Camera Prototype Summary 109

List of Figures

2.1 Main range detection techniques 8
2.2 Active triangulation distance measurement 10
2.3 Interferometry distance measurement 12
2.4 TOF principle 13
2.5 Main TOF techniques 14
2.6 Phase-shift illustration 15
2.7 Frequency Modulated Continuous Wave distance detection principle 17
2.8 Voltage dependence on the phase difference between light signal and demodulation signal 18
2.9 Cross sectional view of the CCD part of a pixel 21
2.10 Example of 3D camera produced by Mesa Imaging company 22
2.11 Simplified PMD structure and modulation principle of the device 23
2.12 Examples of 3D camera system provided by PMDtechnologies company 24
2.13 Schematic cross section of Current Assistent Photonic Demodulator 25
2.14 Examples of 3D camera system produced by SoftKinetic company 26

2.15 Cross-section of a photo-demodulator based on a standard pinned photodiode and modified pinned photodiode with corresponding energy band diagrams 28
2.16 Conceptual diagram of 2D and 3D frames acquisition and a simplified layout of photodiodes and transfer gates in 2 × 2 pixels 29
2.17 Sensor architecture with pixels arrangement 30
2.18 Static drift field pixel 31

3.1 Current-voltage and gain-voltage characteristic of a photodiode 36
3.2 Noise factor as a function of multiplication gain 43
3.3 Schematic cross section of the APD border 44
3.4 Gain uniformity characteristic of $0.35\mu m$ CMOS APDs fabricated on the same die and on different dies in the same production batch 44
3.5 Linear-mode APD gain modulation 46
3.6 APD operation 47
3.7 Average output current dependence on the phase difference between light signal and modulation signal 48

4.1 Block diagram of the phase sensitive pixel 52
4.2 CMOS APD cross section 54
4.3 Charge sensitive amplifier circuit 55
4.4 Simulation results of a phase sensitive pixel 57
4.5 Phase sensitive pixel layout and microphotograph 58
4.6 Phase sensitive pixel measurement setup 60
4.7 Phase sensitive pixel measurement in light and dark conditions 61
4.8 Phase sensitive pixel measurement of SNR 61
4.9 Output voltage noise as a function of output signal 62

4.10 Set-up for phase delay measurement 63
4.11 The output signals observed on an oscilloscope 65
4.12 Output voltage dependence on time delay between optical and electrical modulation signals 66
4.13 Phase sensitive pixel measurement setup 67
4.14 Phase sensitive pixel measurement of output dependence on time delay at 50MHz 68
4.15 Phase sensitive pixel measurement of output voltage dependence on DC bias voltage of APD for two time delays . . . 70
4.16 Phase sensitive pixel measurement at 50MHz: a - demodulation contrast as a function of applied DC bias voltage of APD; b - SNR of demodulated amplitude as a function of applied DC bias voltage of APD 71
4.17 Phase sensitive pixel measurement of output dependence on time delay at 100MHz 73
4.18 Phase sensitive pixel measurement at 100MHz: a - demodulation contrast as a function of applied DC bias voltage of APD; b - SNR of demodulated amplitude as a function of applied DC bias voltage of APD 74

5.1 In-pixel differential amplifier 79
5.2 Pixel schematic 79
5.3 APD simulation model 81
5.4 APD pixel simulation: a - transient simulation, b - output dependence on the phase shift 83
5.5 Final pixel schematic 84
5.6 Pixel layout 86
5.7 Sensor schematic 87
5.8 First readout mode: timing diagram for normal acquisition 88

5.9 Second readout mode: timing diagram for double acquisition 88
5.10 Chip micrograph 89
5.11 The scheme for the modulation circuit 90
5.12 The scheme for the DC bias voltage 90
5.13 Sensor measurement with ultraviolet LED 91
5.14 Sensor measurement of SNR in light and dark conditions . 92
5.15 Dark current distribution 93
5.16 Dark current dependence on APD bias voltage 93
5.17 PRNU measurement 94
5.18 Sensor measurement at 25MHz: a - demodulation contrast as a function of applied DC bias voltage of APD; b - SNR of demodulated amplitude as a function of applied DC bias voltage of APD 95
5.19 Demodulation contrast of single pixels at 200MHz modulation frequency 96
5.20 a - measurement setup, b - setup photograph 98
5.21 Distance measurement as a function of the distance to a plain white target 99
5.22 Distance precision as a function of the distance to a plain white target 100
5.23 2D, 3D images and image histograms 101

6.1 3D camera prototype block diagram 104
6.2 Prototype examples of 3D image: a - 3D image, b - 2D image 106
6.3 Demonstration of a 3D video 107
6.4 Demonstration of a 2D video 107
6.5 Demonstration of a video clip about 3D camera 108
6.6 3D camera system prototype 110

Chapter 1

Introduction

In this chapter the context of the thesis work will be discussed together with a short description of the problem and proposed solution. In addition, the innovative aspects of the work will be highlighted and the structure of the thesis will be listed.

1.1 The Context

Contactless distance measurement has become increasingly popular nowadays. The application spectrum for remote ranging systems is very broad, diverse and constantly growing. It starts from robotics [1],[2], where contactless distance measurement is used in autonomous navigation and collision avoidance, which is also relevant in autonomous vehicle driving and industrial control [3],[4]. Other application examples include entertainment, security and surveillance, biomedical applications and many others [5],[6],[7],[8].

There are various different techniques for distance measurement, they all have specific application focus and thus different characteristics. In general, range measuring techniques can be divided into three groups: optical, microwave and ultrasonic. Optical range measurement, onto which this thesis is focused, can offer solid-state monolithic sensors with high range

resolution and high lateral resolution [9]. A further classification of optical distance measurement techniques separates active and passive methods. Passive optical methods use ambient light to measure the distance, thus they are sensitive to environment condition, such as illumination and contrast. In addition, they require high computational power for distance reconstruction. On the other hand, active optical methods offer a higher immunity to environment conditions by means of scene illumination with an active light source.

Active optical techniques can be divided in three categories: interferometry, triangulation and Time-of-Flight (TOF). This division is made according to operation principle, as a consequence these techniques have different range and precision performance [10]. With respect to other active ranging techniques, TOF method offers the best performance in terms of the system cost, reliability and acquisition time. Compared with interferometery, devices based on the TOF technique are less accurate, but they allow unambiguous measurements over larger distances and they are suitable for targets with diffuse reflection from a rough surface. A further classification in Time-of-Flight distance measurement method distinguishes between scanner and scannerless system techniques. A branching in scannerless side separates direct and indirect TOF methods. The overall block diagram of existing distance measurement techniques will be illustrated in Chapter 2.

The work described in this thesis is focused on Indirect Time-of-Flight technique. The implementation of a new photodetector for this method is investigated. The I-TOF sensor fabrication and 3D camera prototype development based on this photodetector demonstrate the proposed approach for a distance measurement application.

1.2 The Problem

Although several types of 3D camera systems are currently commercialized the improvement of some characteristics would open the way to a broad application of these devices. In particular, power consumption should be reduced in order for 3D cameras to be able to run on batteries and higher frame rate would allow a smoother range video capture of fast moving objects. Ambient light in outdoor operation is still an obstacle for most of available 3D cameras, as well as target reflection and scattering properties can cause certain problems for distance detection. There is always a demand in high precision, high spatial resolution and high fill factor.

Last but not the least, total system cost is very important factor. High prices of existing 3D camera solutions prevent their broad spreading in consumer market. It is also important to note that 3D cameras exploit lasers or IR LEDs for target illumination that can raise serious safety issues that also should be taken into account especially for consumer application market. This work addresses several of the above-mentioned problems, namely frame rate, precision and power consumption.

1.3 The Solution

In order to tackle the problems mentioned above and improve the existing 3D camera systems the application of CMOS avalanche photodiodes for TOF optical ranging has been investigated. There already exist scanning systems that utilize avalanche photodiodes fabricated in custom technologies. However, in this work we propose the monolithic implementation of avalanche photodiodes together with readout electronics fabricated in a standard CMOS process in order to reduce chip and system cost. In addition, we have implemented a sensor consisting of a pixel array, not a

single device, thus improving lateral resolution of a distance measurement system.

This research work has been carried out in collaboration with the Smart Optical Sensors and Interfaces (SOI) research unit of the Fondazione Bruno Kessler (FBK) in Trento, Italy. My main contributions have been in electro-optical characterization of single pixels, as well as the design and electro-optical characterization of the sensor based on an avalanche photodiode array. In addition, my tasks included the design and evaluation of a 3D camera prototype and measurement of sensor's performance.

1.4 Innovative Aspects

In this thesis a novel photodetector for distance measurement that can potentially lead to several improvements with respect to the state-of-art approaches is proposed. This photodetector is a CMOS avalanche photodiode working in a linear regime. The avalanche photodiode plays a role of photodetector and demodulator in a single device that performs mixing operation of optical signal and electrical signal required for Indirect Time-of-Flight distance measurement. We demonstrate for the first time a working TOF camera system prototype with a sensor based on an avalanche photodiode pixel array.

1.5 Structure of the Thesis

The remaining chapters of the dissertation are arranged as follows.

Chapter 2 briefly describes the state of the art in distance measurement techniques with particular focus on an Indirect Time-of-Flight measurement method. Then image sensors characteristics used in Indirect Time-Of-Flight measurement are analyzed. The main problems and drawbacks

of existing Time-Of-Flight sensor solutions are identified.

Chapter 3 introduces the proposed approach of avalanche photodiode application for TOF ranging. Avalanche photodiode theory, CMOS implementation and state-of-the-art on CMOS avalanche photodiode sensors are covered here. Furthermore, the working principle of APD-based TOF distance measurement is illustrated.

Chapter 4 reports on the electro-optical characterization of a single pixel structure, fabricated for a different application in high sensitivity imaging. Even though pixel design was not optimized for Time-of-Flight distance measurement, simulation and experimental results demonstrate the feasibility of the proposed approach.

Chapter 5 focuses on the implementation of a 64×64 pixel image sensor based on avalanche photodiodes in a standard CMOS technology. Details on pixel and sensor design are given next. Electro-optical measurements as well as distance measurements follow the discussion.

Chapter 6 describes the implementation of a 3D camera system prototype based on the fabricated sensor. The main constrains under prototype realization are described. Examples of 3D images and 3D videos illustrate the performance of the 3D camera.

Finally, a summary of the research work is presented in Chapter 7. The directions for future work and their discussion concludes the thesis.

1.6 List of Publications

- Pancheri, Lucio; Shcherbakova, Olga; Massari, Nicola; Dalla Betta, Gian-Franco and Stoppa, David, "Image sensors based on linear mode APDs: analysis and future perspectives," accepted for presentation at the International Image Sensor Workshop, Snowbird, Utah, June 2013

- Shcherbakova, Olga; Pancheri, Lucio; Dalla Betta, Gian-Franco; Massari, Nicola; Stoppa, David, "3D camera based on linear-mode gain-modulated avalanche photodiodes," Solid-State Circuits Conference Digest of Technical Papers (ISSCC), 2013 IEEE International , vol., no., pp.490,491, 17-21 Feb. 2013

- Shcherbakova, O.; Mittempergher, R.; Dalla Betta, G.-F.; Pancheri, L.; Stoppa, D., "Design and characterization of a monolithic CMOS phase-sensitive pixel based on an avalanche photodiode," Ph.D. Research in Microelectronics and Electronics (PRIME), 2011 7th Conference on , vol., no., pp.85,88, 3-7 July 2011

- Shcherbakova, Olga; Pancheri, Lucio; Massari, Nicola; Dalla Betta, Gian-Franco; Stoppa, David, "Linear-mode gain-modulated avalanche photodiode image sensor for TOF distance measurement," to be submitted to a journal

Chapter 2

State of the Art in 3D Imaging

The real world has three spatial dimensions and we as human beings are able to distinguish distances through stereoscopic vision provided by our eyes. However, the majority of digital cameras available on the market capture only two-dimensional projection of a scene. Hence, in a typical image there is a map of pixels, where each pixel represents the intensity of the impinging light. On the other hand, to have a three-dimensional image means to have the same array of pixels, where each pixel represents both intensity and distance information from the camera to specific point in the scene.

There is a great number of possible applications that can benefit from additional source of information provided by a 3D camera. This includes tasks like detection, recognition, surveillance, autonomous navigation, innovative user interface, industrial control and many others. This extra distance information available from a 3D camera improves robustness of object detection and classification with respect to a classical 2D camera approach.

Different range detection techniques are well known and used for a long time and in general, it is a quite broad topic. Figure 2.1 shows a family

tree of main remote distance measuring techniques. There are three main approaches: ultrasonic, microwave and optical [11], [12]. Among optical distance detection techniques there is a division on passive and active. Human vision system belongs to a passive stereoscopy detection class. Range detectors that belong to active class have in their system an active light source, that illuminates a scene. Under the active method there is a further separation on three categories: interferometry, triangulation and Time-of-Flight (TOF). Scanner and scannerless methods are different not only in the illumination unit: the whole system is different. In point scanning systems the sensor is a single detector, while in scannerless system it is an array. Scanning systems need mechanical components, that are not needed

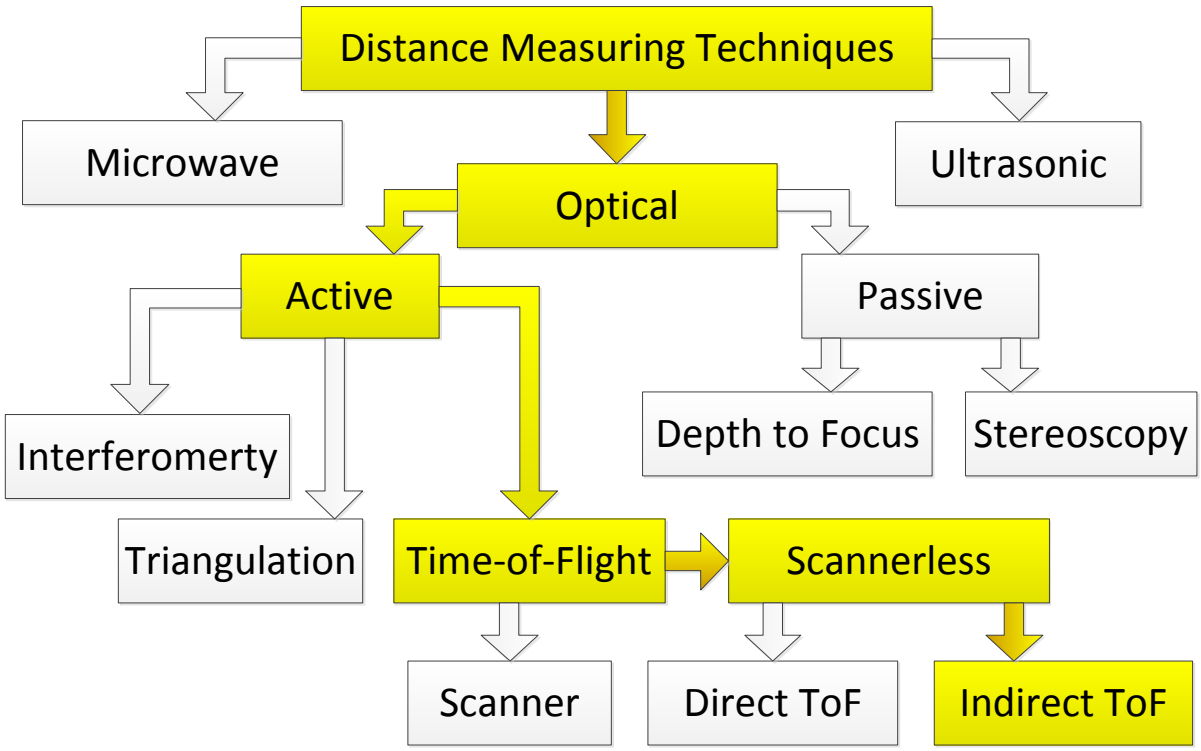

Figure 2.1: Main range detection techniques

in scannerless ones. The work described in this thesis is focused on active Time-of-Flight scannerless category.

2.1 Active distance measurement techniques

The main competitors of a TOF method are active triangulation and interferometry. Here a few examples of triangulation and interferometry implementation will be described. A general overview of TOF methods will be given.

2.1.1 Active triangulation

The basic workflow of an active scanner triangulation method consists of two steps [13]. A laser source, which can be a single point or a laser line, emits light signal onto the scene. The reflection of that signal from the scene falls back onto a detector, which can be a linear array or two-dimensional array. The detector and the laser source are dislocated from each other by a known distance D, called baseline. As the distance from the target to system is changing the back reflected light is focused on a sensor in a different spatial position, as illustrated in Figure 2.2. Using simple trigonometry, the distance Z can be derived as a spot position on the sensor (equation (2.1)).

$$Z = \frac{D \cdot f}{\Delta p + f \cdot tan\alpha} \tag{2.1}$$

There are different implementations of this technique that can cover distance range from a few millimetres to a few kilometres depending on the baseline. In compact devices baseline can be only few centimetres thus the distance range cannot be longer than few metres. The precision of this system is very high and can reach values below 1mm. However,

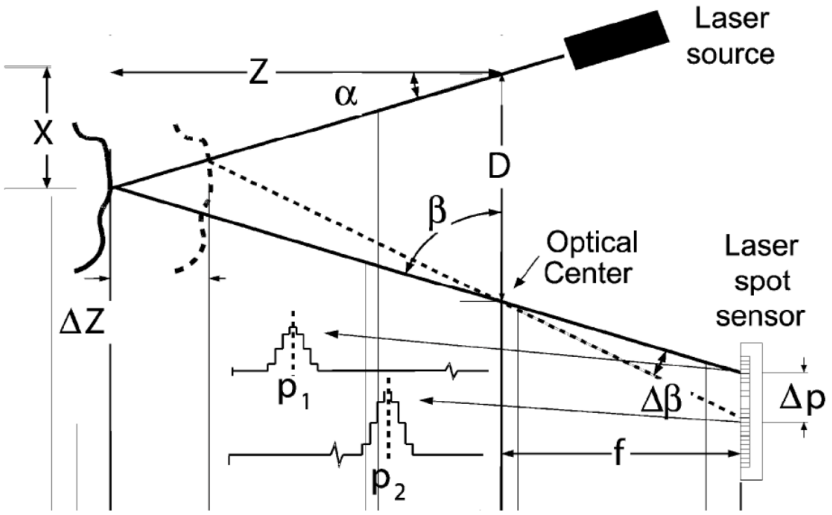

Figure 2.2: Active triangulation distance measurement [14]

this system requires scanning that dramatically increase the cost of this technique implementation.

A recent example of fully custom sensor has been demonstrated by *Mandai et al* [15]. The illumination of a scene is done by a laser blade and the sensor provides a fast estimation of the peak position of the laser-blade by custom designed pixels. This sensor has demonstrated very high precision of less than 1mm at a 40cm distance, as well as very high frame rate in distance measurement.

Another famous example of an active scannerless triangulation technique is a Microsoft Kinect camera, made by PrimeSense company [16]. The basic principle of this system is projection of a grid point pattern on a scene by a laser source. Then the usual image sensor detects the distortion in the projected pattern due to the presence of objects. The estimation of distortion and corresponding depth data is performed by a chip specially designed for this purpose. The distance range of a commercial versions is from 80cm to 3.5m, the distance precision is from a few millimetres to a few centimetres depending on the distance. This camera works at a 3D

frame rate of 15fps. It is important to note that the primary purpose of this camera is user interaction, depth data is only auxiliary information. The main drawback of this system is low distance precision at far distances, due to increasing lateral distances between grid points. There are two more examples of depth cameras produced by PrimeSense company: Carmine 1.08 and Carmine 1.09 [16]. They are different in operating distance ranges and resolution. The first 3D camera is working from 80cm to 3.5m with depth resolution of 1.2cm at 2m. The second camera operates at shorter range from 35cm to 1.4m with depth resolution 0.05cm at 35cm distance and 0.7cm at 1.4m distance. The 3D frame rate of 30fps is the same for both cameras.

2.1.2 Interferometry

Another technique for remote distance detection is the interferometry [17]. The basic structure is based on Michelson Interferometer (Figure 2.3). An interferometer is an optical instrument that splits a laser beam into two parts by a beam splitter. Hence, light travels with two different paths. One part is projected to a mirror and the other illuminates a target of variable distance. Both light beams are reflected back to the beam splitter and projected onto a sensor. When the reflected beams interfere with each other, the region of crossing will exhibit an interference fringe. Moving the reference mirror, the destructive and constructive interferogram is created. By detecting and counting the minimum and maximum transitions in the interference of light wavelength, the distance between the optical system and the target can be measured. This kind of system can achieve extremely high precision, that is defined by wavelength λ, which can be in a nanometre range. However, the range ambiguity of this system also depends on the wavelength, thus it is also very short. Another problem of that system is scanning. In addition, the amount of data generated by this

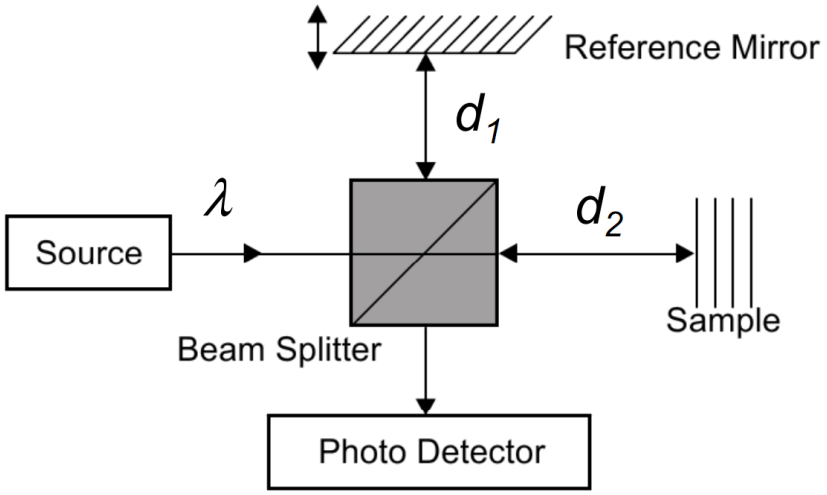

Figure 2.3: Interferometry distance measurement [18]

photodetector and meant for processing is very big [19].

2.1.3 Time-of-Flight

The first Time-of-Flight experiment dates back to 1849 made by Fizeau, who used this technique to measure the speed of light on Earth. The Time-of-Flight technique, as it is evident form the name, measures time t needed for a light beam to fly from a source to a target. This method is based on the knowledge of the speed of light c, which is equal to $3 \cdot 10^8$m/c. The distance D can be derived from the following equation:

$$D = \frac{c \cdot t}{2} \tag{2.2}$$

The division by 2 is needed because, in fact, light travels a round trip from a source to a target and back to a detector, thus $t/2$ is the real time of flight. Figure 2.4 depicts the operation principle of a Time-of-Flight measurement system. Normally, illumination and detection units are made close to each other in order to provide compact setup and exclude shadow effects. Illumination unit can be either a laser source or LEDs.

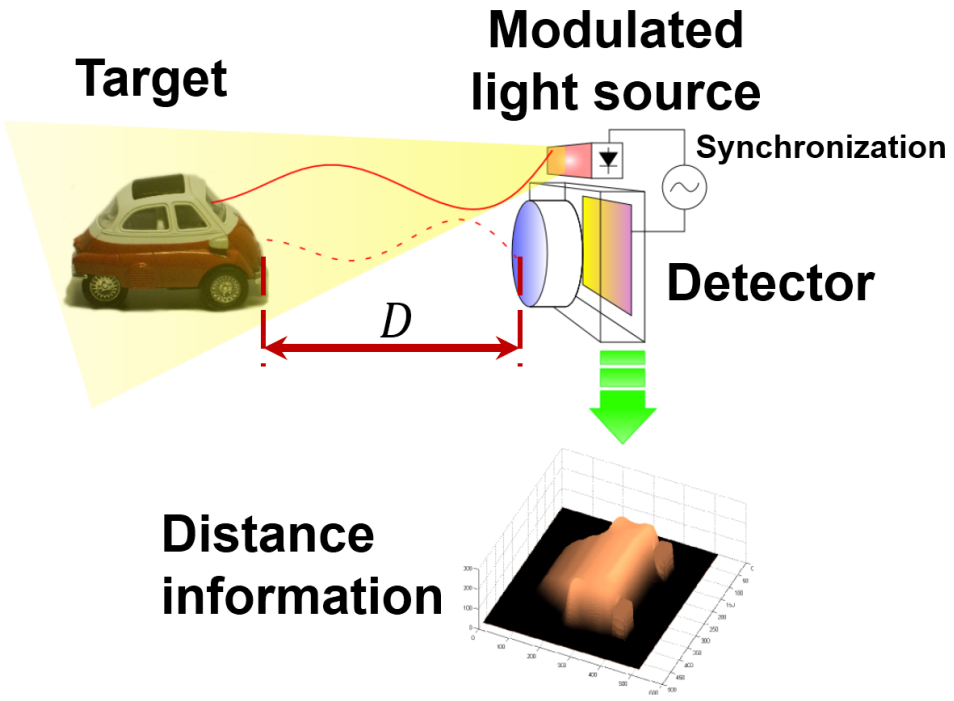

Figure 2.4: TOF principle

The illumination unit sends a light pulse to a target, at the same time the detector clock starts counting time. When a backscattered light from the target reaches the detector, the counting is stopped. Next, the computation of the distance is performed inside or outside detector with the equation (2.2). This setup requires very fast detectors due to high speed of light, for instance to measure 1m distance, the detector capable of measuring 6.7ns time with high accuracy should be employed.

One of the devices that can handle high speed photodetection is a Single Photon Avalanche Diode (SPAD) [20]. The advantage of this device is in its high sensitivity due to intrinsic amplification of charge inside the device. More details on it will be given in Chapter 3. For now this device can simply be represented as a digital switch sensitive to light. Since the progress on device side has entered standard CMOS technology increasing research efforts on a 3D cameras based on SPADs have been observed [21], [22],

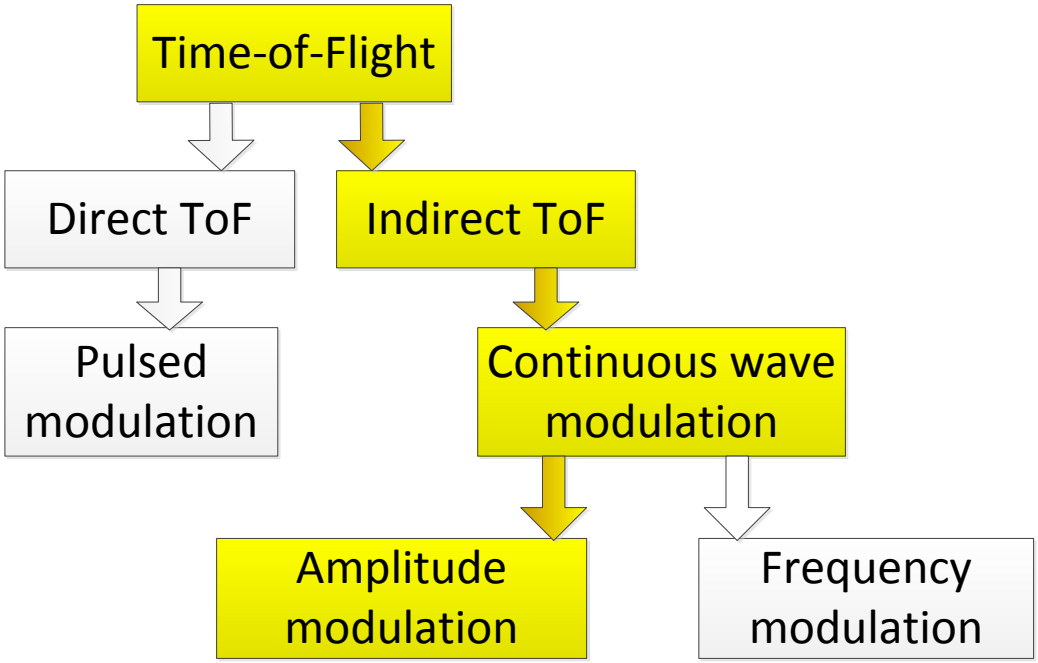

Figure 2.5: Main Time-of-Flight techniques

[23], [24], [25]. A recently presented camera system demonstrated distance range up to 100m, with precision 14.2cm at the maximum distance and 3D frame rate of 10fps. This 3D sensor consist of 202 $\times$ 96 pixels made in 0.18μm HV CMOS technology [25].

Figure 2.5 illustrates the family tree of TOF distance measurement method. The TOF sensor described above belongs to Direct TOF (D-TOF) category. Indirect TOF (I-TOF) is an alternative method that can be more easily implemented in scannerless systems. Instead of pulsed light modulation the system utilizes continuous light modulated. As a result, time of flight is expressed by the phase difference between emitted and received light signals, after the reflection from a target object being measured

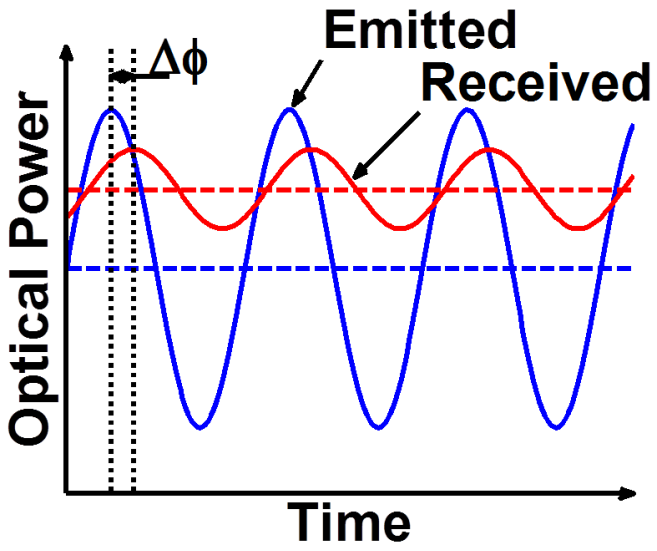

Figure 2.6: Phase-shift illustration

(Figure 2.6).

$$t = \frac{\Delta\varphi}{2\pi f_m} \tag{2.3}$$

This difference is sensed by a detector and after that processed to derive distance information.

$$D = c \cdot \frac{\Delta\varphi}{4\pi f_m} \tag{2.4}$$

In the equation (2.4) f_m is a modulation frequency of a light source, $\Delta\varphi$ is a phase difference and c is the speed of light. Continuous wave (CW) modulation I-TOF method can be implemented using various modulation, demodulation and detection alternatives. Modulation can be square, sine-wave or any other shape, different types are utilized in 3D cameras [26], [27]. However, since the continuous modulation is a periodic process, only a limited distance range can be measured unambiguously. Non-ambiguity range is determined by the equation (2.5).

$$D_{max} = \frac{c}{2 \cdot f_m} \tag{2.5}$$

For instance, at 50MHz modulation frequency unambiguous distance range

is 3m. Maximum unambiguous range can be increased by reducing modulation frequency, however, this will result in lowering distance precision σ_D, since it depends on the modulation frequency as well:

$$\sigma_D = c \cdot \frac{\sigma_{\Delta\varphi}}{4\pi f_m} \tag{2.6}$$

Here, $\sigma_{\Delta\varphi}$ is a precision in phase measurement. One of possible solutions for non-ambiguity range expansion is to employ several modulation frequencies for different ranges.

The technique described above, which exploits single modulation frequency to perform distance measurement is called homodyne or phase-shift technique. Frequency modulation technique, called heterodyne or frequency-shift, is also utilized for distance estimation. This technique is widely used in laser range finders for different applications [28], [29], [30]. This method is known for large dynamic range and high resolution at short distances. The schematic setup for this type of distance measurement is illustrated in Figure 2.7. The distance can be calculated with the following equation:

$$D = \frac{c \cdot f_{if} \cdot t_m}{2 \cdot \Delta f} \tag{2.7}$$

where f_{if} is the intermediate frequency difference between reference signal and object signal, t_m is a ramp period and Δf is a periodic frequency shift. The drawback of this technique is in wide bandwidth and high linearity requirement for illumination source and detection unit [31].

Several research works have demonstrated employment of commercially available avalanche photodiodes as a good electro-optical mixers for intermediate frequency detection, applied to frequency-shift distance measurement [29], [32]. The first work [29] has demonstrated 5cm resolution on a range from 5m to 40m. The second work has not presented the distance measurement, however this idea was adopted for APD implementation in CMOS technology [33]. Unfortunately, there is still no demonstration of

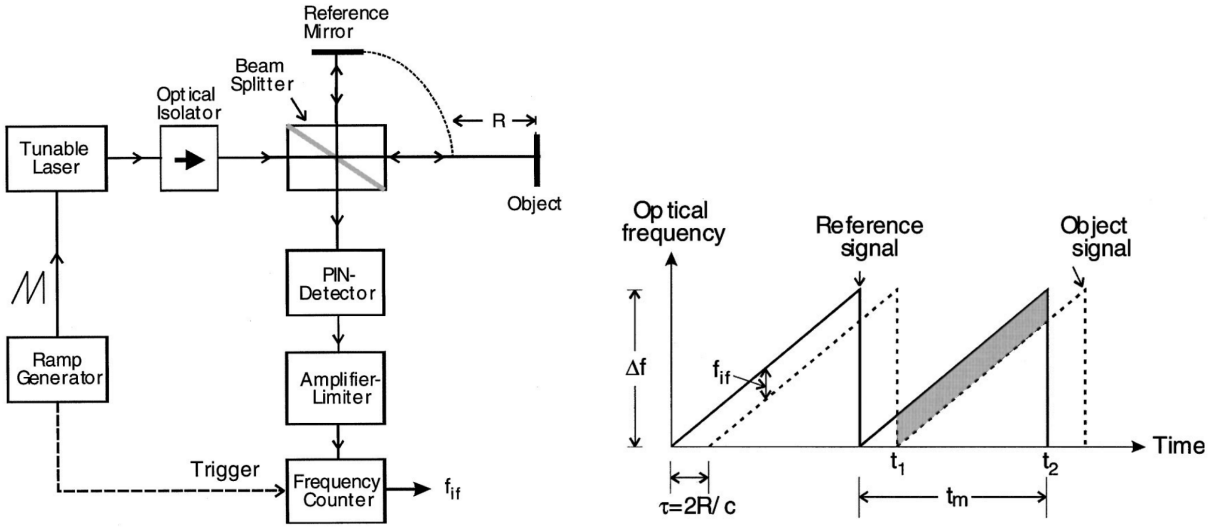

Figure 2.7: Frequency Modulated Continuous Wave distance detection principle [31]: a - FMCW setup for distance measurement, b - optical frequency dependence on time

distance measurement by this technique. The reason behind this can be in the incorrect design of CMOS avalanche photodiode. According to figures of pixel layout provided in the paper [33] the avalanche photodiode structure has sharp corners where breakdown occurs first due to high electric field concentration.

In this thesis work, our test pixel and sensor are investigated in a single frequency phase-shift TOF technique, even though potentially they can operate also in frequency-shift technique. In the next section several examples of state-of-the-art demodulation sensors working at a single modulation frequency will be presented.

2.2 Demodulating image sensors for Indirect Time-of-Flight measurement

In this section the state of the art of TOF image sensors based on I-TOF technique will be described. The basic building block of such sensors is

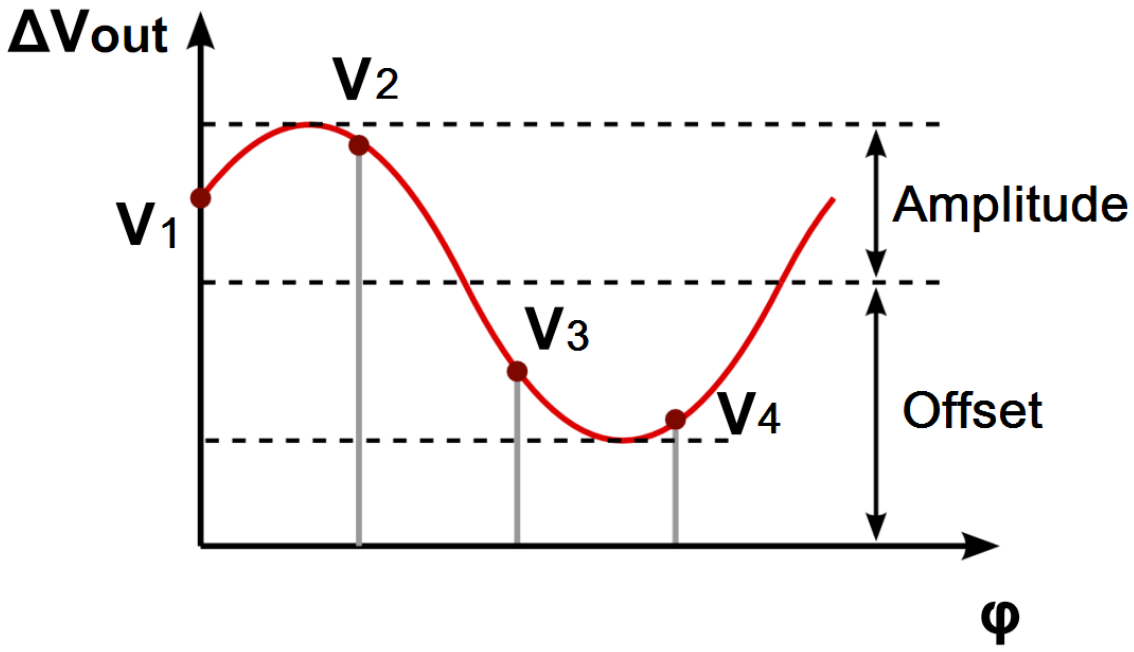

Figure 2.8: Voltage dependence on the phase difference between light signal and demodulation signal

a pixel, that performs synchronous detection of modulated light and its demodulation. The output of a demodulation pixel has a sine-wave dependence on the phase difference between electrical demodulating signal and receiving optical signal. Figure 2.8 illustrates the output voltage dependence on the phase difference φ. In order to extract phase information four measurements with $\pi/2$ relative phase shift are needed. Hence, the frame rate for 3D image reconstruction is four times slower than for 2D image acquisition. After acquisition of four voltages the phase value can be computed by following equation:

$$\varphi = tan^{-1}\frac{V_4 - V_2}{V_3 - V_1} \tag{2.8}$$

Thus the distance can be expressed as:

$$D = \frac{c}{4\pi \cdot f_m} \cdot tan^{-1}\frac{V_4 - V_2}{V_3 - V_1} \tag{2.9}$$

Other two important parameters that characterize the output signal of a pixel and can be derived from four acquisitions are amplitude and offset. The useful information is contained in the amplitude value, while the offset is there due to ambient light presence or demodulation inefficiency of a pixel or some other reasons like pixel dark current. The offset reduces the dynamic range of a pixel. Amplitude and offset can be calculated from following equations:

$$Amplitude = \frac{\sqrt{(V_4 - V_2)^2 + (V_3 - V_1)^2}}{2} \tag{2.10}$$

$$Offset = \frac{V_1 + V_2 + V_3 + V_4}{4} \tag{2.11}$$

The most important figure of merit for demodulating pixels is demodulation contrast. The quality of a demodulation device can be represented by demodulation contrast C_D as a ratio between demodulated amplitude and offset.

$$C_D = \frac{Amplitude}{Offset} \tag{2.12}$$

Other figures of merit for 3D TOF image sensors are distance resolution σ_D that is a function of phase measurement noise, distance range that in the case of demodulating pixels maximum range is limited by distance ambiguity, and lateral resolution, which depends on the number of pixels in a sensor. In addition, there is Fixed Pattern Noise that is a pixel to pixel voltage variation under the same illumination condition and 3D frame rate.

Part of the requirements for 3D TOF sensors are common to usual image sensors, that are high sensitivity, low noise, high dynamic range and high fill factor. Other requirements are more specific for TOF sensors, that are high demodulation contrast, high modulation frequency, which increases the distance precision, high quantum efficiency in Infra-Red spectrum, while ordinary image sensors are tailored to visible light spectrum region, and

low power consumption, which is also important when targeting battery operation or large number of pixels in a sensor.

Several different types of demodulating detectors have been presented in the literature. They can be roughly divided into four groups, namely photogate-based sensors, Current Assisted Photonic Demodulators, pinned photodiode sensors and static drift field devices.

2.2.1 Photogate-based demodulator

Research in the field of photo-demodulating devices started in 90s [34]. The first published work has demonstrated photogate-based demodulating sensor fabricated in $2\mu m$ CMOS/CCD process. Two research groups from USA and Germany were working on the same topic at the same time [35], [36]. Both groups came up with similar sensors and comparable performance. *Miyagawa et al.* [35] has demonstrated single line of 32 pixel sensor measuring distance with 15cm precision at 15m range. Charge domain signal processing was used to perform demodulation in those works.

The first 3D TOF camera based on CCD/CMOS photogate pixels was demonstrated by *Lange et al.* in 2001 [27]. Figure 2.9 shows a cross section of a CCD part of demodulation pixel implemented in 64×25 sensor used in the camera. Different gate voltages result in the change in potential gradient under the gates. By synchronous modulation of gate voltages and impinging light, the generated charge carriers move to one of two sides, either under integration gate or dump diffusion. Pixel size is $21 \times 65\mu m^2$ with a fill factor of 22%. The 3D camera has demonstrated 5cm resolution over a full distance range of 7.5m at 20MHz modulation frequency. Demodulation contrast shown by this camera was less than 64%.

The advantage of this solution is in simplicity of in-pixel readout electronics, that can consist only of three transistors, thus the pixel can be very compact. The drawbacks of these devices are high cost of modified

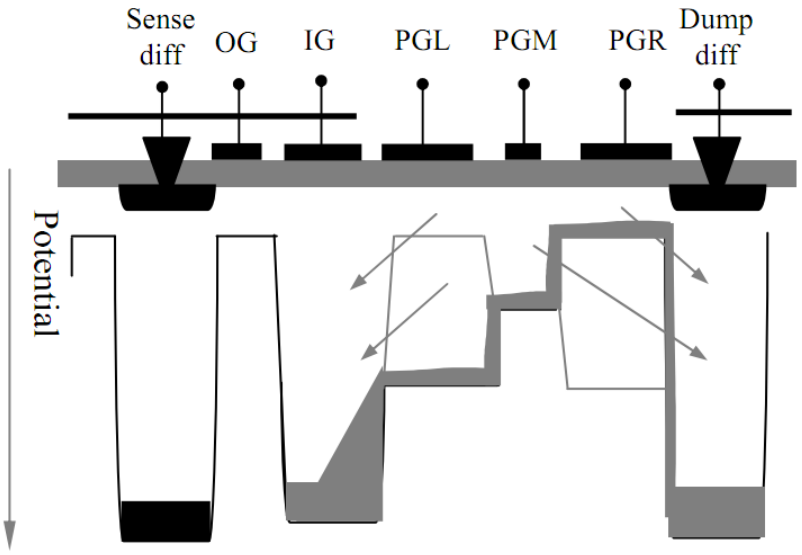

Figure 2.9: Cross sectional view of the CCD part of a pixel (IG - integration gate, PGL/PGM/PGR - left/middle/right photogates)[27]

process, absence of ambient light suppression mechanism and reduced sensitivity because of the photogate layer.

The evolution of the photogate device described above was presented by *Oggier et al.* [37]. The dump diffusion of the previous pixel was replaced with an integration gate. The readout now was possible from both sides, thus introducing differential readout scheme with the advantage of noise reduction. Pixel size is $39 \times 55\mu m^2$ with a fill factor of 17%. The sensor had 160×124 pixels. The modulation frequency and distance range was 20MHz and 7.5m, the same demonstrated by *Lange et al.* 3D camera. Demodulation contrast achieved by this camera was 40%. This camera was the first in a series of commercialized products $SwissRanger^{TM}$ produced by Mesa Imaging company [38]. This company is still present in the market and their last camera $SwissRange^{TM}$ SR4000 has 176×144 pixels with $40\mu m$ pixel pitch (Figure 2.10). The camera is dedicated for indoor use only and has 5m and 10m switchable range with maximum 3D frame rate

Figure 2.10: Example of 3D camera produced by Mesa Imaging company

of 50fps. Distance resolution is 2cm for 5m range and 3cm for 10m range [39], [40].

Photonic Mixing Device

A similar device, which belongs to the photogate-based detectors, introduced by another research group from the University of Siegen, Germany, in 1997 [36] turned out into a 3D camera product [41] produced by PMDtechnology company [42]. The demodulating pixel has two photogates instead of three as in the works described above. Though, the working principle is similar, part of photogenerated carriers are driven towards one of floating diffusions and another part to another floating diffusion. Figure 2.11 illustrates simplified device structure and operation principle. When incoming light is constant and gate modulation is rectangular with 50% duty cycle, the output signals at two readout nodes are equal (Figure 2.11b). In other case, when incoming light is modulated with rectangular signal and there is no phase difference between light and gates' modulation, most of the charge carriers are collected by only one readout node (Figure 2.11c). Any other phase difference between optical and electrical modulation will result in different ratios between two output nodes.

PMDtechnologies company launched series of integrated image sensors PhotonicICs® fabricated in CCD/CMOS technology for 3D imaging ap-

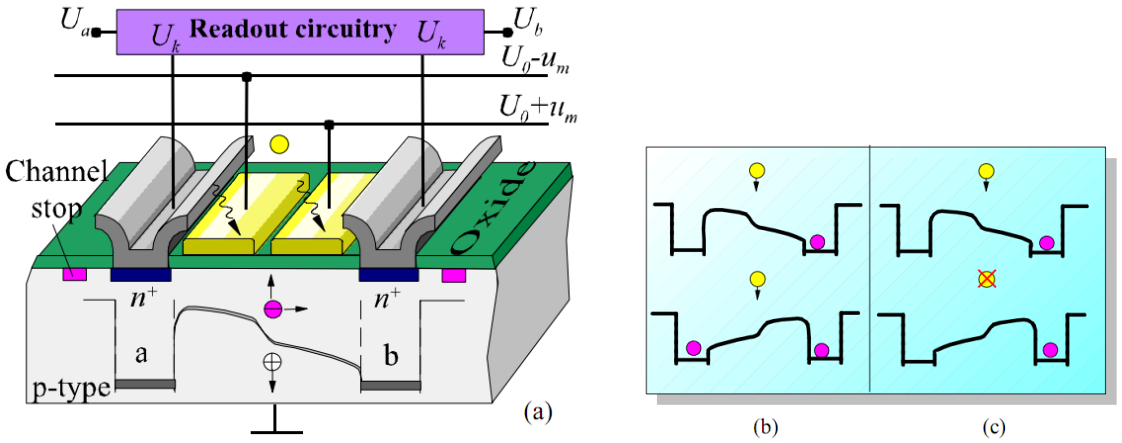

Figure 2.11: Simplified PMD structure and modulation principle of the device [42]

plication in 2005. The maximum demodulation contrast of their sensors is 50% with the bandwidth of 100MHz. Currently available PhotonicICs®19k - S3 sensor has 160 × 120 array size with background illumination suppression. The commercially available 3D camera CamCube3.0 has 200 × 200 pixel array, 7.5m maximum distance with centimetric resolution and 15fps 3D frame rate [40]. Furthermore, this company offers very compact 3D camera systems called CamBoard nano, based on PhotonicICs®19k-S3 chip, and CamBoard pico, which is a reference design not freely available, thus there is no information about its performance. Two examples of 3D camera systems are presented in Figure 2.12. The offered camera systems can be used in outdoor environment with direct sunlight. This company is one of the leading in 3D TOF camera industry.

Another study on the photogate devices was done by researchers at Shizouka University, Japan they implemented a demodulating pixel in a standard 0.35μm CMOS process with one additional implant, consisting of an n-buried layer below a field oxide [43]. The sensor array is 336 × 252 pixels with 15μm pixel pitch. The measured distance range is from 1.6 to 12.3m and the best range resolution of 2.35cm was achieved at 30 3Dfps and 1MHz modulation frequency with 10% duty cycle.

a b

Figure 2.12: Examples of 3D camera system provided by PMDtechnologies company: a - CamCube3.0, b - Camboard nano (dimensions:37×30×25)

More recent example of photogate-based demodulating sensor was demonstrated by *Stoppa et al.* [44] in 2010. A photo-demodulator has a modified pinned structure that helps to reduce transfer time required for photogenerated charge carriers to reach collection electrodes. Measured demodulation contrast is 29.5% up to 50MHz modulation frequency. This sensor was fabricated in a standard $0.18\mu m$ CMOS Image Sensor technology with 80 × 60 pixel array, pixel pitch of 10 μm and 24% fill factor. The distance range achieved by a 3D camera system working at 20MHz modulation frequency was from 20cm to 6m with the best precision of 4cm at 2.5m distance.

The evolution of this pixel was presented by *Lee et al.* [45] in 2011. The sensor, fabricated in a standard $0.13\mu m$ CMOS Image Sensor technology, has demonstrated 53% demodulation contrast at 20MHz modulation frequency. The array size is 192 × 108 pixels with 28 μm pixel pitch. Gain in device performance was achieved through doping optimization of n- and p-layers, which is possible through the control over a technological process.

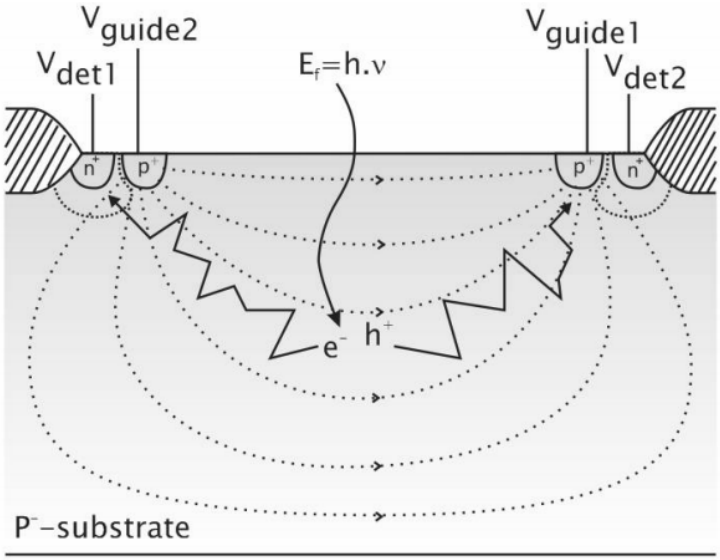

Figure 2.13: Schematic cross section of Current Assistent Photonic Demodulator [46]

2.2.2 Current Assisted Photonic Demodulator

One more interesting concept of photo-demodulating device was introduced by *Van Nieuwenhove el al.* in 2005. The author proposed Current Assisted Photonic Demodulator (CAPD). The device cross section is given in Figure 2.13. Two p+ contacts and two floating diffusions are made in a lightly doped p-substrate. When two p+ contacts are biased at different voltages a static current and corresponding electric field appears in the substrate between two contacts. This electric field forces charge curries, generated at the central part of the device, to move towards one or another floating diffusions. With this mechanism a similar effect is achieved as with photogates. The advantage of this structure with respect to photogate implementation is that electric field goes deeper in the device substrate increasing quantum efficiency and maintaining a high modulation frequency. The major disadvantage of this structure is high power consumption due to static hole current.

The first sensor based on CAPD structure was presented by *Van Der*

a b

Figure 2.14: Examples of 3D camera system produced by SoftKinetic company: a - DS311, b - DS325

Tempel et al. [47] in 2008. The sensor, fabricated in a $0.35\mu m$ standard CMOS technology, has 32×32 pixel array with $30\mu m$ pixel pitch and fill factor as high as 66%. The demodulation contrast demonstrated by the sensor was 51% at 20MHz modulation frequency. However, the power consumption was 1.4mW per pixel due to modulation. The solution was found in the increase of substrate resistivity. 3D cameras based on CAPD sensors are now available in consumer market. SoftKinetic company produces two models of 3D cameras DepthSense DS325 and DS311 [48] (Figure 2.14). DepthSense DS325 camera has QVGA depth sensor resolution, distance range from 15cm to 1m, depth precision less than 1.4cm at 1m, and maximum 3D frame rate of 60fps. DepthSense DS311 camera has 160×120 pixel depth sensor, distance range from 1.5m to 4.5m, depth precision less than 3cm at 3m distance, and maximum 3D frame rate of 60fps. Both cameras are meant for indoor operation only.

The implementation of CAPD device in a more advanced $0.18\mu m$ CMOS technology was proposed by *Pancheri et al.* [49] in 2010. The modulation contacts are p-wells and there is an external p-well that is connected to ground, in which pixel electronics is integrated. The array of 120×160 pixels was demonstrated with a pixel pitch of $10\mu m$ and 24% fill factor.

Without any process modification the power consumption of $10\mu W$ per pixels was achieved. Demodulation contrast higher than 40% was measured up to 30MHz modulation frequency with 1.6V modulation amplitude and higher than 35% up to 45MHz for 1.2V modulation amplitude [50]. A 3D system based on this sensor is capable of acquiring a stream of 7 3Dfps, has the range from 1.2 to 3.7m and a precision better than 10cm at 2m.

2.2.3 Pinned photodiode demodulator

Next type of photo-demodulating structure is a pinned photodiode, which was proposed as TOF sensor and patented in 2003[1]. However, no implementation of this sensor has been demonstrated until 2010. In the last two years this type of photo-demodulator has been intensively investigated, since pinned photodiode structures are now available as standard cells in a CMOS Image Sensor process.

The first demonstration of a pinned photodiode as a photo-demodulator, fabricated in a $0.18\mu m$ imaging CMOS technology, was presented by *Stoppa et al.* [44] in 2010. Figure 2.15 demonstrates cross-section of a photo-demodulator based on a standard pinned photodiode and modified pinned photodiode, proposed by the authors, with corresponding energy band diagrams. The second photo-demodulator has a modified pinned structure that helps to reduce transfer time required for photogenerated charge carriers to reach collection electrodes. Measured demodulation contrast is 29.5% up to 50MHz modulation frequency. This sensor has 80×60 pixel array, $10\mu m$ pixel pitch and 24% fill factor. The distance range achieved by a 3D camera system working at 20MHz modulation frequency was from 20cm to 6m with the best precision of 4cm at 2.5m distance. The progress on this side was demonstrated with QVGA resolution TOF sensor in 2012 [9]. The sensor, fabricated in the same technology, has $14\mu m$ pixel pitch

[1] V. Berezin, et al., US Patent 2003/0213984A1, 2003

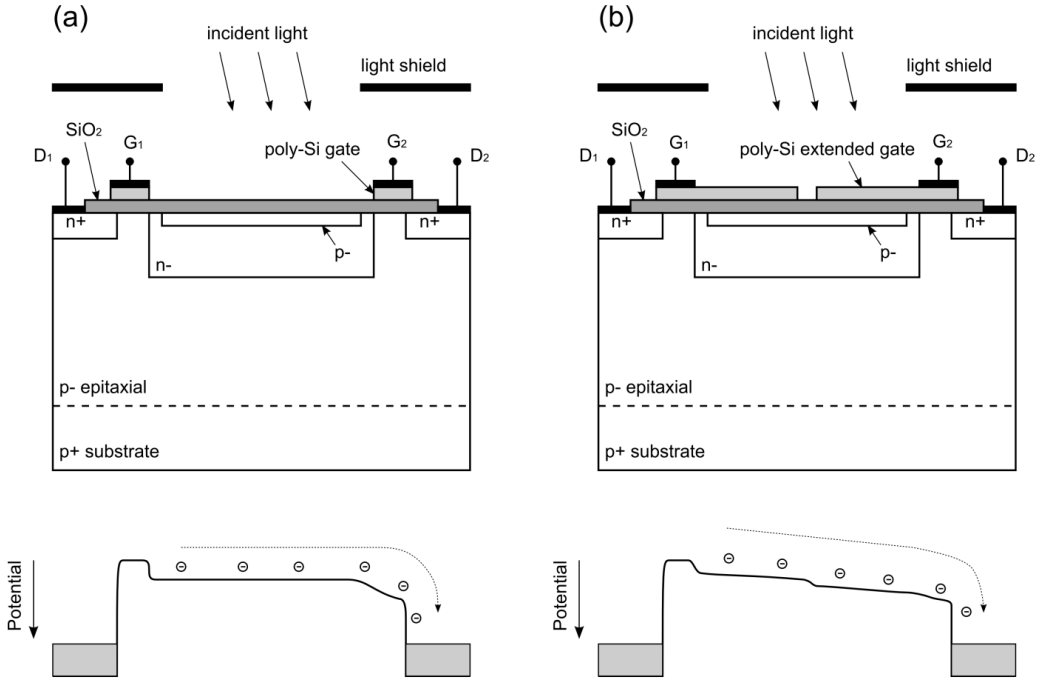

Figure 2.15: Cross-section of two photo-demodulators: a - based on a standard pinned photodiode, b - based on modified pinned photodiode; with corresponding energy band diagrams [44]

with 48% fill factor and maximum 3D frame rate of 70fps. The camera system based on this sensor showed high dynamic range capability by combining 3D images made at different integration time. The modulation frequency was 16.7MHz, combined distance range was from 80cm to 7.5m with the best precision of 2.6cm at 3m distance.

In parallel, another research group from Samsung Advanced Institute of Technology started investigation on pinned photodiode application for depth detection in 2010 [51]. This research group is working not just on a 3D image sensor, but they try to combine 2D and 3D image sensors in a single chip. Hence, the structure of pinned photodiode is kept unmodified, in order to be suitable also for 2D imaging (Figure 2.15a). The group effort resulted in a fabrication of the first sensor with a 64 $\times$ 64 pixel array in 0.18μm imaging CMOS technology. The pixel pitch was 12μm with fill

factor of 62%. The modulation frequency used for the measurement was 5MHz, and demodulation contrast achieved 35%. The measured distance range was from 1m to 4m and the best precision was 2cm at 1m distance.

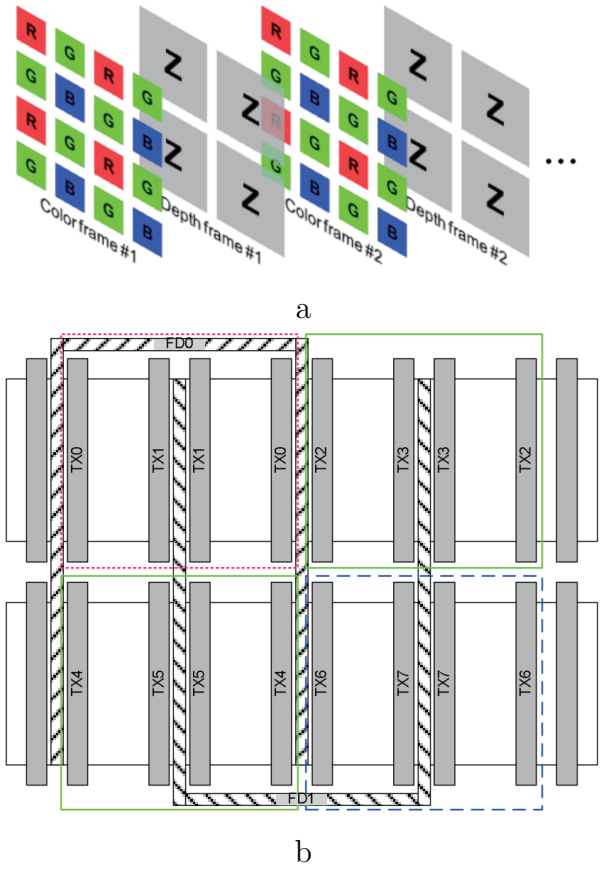

Figure 2.16: Conceptual diagram of 2D and 3D frames acquisition and a simplified layout of photodiodes and transfer gates in 2 × 2 pixels [52]

The evolution of this work turned out into next sensor consisting of 640 × 480 pixels fabricated in 0.11μm CMOS IS technology [52]. This image sensor does not contain any dedicated pixels for depth measurement. Both 2D and 3D images can be captured by switching operation modes. Each four colour pixels contain single pixel used for 3D image reconstruction, thus the resolution of 3D image is reduced with respect to standard colour image. Conceptual diagram of 2D and 3D frames acquisition and a simplified layout of photodiodes and transfer gates in 2 × 2 pixels is illustrated

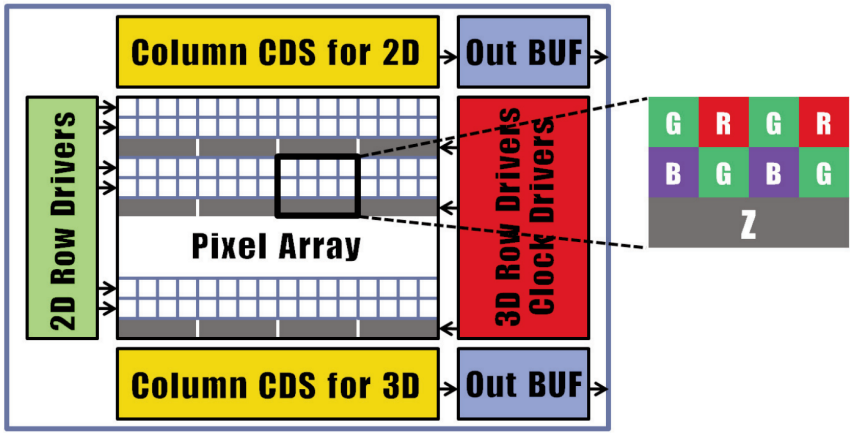

Figure 2.17: Sensor architecture with pixels arrangement [54]

in Figure 2.16. Pixel pitch is $6\mu m$ for colour image and $12\mu m$ for depth image. The measured distance range is from 1m to 3m with 1cm and 6cm depth accuracy for 1m and 3m, respectively. The modulation frequency of 10MHz was used for depth measurement.

Next generation of the sensor based on the same concept with full-HD resolution for 2D image and 480× 270 effective resolution for depth image was presented in 2012 [53]. Pixel size is $3.65\mu m$ for colour image and $14.6\mu m$ (4×4 binning) for depth image. The measured distance range is from 0.75m to 4.5m. Depth error is from 1cm to 3.8cm for different integration time. Now the modulation frequency of 20MHz was used for depth measurement with 11 3D frames/s acquisition and demodulation contrast reached 52.8%.

Another example of 2D and 3D image sensor combination was presented in 2012 [54]. Here a standard 2D image sensor was modified in order to accommodate depth sensor inside. The sensor has 1920×1080 pixel array where every third row is replaced by depth pixels with 2.25×9 μm^2 size. Thus, the size of depth imager is 480×360 pixels. The architecture of the sensor with arrangement of pixels is given in Figure 2.17. The employed technology node was 0.13 μm CMOS Image Sensor and the depth pixel

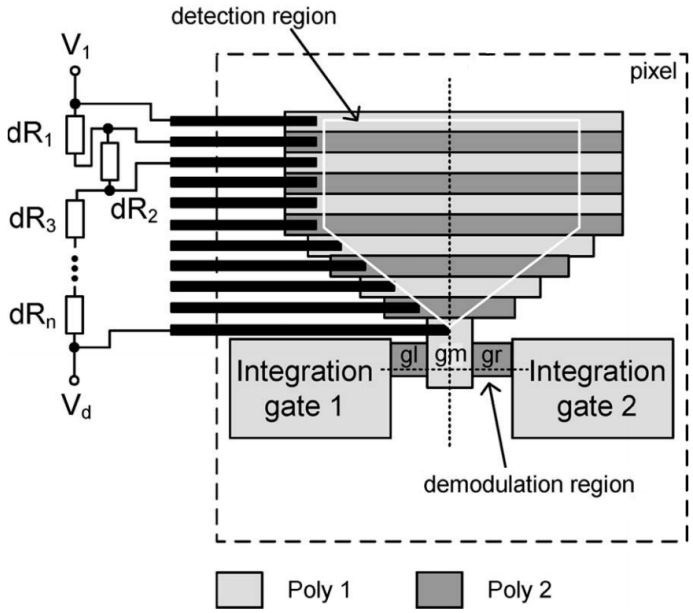

Figure 2.18: Static drift field pixel [55]

fill factor reached 48%. The demonstrated distance range was from 1m to 7m with 0.5cm range accuracy at 1m distance at 20MHz modulation frequency.

2.2.4 Static drift field device

The last group of 3D demodulating sensors that will be discussed in the thesis is based on static drift field devices. The concept of this device was first presented by *Buttgen et al.* [55] in 2006. The authors proposed to separate photo-detection and demodulation regions. This solution allows for a pixel to achieve high bandwidth, high fill factor and low power consumption. Figure 2.18 shows the static drift field pixel. The detection region is made of two photo-transparent poly gates, all gates are set to constant voltages linearly increasing from 0 to Vd. Due to minimum width of poly gates the built lateral electrical drift field is almost constant driving the electrons generated in detection region toward a small central gate (gm).

The modulation of two gates (gl,gr) in the demodulation region allows the device to acquire two samples of the signal. The cutoff frequency of such device can exceed 100MHz. The proof of concept was performed on a 176 $\times$ 144 pixel array fabricated in 0.6μm CMOS/CCD technology. The size of the pixel was 40 $\times$ 40 μm^2 with 25% fill factor. The measured distance range was from 50cm to 3.5m with the distance precision of 2.5cm at 1m, and 20MHz modulation frequency.

2.3 Summary

Table 2.1 reports the performance summary of described above sensors. Photogate-based sensors offer simplicity in the readout circuit and compact pixel size, however, the utilization of photogate layers reduces detector's sensitivity. In addition, sensors that are fabricated in modified technological process have higher cost with respect to sensors fabricated in a standard process. That is relevant for all types of demodulating sensors. PMD-based sensors suffer from low frame rate, even though they have good distance range and precision. Sensors based on CAPD devices have limited distance range and modified technological process. Two perspective implementations based on standard pinned photodiodes have also disadvantages. The first sensor has low frame rate due to sequential operation of 2D image and 3D image modes. The second one has modified 2D image array, thus the resolution of both images are reduced. Unfortunately, there is no information about frame rate, but in general sensor demonstrates very good range and high distance precision at close distances. Regarding static drift field devices quite complex layout is the main drawback.

As a conclusion, there is still a demand in depth sensors improvement. In particular, higher demodulation contrast is required, better distance precision at longer ranges, which in case of demodulation pixels means

higher modulation frequency, higher lateral resolution, higher 3D frame rate, low system power consumption and device cost.

Table 2.1: Performance Comparison of Different Types of Demodulating Sensors

Ref./ Detector type	Technology	Sensor resolution	Pixel pitch/ Fill factor	Modulation frequency	Demodulation contrast	Distance range	Distance precision	3D frame rate
[39]/ photogate-based	n.a.	176×144	40μm/ n.a.	30MHz/ 15MHz	40%	max 5m/ 10m	2cm/ 3cm	50fps
[42]/ PMD	CCD/ CMOS	200×200	28μm/ n.a.	20MHz	50%	max 7.5m	few cm	15fps
[44]/ PMD	0.18μm CIS	80×60	10μm/ 24%	20MHz	30% @50MHz	20cm-6m	4cm @ 2.5m	n.a.
[45]/ PMD	0.13μm CIS	192×108	n.a.	20MHz	50%	1m-7m	1cm-6cm	n.a.
[48]/ CAPD	n.a.	320×240	n.a.	n.a.	n.a.	15cm-1m	1.4cm @ 1m	60fps
[48]/ CAPD	n.a.	160×120	n.a.	n.a.	n.a.	1.5m-4.5m	3cm @ 3m	60fps
[49]/ CAPD	0.18μm CMOS	120×160	10μm/ 24%	n.a.	>40% @30MHz	1.2m-3.7m	10cm @ 2m	7fps
[9]/ pinned	0.18μm CIS	320×240	14μm/ 48%	17MHz	n.a.	0.8m-7.5m	2.6cm @ 3m	70fps
[53]/ pinned	0.11μm CIS	480×270	14.6μm/ n.a.	20MHz	53%	0.75m-4.5m	1cm-3.8cm	11fps
[54]/ pinned	0.13μm CIS	480×360	9μm/ 48%	20MHz	n.a.	1m-7m	0.5cm @1m; 16cm @7m	n.a.
[55]/ static drift field device	0.6μm CMOS/ CCD	176×144	14μm/ 25%	20MHz	n.a.	0.5m-3.5m	2.5cm @ 1m	n.a.

Chapter 3

The Proposed Approach: Avalanche Photodiode

This chapter is devoted to a general description of avalanche photodiodes and their implementation in a standard CMOS process. The existing works on CMOS avalanche photodiodes are also reviewed in the following paragraphs. In addition, the operation principle of avalanche photodiode application for Time-of-Flight distance detection is described.

3.1 Avalanche Photodiode Introduction

In the last four decades, the progressive development in solid-state multiplication based photodetectors has been observed. In this section the description of avalanche photodiode types and their operation principle is presented.

3.1.1 Avalanche photodiode

Current research in the area of avalanche photodiodes is proceeding in two directions. The first one exploits dedicated technological processes to realize APDs with state-of-the-art performance [56]. The second way proposes

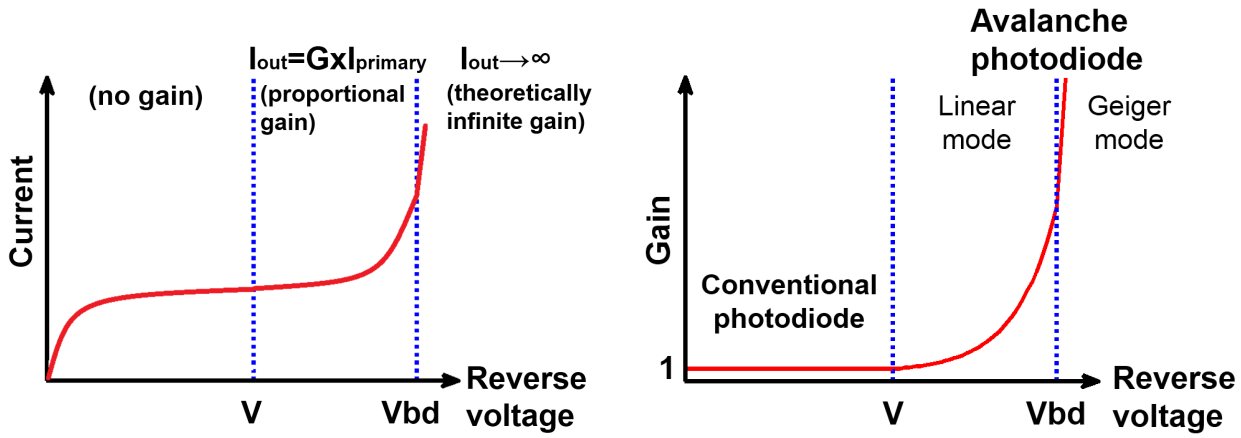

Figure 3.1: Current-voltage and gain-voltage characteristic of a photodiode: a - schematic I-V curve of a photodiode, showing linear and Geiger operation modes, b - schematic gain-voltage characteristic

to fit an APD design to standard CMOS processes in order to reduce cost and enable their monolithic integration with readout electronics.

The suggestion to create a photodetector based on solid-state APDs in order to reach high sensitivity and dynamic range was made decades ago [57]. However, the first implementation of an APD pixel array in a standard CMOS technology was demonstrated only lately [58].

An APD is a photodiode reverse biased near or above its breakdown voltage, where its optical gain is greater than one (Figure 3.1). When an APD is biased below the breakdown voltage it is known as a *proportional* or *linear* mode APD. When an APD is biased above the breakdown voltage, the optical gain becomes theoretically infinite and with the help of readout electronics such APD is able to detect a single photon. The APD working in this regime, which is also known as Geiger-mode, is called Single Photon Avalanche Diode (SPAD). Although the invention of SPADs was made long ago [59], [60] the first pixel arrays based on SPADs in CMOS technology have been made only ten years ago [61]. Since that time an increasing progress in this area has been observed [23], [62], [63].

The level of the development of linear-mode CMOS APDs drops behind to that of CMOS SPADs, which have already been used as a part of CMOS image sensors. Currently only few implementations of linear-mode APDs are known and no attempts yet devoted to the development of large arrays based on APDs operating in linear mode. However, the application field for such devices is potentially wide especially where high sensitivity and fast response are required.

3.1.2 Operation principle of linear-mode APD

Avalanche photodiodes are p-n junction photodiodes that operate at high electric fields in order to achieve avalanche multiplication. In reverse biased photodiodes, the electric field increases in response to the applied voltage, causing the increase in the drift velocity and kinetic energy of charge carriers, injected in the depletion region. This results in carriers energies high enough to break a bond in case of interaction with lattice atoms. This process, called impact ionization, leads to the generation of a new electron-hole pair [64]. The original carrier together with the secondary one will be accelerated by the electric field and contribute to the generation of more and more electron-hole pairs, thus resulting in avalanche multiplication of the number of carriers and the internal current.

Two main factors control the avalanche effect. The first is the carrier ionization rates, which are defined as the number of pairs created by a carrier per unit distance passed, and the second one is the speed at which electrons and holes exit the high-field region and are collected by the electrodes. Ionization rates strongly depend on the electric field, ionization rates increase with electric field growing. For bias voltages below the breakdown, ionization rates are compensated by the extraction rate, so that carrier concentration and output current are increased by a finite multiplication factor M. Typically the gain has values from a few tens to

a few hundreds and can be expressed by the equation (3.1).

$$M_{ph} = \frac{I - I_{MD}}{I_P - I_D} = \frac{1}{1 - (\frac{V_R - IR_s}{V_B})^n} \tag{3.1}$$

Where I is the total multiplied current, I_{MD} is the multiplied dark current, I_P is the primary (unmultiplied) photocurrent and I_D is unmultiplied dark current. V_R is the reverse bias voltage, V_B is the breakdown voltage, R_s is the series resistance and n is a constant that depends on the semiconductor material, doping profile and radiation wavelength [64]. The output current I_{ph} of an APD operating in a linear-mode is proportional to the impinging light intensity P_{opt}, responsivity R and multiplication factor or avalanche gain M [65].

$$I_{ph} = R \cdot Popt \cdot M \tag{3.2}$$

Another important parameter is the excess noise factor F. It indicates the increase in shot noise due to the variations in the APD gain factor M [66]. Noise factor F strongly depends on the ionization ratio k, which is a ratio between hole and electron ionization rates, and multiplication factor M.

$$F = M \cdot k + (2 - \frac{1}{M}) \cdot (1 - k) \tag{3.3}$$

3.2 Related work on linear-mode APDs

Currently, commercial linear-mode silicon APDs are fabricated in tailored technologies, with outstanding performances in terms of Quantum Efficiency (QE), Noise Factor (F) and Bandwidth. Such companies as Hamamatsu Photonics, Advanced Photonix, Perkin Elmer and some others sell several APD products for wide range of applications, like particle detection, laser ranging, molecule detection, optical communications and many others. Commercially available APDs have a quantum efficiency (QE) more than 80%, an excess noise factor $F \approx M^{0.3}$ for reach-through devices and

as low as $F \approx M^{0.17}$ in the case of Slik^{TM} devices fabricated by EG&G. Here M is the gain and F is the excess noise factor.

The arrays made of APDs are currently represented by few examples, whose size is very small (8x8 module made by RMD). Most of commercially fabricated linear-mode APDs are implemented through the reach-through technique [67], which is a vertical structure, incompatible with planar CMOS processes.

Starting from ten years ago, a few linear-mode APDs fabricated in different CMOS technologies have been presented in the literature. Although the performance of commercially available APDs are much better than one obtained by non-optimized CMOS APDs, the low cost of their fabrication and possibility of monolithic integration with readout electronics make them very attractive for several application fields. Table 3.1 shows some characteristics of a selection of CMOS linear-mode APDs presented so far in the literature.

The choice of the proper APD structure leads to the better coupling of integrated readout with the APD. However, when the readout noise is high, an n+/p structure is more suitable especially for visible light wavelengths, due to the lower excess noise factor, which can be remarked by the comparison of two structures proposed by *Stapels et al.* [68], in Table 3.1.

A positive tendency can be noticed for technology transition from $2\mu m$ to $0.35\mu m$. Due to the higher doping levels, the breakdown voltage is reduced. Together with this, a noise level reduction is observed, owing to the hole initiated avalanche. With the doping levels increase, the width of the multiplication region becomes extremely thin. This is the reason why the standard McIntyre theory [66] is no longer valid for the avalanche process description. The results of *Pancheri et al.* [71] work show that the noise factor is getting lower than the one expected by the standard model

Table 3.1: Selected characteristics of available CMOS Avalanche Photodiodes

Ref.	Technology	Type	Breakdown voltage [V]	QE [%]	F @ M = 20
[58]	BiCMOS $2\mu m$	p+/n-well	42	40 @ 500nm	36000 @635nm
[58]	BiCMOS $2\mu m$	n+/p-sub	80	75 @ 650nm	1800 @635nm
[61]	CMOS $0.8\mu m$	p+/n-well	19.5	50 @ 470nm	7 @400nm
[68]	CMOS $0.8\mu m$	n+/p-sub	n.a.	> 60 @700nm	5 @470nm
[68]	CMOS $0.8\mu m$	p+/n-well	25	50 @ 550nm	50 @470nm
[69]	HV CMOS $0.7\mu m$	n+/p-body	11	30 @ 650nm	n.a.
[70]	HV CMOS $0.7\mu m$	p+/n-tub	20.8	41 @ 480nm	8.5 @380nm 100 @650nm
[71]	CMOS $0.35\mu m$	p+/n-well	10.8	23 @ 480nm	4.5 @380nm 6 @560nm
[72]	CMOS $0.18\mu m$	n+/p-well	9.2	22 @405nm 5 @650nm	n.a.
[73]	CMOS $65nm$	n+/p-well	10.7	2 @ 850nm	n.a.
[74]	CMOS $40nm$	p-well/ deep n-well	15.22	57 @520nm 41 @660nm	12 @520nm (M=27)

for electron- and hole-initiated avalanche that can be caused by the dead space effect [75]. In spite of the positive trend in noise performance due to the technology scaling, the quantum efficiency is reduced as well, owing to the degradation of the absorption region depth and an increase in dark current due to the contribution of tunnelling [76].

The first attempt to create an APD-based camera was performed by *Biber et al.* [58], twelve years ago. The APD was implemented in a standard $2\mu m$ BiCMOS technology. The readout circuit was realized through a transimpedance amplifier with a programmable feedback resistor, integrated in each pixel. Such pixel had an optical fill factor of 20% with a round-shaped APD, the outer diameter of which was $48\mu m$. The sensor array consisted of 12 x 24 pixels. The main characteristics of the fabricated APD are shown in Table 3.1. In spite of all efforts, the desired increase in sensitivity has not been achieved. The main reason behind this was in the noise behavior of the APD, which was significantly high due to the technology optimization for transistors, but not for the avalanche photodiode fabrication.

Another application domain that can exploit the monolithic implementation of Avalanche Photodiodes in standard CMOS processes is short-distance optical communication. A monolithic APD-based receiver could be successfully applied in chip-to-chip or board-to-board wide-band optical interconnections. This area stimulates research in CMOS APDs. A number of successful APD implementations has already been demonstrated [72], [77], [78], some of them are also listed in Table 3.1. The research in this field is mainly driven by widening gain bandwidth product of the device, which can reach 1THz [73], but the characterization of noise factor is often missing, whereas it is fundamental in imaging application. In addition, the implementation of APD pixel arrays is not fundamental in communication applications. However, the investigation of different guard-

ring structures and technology scaling and its influence on the performance of CMOS APDs can also be exploited in imaging applications [79], [80].

3.3 CMOS APD implementation and characterization

The major condition for the successful realization of APD-based pixels together with readout electronics in a standard CMOS technology is the accessibility of both terminals of APDs. One terminal is used to apply the bias voltage and the other to connect the readout channel, thus determining the p+/n-well type structure as the most appropriate.

On account of the technology scaling, well doping levels are rising, resulting in a reduction of APD breakdown voltage and an increase in tunneling dark currents, turning from one technology to more advanced one [76].

The dependence of the noise factor on the technology scaling appears to be quite important for further analysis of the feasibility of CMOS APD fabrication. Although only few examples of noise-characterized CMOS APDs were presented in the literature, on the basics of the results, shown by *Pancheri et al.* [71], the trend to the noise reduction can be observed (Figure 3.2). If compared to the prediction of McIntyre theory the measured results show a much lower noise factor, owing to the dead-space effect [75].

The cross section of the edge of an APD manufactured in a standard CMOS technology is depicted in Figure 3.3. The p+ region implemented in an n-well, which is made in a p-type substrate, forms an active area of an APD. The problem of the early edge breakdown prevention has been solved by means of a guard ring proposed by *Rochas et al.* [61]. The idea of the proposed approach is the following: at a close distance d from

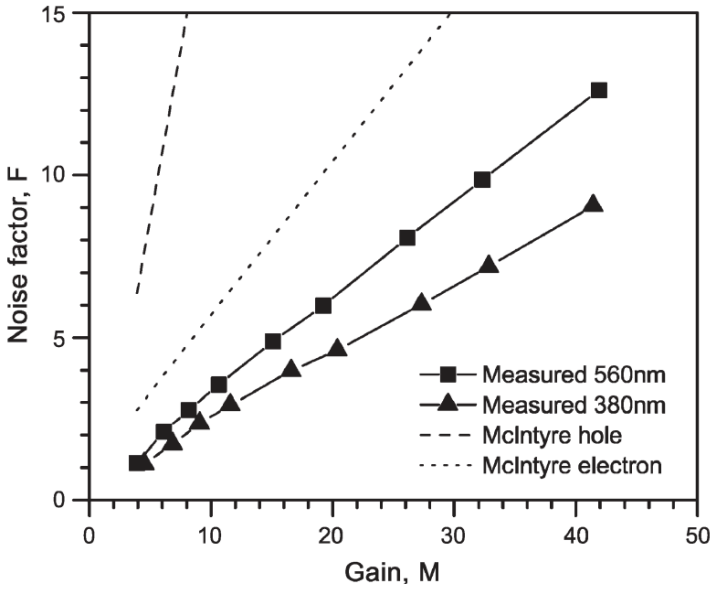

Figure 3.2: Noise factor as a function of multiplication gain at two illumination wavelengths in the APD made from $0.35\mu m$ standard CMOS technology [71]

the central n-well region a separate n-well ring is realized by violating the design rules. Owing to the close implementation of two n-well regions a p-well diffusion forms. At the end of the process, the p-well region is isolated from the substrate due to the merging of the external and internal n-wells through the dopant diffusion. The optimum value of d equal to $0.8\mu m$ was determined through the analyses of a set of test structures with different n-well distances.

The gain uniformity between different APDs needs to be taken into account in the development of an APD array. The increase in multiplication factor results in high deviation in pixels gain values in the array. While the small non-uniformity in an array could be eliminated by pixel-to-pixel calibration, the large non-uniformity is hard to eliminate and this can lead to incorrect operation of a sensor.

An estimation of APD gain uniformity was made for a set of identical APDs fabricated in a $0.35\mu m$ technology with the structure described

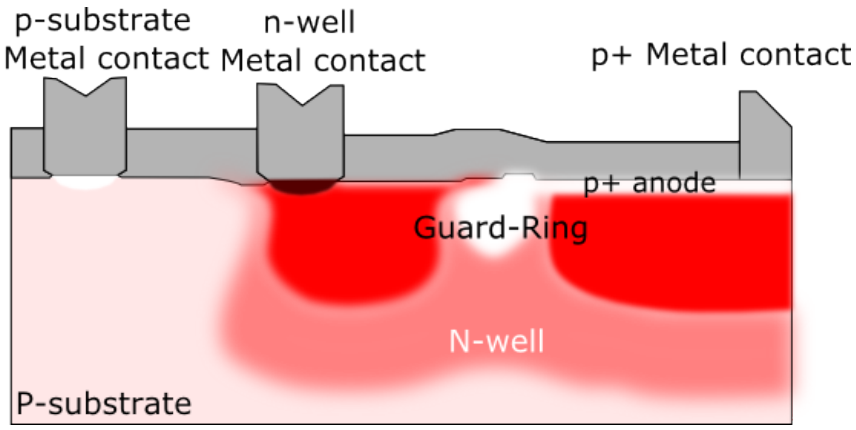

Figure 3.3: Schematic cross section of the APD border [61]

above. The gain as a function of voltage was measured for different APDs in the same die and for several dies. The standard deviation, representing gain non-uniformity, as a function of average gain is presented in Figure 3.4 [81]. As can be seen from the graph the gain non-uniformity of APDs fabricated on different dies is 10 times higher than the gain non-uniformity

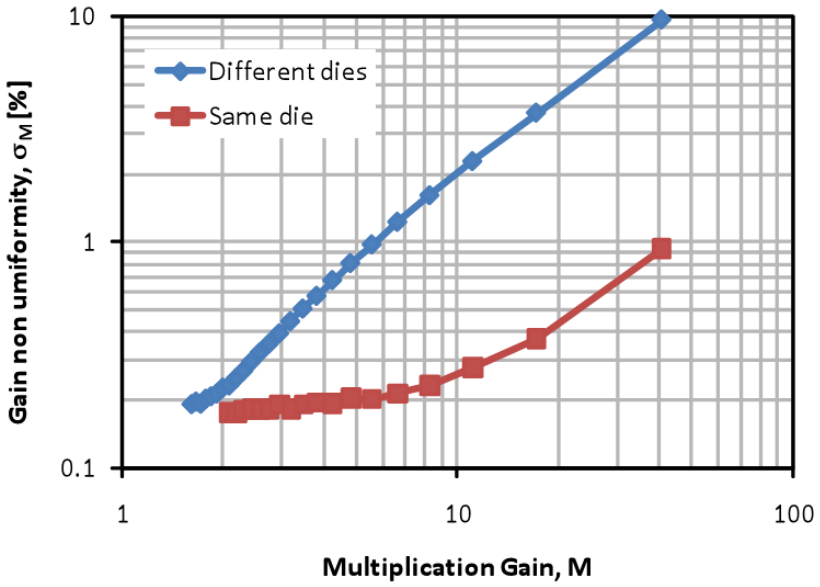

Figure 3.4: Gain uniformity characteristic of $0.35\mu m$ CMOS APDs fabricated on the same die and on different dies in the same production batch

for APDs which are parts of the same die. The Figure 3.4 shows that for a

gain equal to 40, non-uniformity is lower than 1%. This value constitutes a good background for linear-mode APD array fabrication in the considered $0.35\mu m$ process.

3.4 CMOS APD application for Indirect TOF measurement

The implementation of avalanche photodiode pixel array for Indirect TOF distance measurement was enabled by the successful realization of a low-noise APD in a standard CMOS technology [71]. Since the photocurrent multiplication of an APD depends on the applied bias voltage, the modulation of an APD bias voltage results in the modulation of the internal multiplication factor (Figure 3.5). This property makes avalanche photodiodes usable as electro-optical mixers, which can be employed in phase-shift TOF measurements. Synchronous modulation of both the light signal incident on the APD and APD bias voltage produces a generated current proportional to the correlation function between two signals (Figure 3.6). In Chapter 2 several examples of different opto-electrical demodulating devices have been described. The general operational principle of the APD demodulator is the same as for the other devices used in I-TOF distance measurements [82].

The application of a modulated bias voltage to one of the APD terminals gives a modulated avalanche gain $M(t)$:

$$M(t) = cos(\omega t) \tag{3.4}$$

The incident modulated light signal $Popt(t)$ can be represented as:

$$Popt(t) = 1 + A \cdot cos(\omega t - \varphi) \tag{3.5}$$

where A is a demodulation amplitude and φ is the phase shift with respect to $M(t)$. In this condition, the detector current is proportional to the

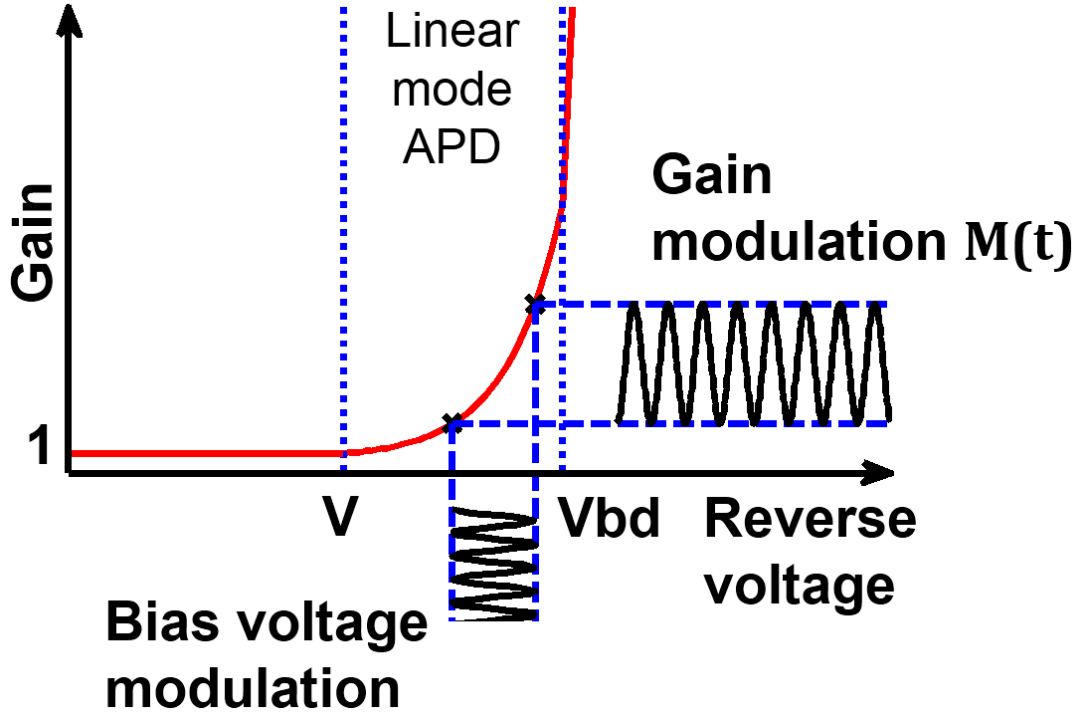

Figure 3.5: Linear-mode APD gain modulation

correlation function $c(\tau)$:

$$c(\tau) = Popt(t) \otimes M(t) = \\ (1 + A \cdot cos(\omega t - \varphi)) \otimes cos(\omega t) = A/2 \cdot cos(\varphi + \omega\tau) \tag{3.6}$$

between the received modulated light signal $Popt(t)$ and internal gain $M(t)$ of the APD, where τ is an arbitrary time delay applied between $Popt(t)$ and $M(t)$.

By measuring the $c(\tau)$ at four different phase shift values: $\omega\tau_1 = 0°$, $\omega\tau_2 = 90°$, $\omega\tau_3 = 180°$ and $\omega\tau_4 = 270°$ it is possible to calculate the phase φ and amplitude A of received optical signal $Popt(t)$. Taking into account that received optical signal contains background light information, an additional offset B must be summed to the correlation function $c(\tau)$.

$$C(\tau_1) = A/2 \cdot cos(\varphi) + B$$

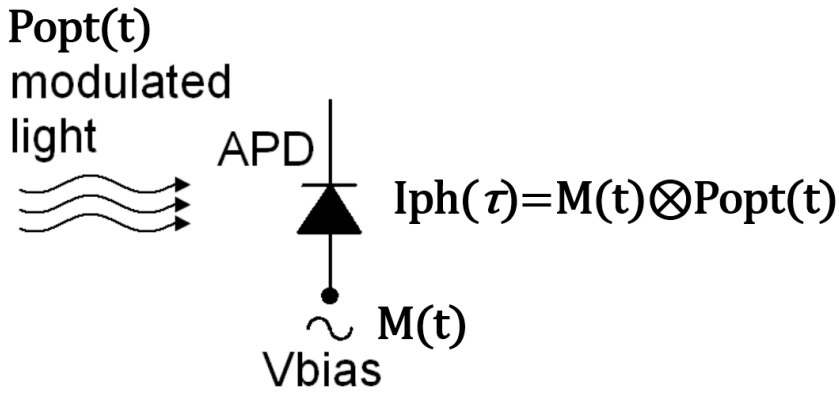

Figure 3.6: APD operation

$$\begin{aligned} C(\tau_2) &= A/2 \cdot cos(\varphi + 90°) + B \\ C(\tau_3) &= A/2 \cdot cos(\varphi + 180°) + B \\ C(\tau_4) &= A/2 \cdot cos(\varphi + 270°) + B \end{aligned} \tag{3.7}$$

Once the correlation function at four time shifts $\tau_1 - \tau_4$ is known, the phase φ and amplitude A can be determined:

$$\varphi = atan\frac{C(\tau_4) - C(\tau_2)}{C(\tau_3) - C(\tau_1)} \tag{3.8}$$

$$A = \frac{\sqrt{(C(\tau_4) - C(\tau_2))^2 + (C(\tau_3) - C(\tau_1))^2}}{2} \tag{3.9}$$

Thereby, in order to calculated distance D four acquisitions are required with $\pi/2$ phase shift in the optical signal. D is proportional to the phase shift φ:

$$D = c \cdot \frac{\varphi}{4\pi f_m} \tag{3.10}$$

Here c is the speed of light and f_m is a modulation frequency.

Figure 3.7 illustrates the average output current dependence on phase difference φ. Amplitude and Offset can be calculated from equations (3.11-

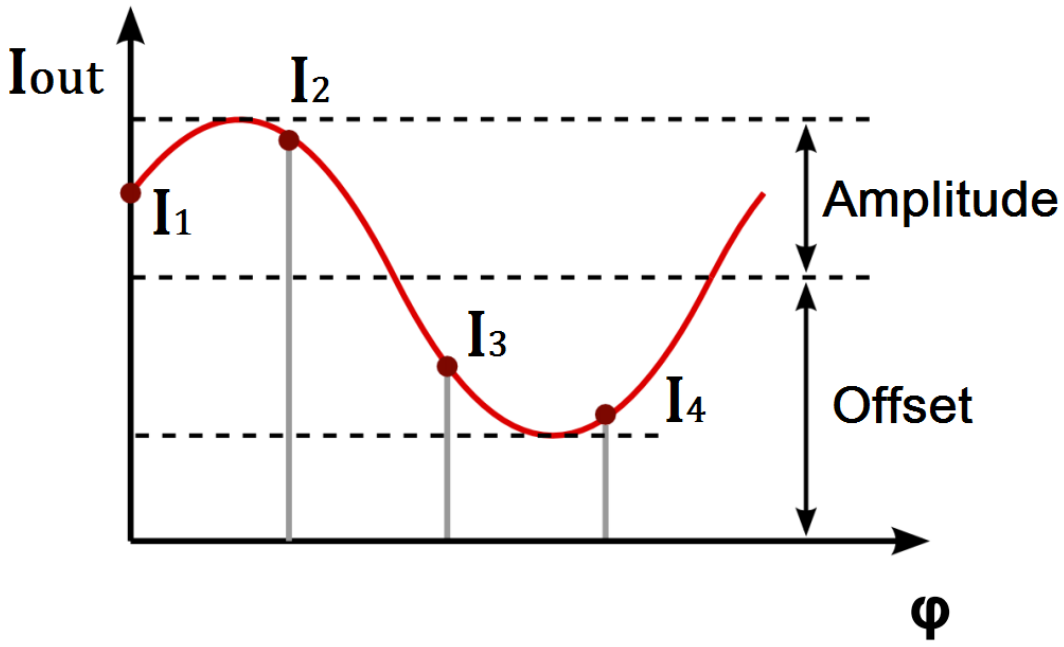

Figure 3.7: Average output current dependence on the phase difference between light signal and modulation signal

3.12).

$$Amplitude = \frac{\sqrt{(I_4 - I_2)^2 + (I_3 - I_1)^2}}{2} \tag{3.11}$$

$$Offset = \frac{I_1 + I_2 + I_3 + I_4}{4} \tag{3.12}$$

The quality of the demodulating device can be represented by demodulation contrast C_D defined as the ratio between demodulated amplitude and offset.

$$C_D = \frac{Amplitude}{Offset} \tag{3.13}$$

Demodulation contrast should be as high as possible in order to achieve large signal amplitude. That will provide a good Signal-to-Noise Ratio for a high phase accuracy [27]. The SNR in demodulation pixel is defined as the ratio between demodulated amplitude and noise in the measurement

of demodulated amplitude.

$$SNR = \frac{Amplitude}{AmplitudeNoise} \tag{3.14}$$

These two important parameters will be examined in pixel and sensor characterization in Chapters 4 and 5.

Chapter 4

Test Pixel Characterization

This chapter reports experimental results obtained on a test pixel to verify the principle of phase detection by APD gain modulation. This pixel was conceived to test the APD operation in high-sensitivity imaging application. That was the main reason under not optimal pixel configuration for gain modulation operation. However, it was a good experimental starting point for preliminary test the idea of phase detection by APD gain modulation. Pixel design, simulation and main performance are also shown in this chapter.

4.1 Phase sensitive pixel

Several advanced imaging applications require phase-sensitive light detection at a pixel level. Among these applications, the most appealing one from the industrial point of view is Time-of-Flight 3D imaging, for which several commercial products based on phase-sensitive pixel arrays are already being commercialized [83]. In the last decade an increasing research effort is being made to improve the sensor performance and functionality and to reduce the overall pixel cost [23], [84], [85], [43], [86], [87], [49], [88], [89], [90]. Besides 3D imaging, the biomedical field would also benefit from the development of high-performance phase-sensitive image sensors

suitable for Fluorescence Lifetime Imaging (FLIM) applications. FLIM generally requires modulation frequencies higher than those typically used in 3D range cameras, and the light to be detected is more often in the blue-green region of the visible spectrum [91].

Mostly unexplored phase-sensitive pixel concept is the use of a gain-modulated Avalanche Photodiode (APD) as an intrinsic electro-optical mixer. Discrete APDs are commonly used in scanning systems for TOF ranging [92], offering excellent performance, but high noise of CMOS integrated APDs has so far prevented the implementation of monolithic pixels with satisfactory performances.

4.1.1 Operation principle

The proposed pixel exploits the principle of APD gain modulation to detect phase changes in modulated light signal incident on the device. The pixel is composed of a CMOS APD, whose cathode is connected to a charge integrating amplifier. The simplified pixel structure is shown in Figure 4.1.

The APD is reverse biased with a DC voltage close to breakdown. This

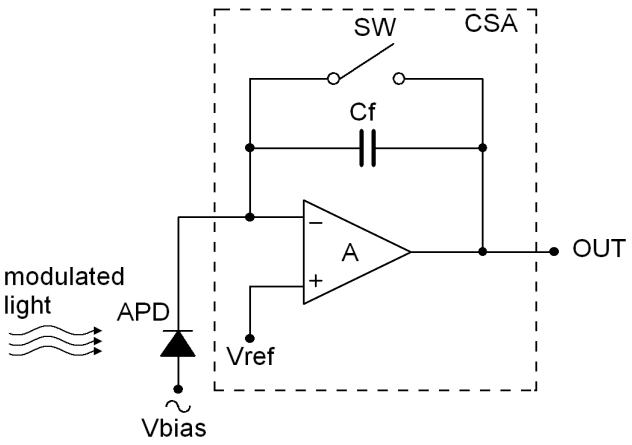

Figure 4.1: Block diagram of the phase sensitive pixel

voltage is superimposed to a modulation voltage synchronous with emitted light. Due to the modulation of the APD bias voltage, APD internal gain M is also affected by the modulation. This condition allows the detector to measure the correlation function $c(\tau)$ between the received modulated light signal $Popt(t)$ and internal gain $M(t)$ of the APD (see equations (4.1-4.3)).

$$Popt(t) = P_0 + \Delta P_0 \cdot cos(\omega t - \varphi) \tag{4.1}$$

$$M(t) = M + \Delta M \cdot cos(\omega t) \tag{4.2}$$

$$c(\tau) = Popt(t) \otimes M(t) = P_0 \cdot M \cdot Tint + 1/2 \cdot \Delta P_0 \cdot \Delta M \cdot Tint \cdot cos(\omega\tau - \varphi) \tag{4.3}$$

where P_0 and M are the DC values of the optical signal and internal gain time variable with amplitudes ΔP_0 and ΔM respectively, φ is the phase delay, $Tint$ is the integration time and τ is an arbitrary time delay applied between $Popt(t)$ and $M(t)$. The correlation current signal generated at the cathode of the APD is integrated on a feedback capacitance, Cf, of the Charge Sensitive Amplifier (CSA). The output voltage of the CSA is proportional to the average current flowing through the APD during its illumination.

4.1.2 Phase sensitive pixel design

In this test pixel the low-noise APD fabricated in $0.35\mu m$ standard CMOS technology is employed. The p+ region implemented in an n-well, which is made in a p-type substrate, forms an active area of the APD (see Figure 4.2). The problem of the early breakdown at the edges of the structure has been solved by means of a guard ring realized by merging of two separate n-well regions made at a close distance d from each other. Owing to this merging the isolation of p-well diffusion that appears between two

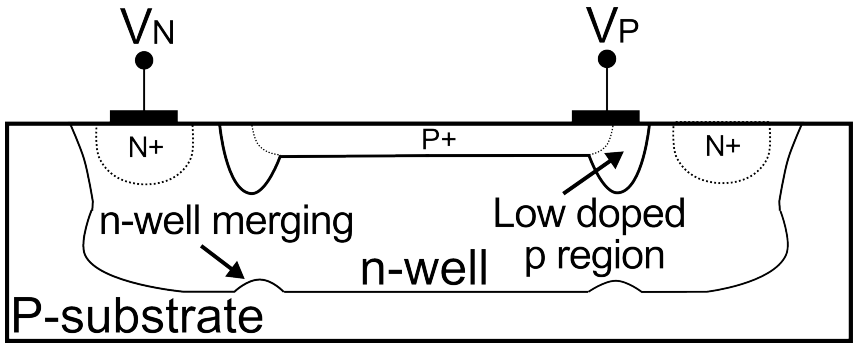

Figure 4.2: CMOS APD cross section

close n-wells from a p-type substrate is carried out. More details on the performance can be found in the reference work [71]. Main characteristics of the APD used in the pixel are listed in Table 4.1.

Table 4.1: Main characteristics of CMOS APD used in the pixel

Parameter	Value
Technology	$0.35\mu m$ standard CMOS
Size	$100\mu m$ in diameter
Type	p+/n-well
Guard ring	p-well
Breakdown voltage [V]	10.8
Quantum Efficiency [%]	23 @ 480nm
Noise Factor @ M=20	4.5 @ 380nm, 6 @ 560nm

Design and simulation of the APD phase sensitive pixel was performed using Cadence circuit simulation program [93]. A model of the APD based on experimental I-V characterization, which includes dark current and internal multiplication effects, was implemented in the simulator. More details on the model will be given in the next chapter. The evaluated capacitance of the APD, whose active area is $100\mu m$ in diameter, is 2.9pF. Since the APD is realized in an n-well, an n-well over p-substrate diode with a capacitance of 446fF was also included in the model.

The CSA was realized with a single-ended Operational Transconduc-

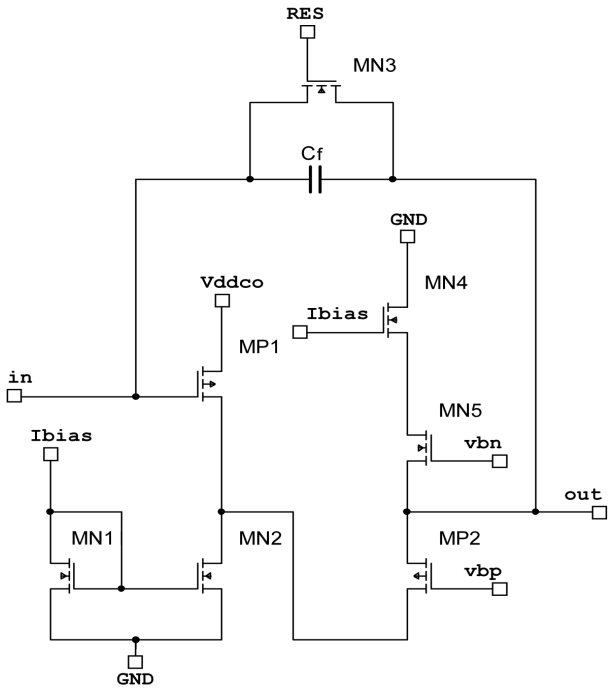

Figure 4.3: Charge sensitive amplifier circuit

tance Amplifier (OTA), a feedback integration capacitor, $Cf = 23$fF, and a reset transistor. The OTA, made of six transistors, has a folded cascode configuration in order to obtain a high gain in a compact circuit (Figure 4.3). The DC gain value of the OTA is 63.9dB, the gain bandwidth product is equal to 969MHz and noise of 0.96mV was estimated from OTA simulations [94].

Table 4.2: In-pixel Amplifier Characteristics

Parameter	Value
Gain	63.9dB
GBWP	969MHz
f-3dB	2MHz
N transistors	7
Integration capacitance	23fF

In order to assess the phase-sensing capability of the proposed pixel,

analysis of the CSA output with simultaneous modulation of APD anode voltage and photocurrent signal was performed. In the simulations, an un-multiplied photocurrent having 10pA amplitude, 10pA DC value and 20MHz frequency was imposed to the APD. The modulation signal applied to the anode of the APD had 2V amplitude, and -8.5V DC level and the same frequency as the photo-generated current. Simulation results of the APD pixel are presented in Figure 4.4a,b.

In the simulations, the maximum value of the APD bias voltage does not exceed the breakdown value, thus maintaining the APD in the linear mode of operation. The simulation was repeated with phase delay between modulation voltage and photocurrent changing from 0 to 360 degrees with a linear step of 15 degrees. Top inset of Figure 4.4a shows the simulated pixel output as a function of time at two different phase delay settings 0° and 180°. The integration time is $12\mu s$. In the middle of the integration time the oscillation of the amplifier in the presence of APD modulation is observed. This oscillation occurs due to a very high gain factor of the amplifier, which is advantage for high-sensitive pixel application, but results in distortion of the output during modulation. Next graph represents Reset signal, then goes APD bias voltage signal with modulation interval at the centre of the integration time. Last inset illustrates two light signals with 180° phase shift. The dependence of the output voltage on the applied phase delay can be observed at the end of the integration time after modulation interval. The oscillation of the amplifier does not influence the phase measurement because the useful information is contained in the DC component of the correlation current.

The voltage difference between the output value at the end of the integration time and the value after reset is reported in Figure 4.4b as a function of phase delay. A sine-wave behavior is observed, as predicted by equation (4.3), thus demonstrating the viability of the proposed pixel

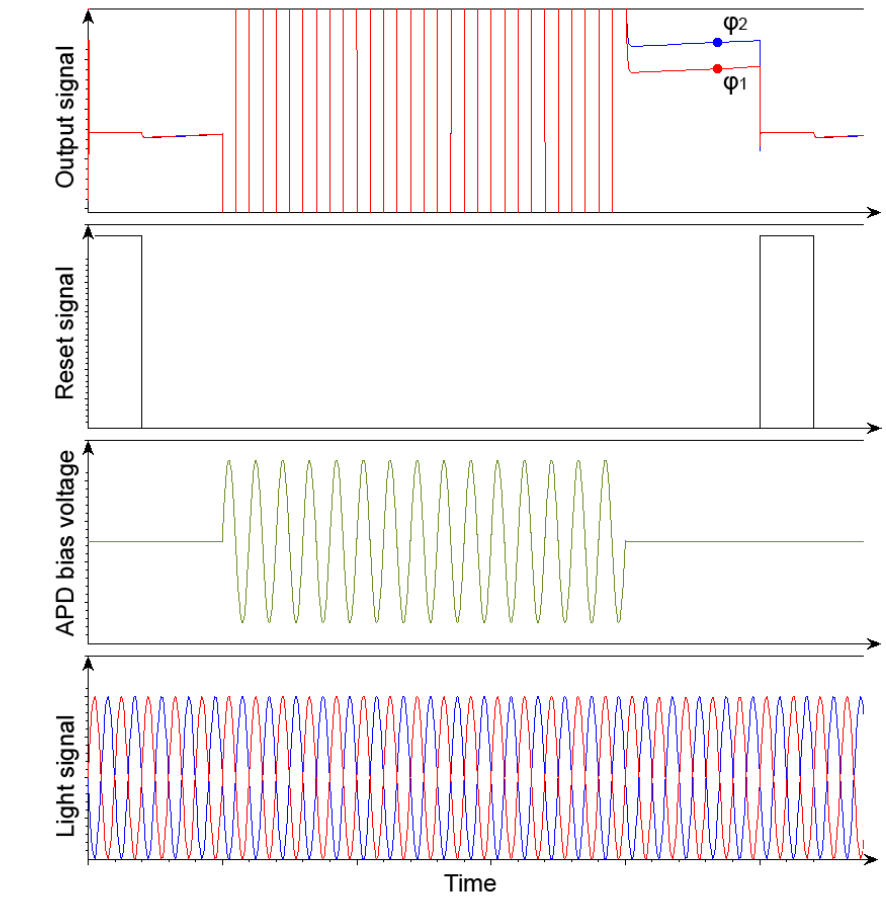

a

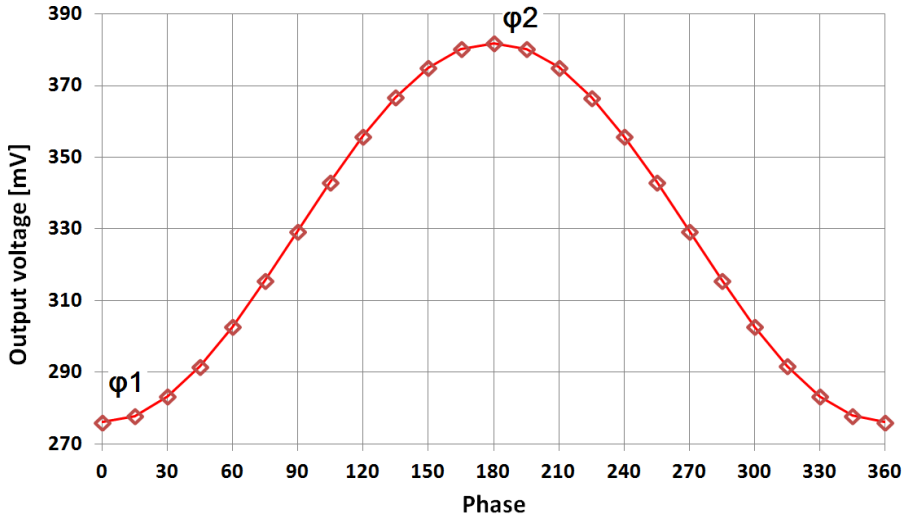

b

Figure 4.4: Simulation results of a phase sensitive pixel

structure in phase detection applications.

The phase sensitive pixel design was implemented in a commercial 0.35 μm CMOS technology. It consists of an APD having a 100μm light-sensitive area and a charge amplifier realized with seven transistors and integration capacitance that occupies an area of 90$\mu m \times 73\mu m$. The integration capacitance has a value of 23fF and size of $5\mu m \times 5\mu m$. The APD shape is circular, but an octagonal metal shield was used to reduce the number of DRC violations associated with circular shapes in the design. Figure 4.5a,b illustrates the elementary cell layout together with the microphotograph of the fabricated pixel. Table 4.3 lists selected characteristics of the phase-sensitive pixel.

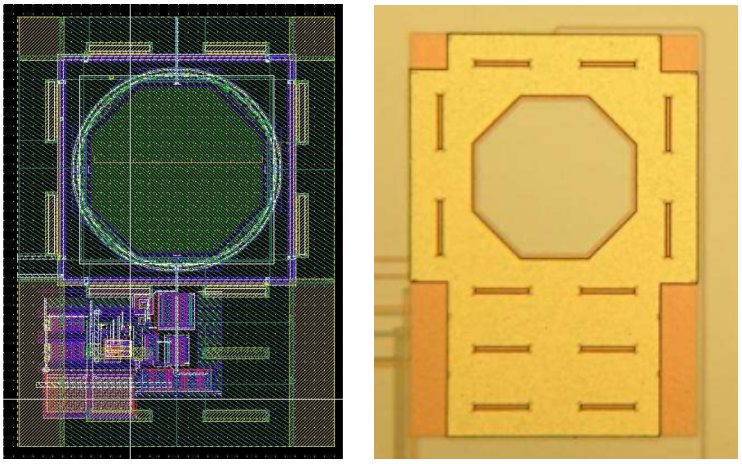

a b

Figure 4.5: Phase sensitive pixel layout and microphotograph

Table 4.3: Phase Sensitive Pixel Characteristics

Parameter	Value
Technology	0.35μm CMOS
Active area	100μm in diameter
Fill factor	54%

4.2 Experimental results

This section is aimed to describe measurements performed on a test pixel containing single Avalanche Photodiode (APD) of $100\mu m$ in diameter fabricated in $0.35\mu m$ CMOS technology, hosted on a board that has all necessary periphery for readout purpose. Measurements were made to perform full characterization of the APD pixel with constant light as well as modulated light. Based on simulations performed in Cadence software, measurements were made with modulated light signal and modulated APD bias voltage with variable time delay in order to estimate dependence of the output signal on time delay between two input signals.

4.2.1 Equipment

Tools used to perform measurements are listed in Table 4.4. Board 7 was fabricated to control the APD pixel readout process and applied reference voltages.

Table 4.4: Measurement Equipment

Nn	Tool type	Model
1	Oscilloscope	LeCroy Wavepro 7200
2	Microcontroller board	Mbed NXP LPC1768
3	Power supply	GPC-3030
4	Power supply	Agilent E3620A
5	Function generator	Tektronix AFG3102
6	Multimeter	Philips PM2525
7	Test Board	

4.2.2 Measurements with constant light

These measurements were performed in order to evaluate pixel output signal and noise as a function of APD bias voltage. Measurements were made in two conditions: without light, to check dark signals of the APD, and with the presence of light. A blue LED with 425nm wavelength was used as a light source. Avalanche photodiode bias voltage was reversed and increased from 0 to -9.4V with a certain step. The signal from APD was acquired through an output of Board 7 and registered on the oscilloscope. Mbed NXP board generated a reset signal with a period of $15\mu s$ as well as other control signals required for APD pixel acquisition. Measurement setup for two cases is schematically shown on Figure 4.6a,b.

Two output values of interest are readout: just after Reset signal (V_1)

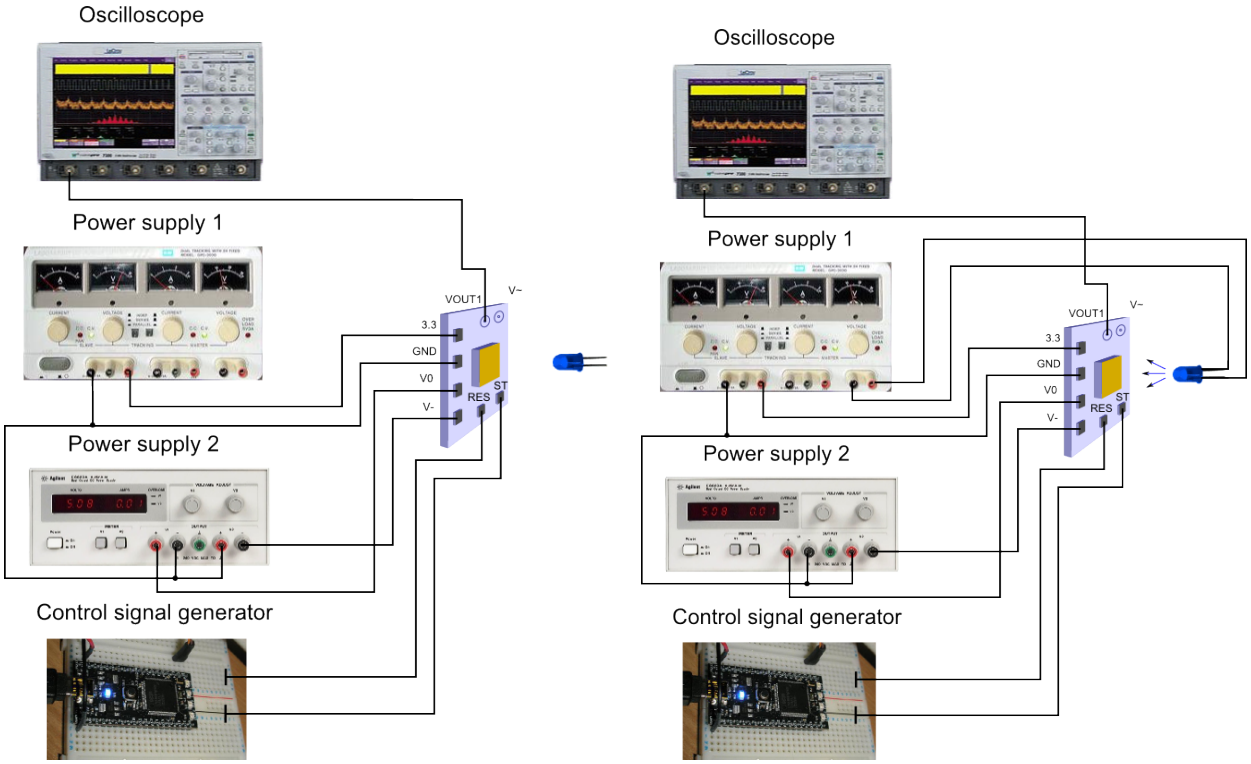

a b

Figure 4.6: Phase sensitive pixel measurement setup: a - without light, b - with the presence of light

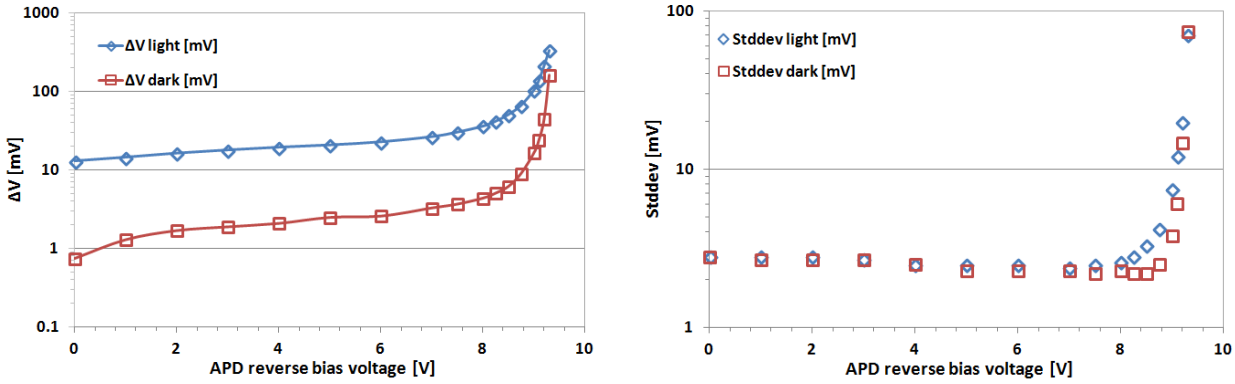

a b

Figure 4.7: Phase sensitive pixel measurement in light and dark conditions: a - output signal as a function of APD bias voltage, b - standard deviation as a function of APD bias voltage

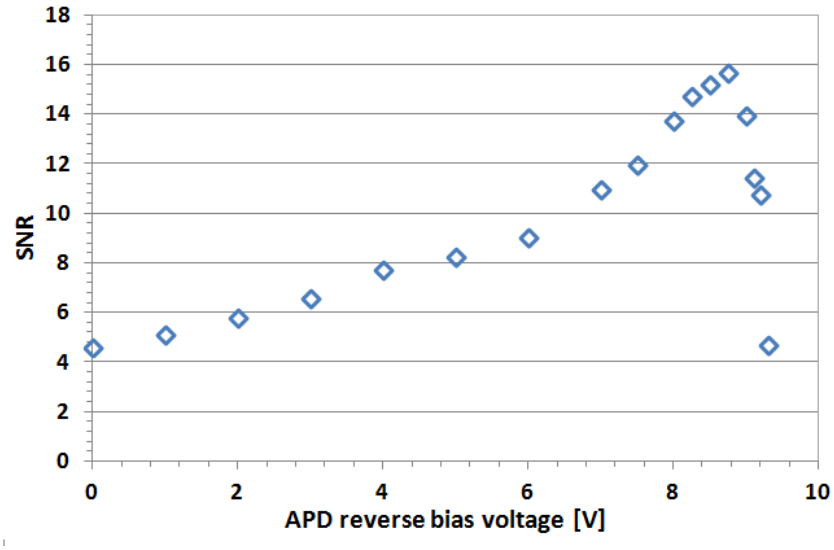

Figure 4.8: Phase sensitive pixel measurement of SNR

and just before next Reset signal (V_2). The important data of difference between two values ($\Delta V = V_2 - V_1$) and standard deviation of this difference were registered with the help of the oscilloscope and further processed on a PC. Experiments were performed several times and showed high repeatability of the results. Figure 4.7 shows pixel output signal and noise as a function of APD bias voltage in logarithmic scale. Signal to Noise

Ratio as a function of APD bias voltage is presented in Figure 4.8. SNR experiences its maximum at -8.75V, where the signal is high and multiplication noise factor of the APD is still low. The multiplication factor M at -8.75V APD bias voltage is equal to 5 and Noise factor F is around 2.

Noise measurements

One of the most important characteristics of the pixel is the output noise, which was measured as the standard deviation of the output signal difference between the value at the end of integration and the reset value, that is a Correlated Double Sampling (CDS) operation (Figure 4.9). The measurements were carried out at different light intensities for two values of the APD anode bias voltage, 0 and -8.9V. The measured output noise in the dark was 2.4 and 2.8mV for 0 and -8.9V bias voltages respectively.

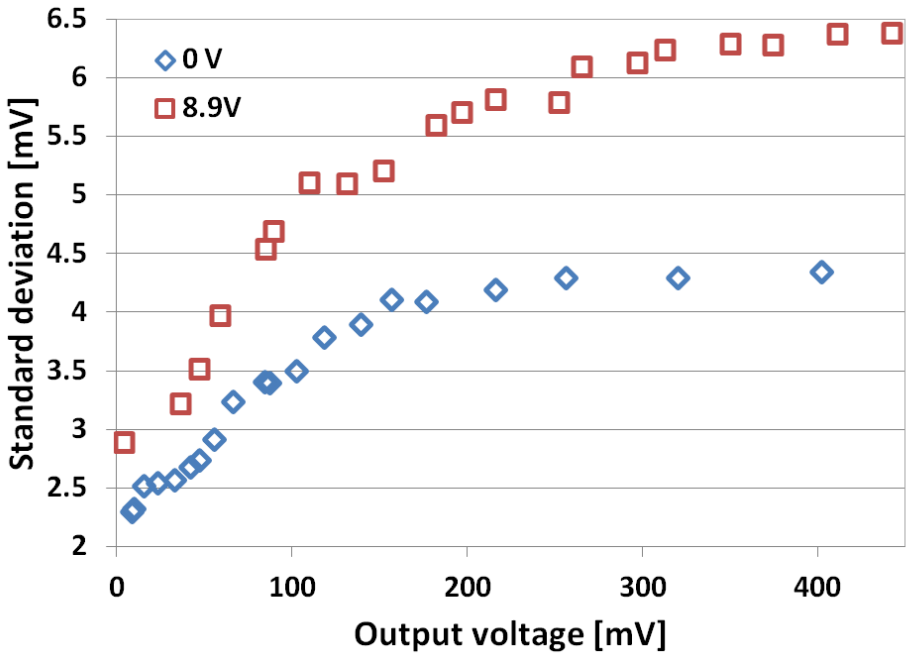

Figure 4.9: Output voltage noise as a function of output signal

The noise values 4.1 and 5.6mV were measured for the same bias voltages at 200mV output voltage [95]. In the case of 0V biasing, the noise fac-

tor increases with the light intensity growing due to the shot noise, while in the second case there is also the additional contribution of the APD multiplication noise.

4.2.3 Phase shift measurement

Preliminary measurements

The main attention in the pixel characterization was focused on the study of the output voltage evolution in response to sine wave light and bias voltage modulation. The results of this measurement are of great importance for concept validation inasmuch as they can prove the possibility for the APD pixel to work as an electro-optical demodulator.

The simplified experimental setup for the phase delay measurements is illustrated in Figure 4.10. It consists of a light source, a board hosting the pixel with the necessary peripheral electronics and a two-output signal generator Tektronix AFG3102, which produces two synchronous light modulation signals for the pixel and the light source with variable time delay. Both signals were set to the same frequency of 20MHz.

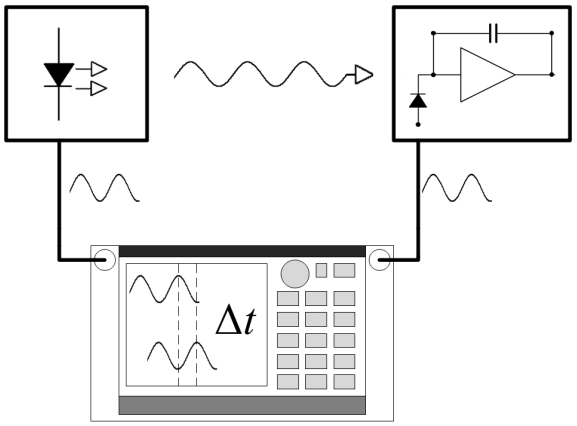

Figure 4.10: Set-up for phase delay measurement

In order to characterize the operation of the pixel it was necessary to analyze the output of the charge amplifier during the integration period,

in particular, to calculate the voltage difference of the output signal under time delay variation between two signals. In the measurements, an integration time of $14\mu s$ was set, with a reset time of $2\mu s$. A double sampling operation was performed externally to measure the voltage difference between the output value at the end of integration and the reset value. A blue light emitting diode (LED) with the wavelength of 425nm and 20mW nominal power was used as a light source during the measurements. The LED with a resistance of 50Ω in series was connected to the signal generator and was driven by a sinusoidal signal, obtaining an optical signal with 80% modulation depth. The anode contact of the APD was connected to the same signal generator in order to properly synchronize two sinusoidal signals. Table 4.5 shows the settings applied to the pixel and illuminator.

Table 4.5: Pixel and Illuminantor Settings

Pixel settings:	
Bias voltage offset	-8.67V
Modulation amplitude	2V
Modulation frequency	20MHz
Waveform	sine
Illumination settings:	
Source	Blue LED
Wavelength	425nm
Nominal power	20mW
Modulation frequency	20MHz
Modulation depth	80%

The bias voltage offset was set to -8.67V and peak-to-peak voltage equal to 4V. Such high value of the bias voltage was required to achieve proper internal gain modulation and to compensate the voltage variation at the

cathode contact of the APD. The modulation of APD anode caused saturation of the amplifier and in order to overcome this problem a modulation window inside the integration window was defined, while outside this time window APD voltage was maintained at the constant offset value. The same behaviour has been observed during pixel simulation. However, results of the simulation have not been spoiled by amplifier oscillation. Thus, this behaviour does not interfere with the measurement and the useful information is still contained in the output signal at the end of integration time after output stabilization.

Figure 4.11 represents the output signals observed on an oscilloscope during the experiments. Blue wave (top) shows the pixel output and red wave (bottom) is the Reset signal. The left inset shows the case of the modulated optical signal and the constant bias voltage applied to the APD anode. The output voltage difference was measured for different values of delay between optical and electrical modulation signal, at 5ns step up to a total of 50ns, thus covering 360° of phase delay. The output signals for two cases of time delay between input signals are shown on the middle and right insets of Figure 4.11. The voltage jump at the middle of the integration time represent the influence of applied modulation on the output signal. As was discussed before the in-pixel amplifier experience oscillation, however,

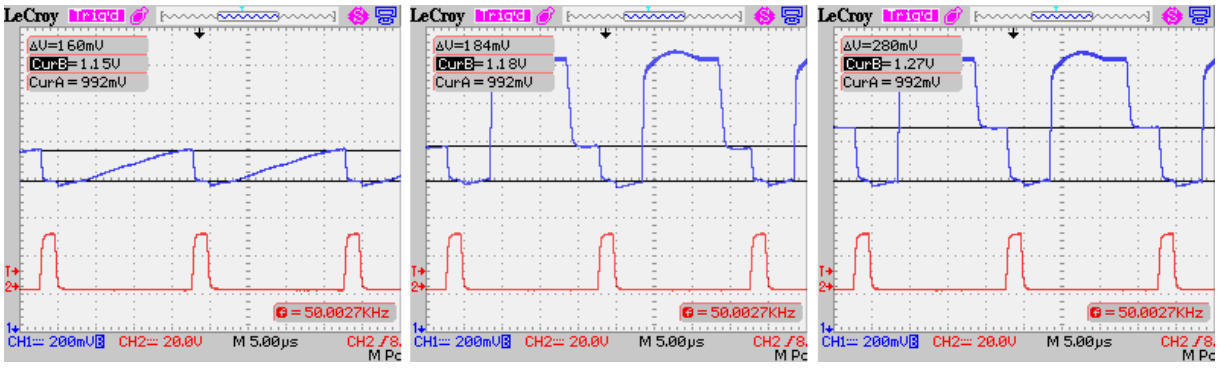

Figure 4.11: The output signals observed on an oscilloscope

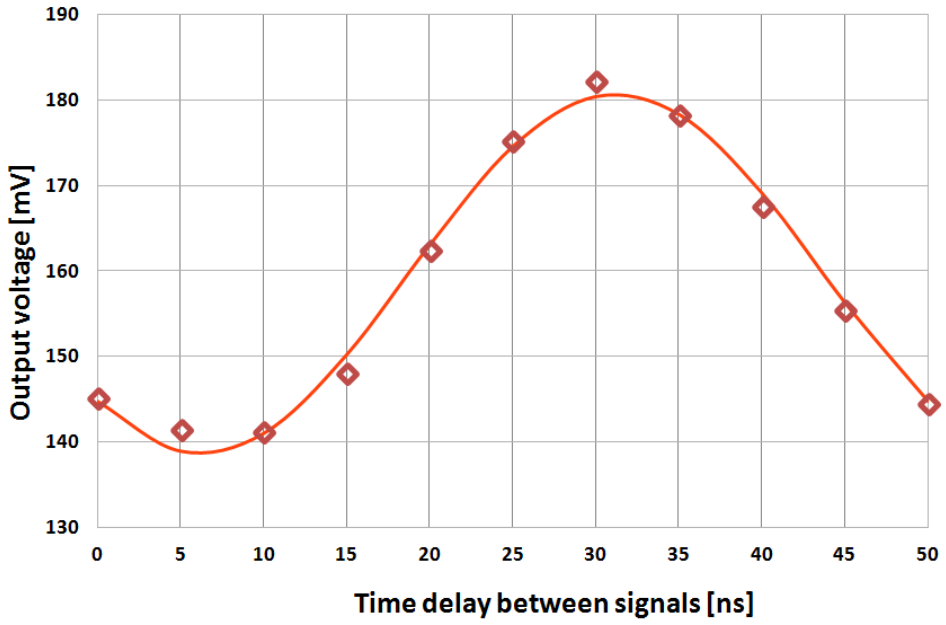

Figure 4.12: Output voltage dependence on time delay between optical and electrical modulation signals

on the oscilloscope it is not visible due to low-pass filer and low bandwidth of the tool. Figure 4.12 presents the measured voltage difference as a function of time delay applied to the modulated light signal.

Figure 4.12 shows that the difference in the output voltage is related to the phase with a sinusoidal relation, as it was predicted by the simulations reported in subsection 4.1.2. The curve is horizontally shifted with respect to the curve obtained from the simulations, because of the phase delays introduced by the different elements and cables of the experimental setup. These measurements validate the simulated pixel operation, and confirm the possibility of integrating monolithic phase-sensitive pixels based on linear APD gain modulation principle.

Extended pixel characterization

To further evaluate phase-sensitive detection, a measurement campaign was performed with modulated light signal and modulated APD bias volt-

age at high modulation frequency. Modulation signals were synchronous and came to the LED and APD from a two-output function generator Tektronix AFG3102. The modulation interval within integration time was provided by a microcontroller board MBed NXP. Figure 4.13 illustrates the measurement setup.

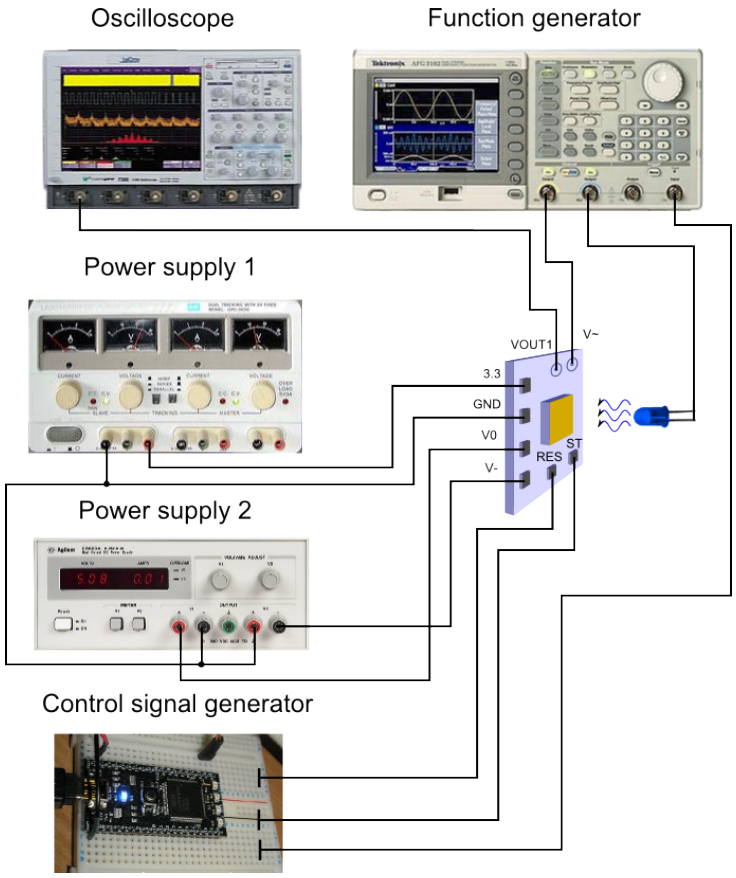

Figure 4.13: Phase sensitive pixel measurement setup

Generator settings for LED and APD are listed in Table 4.6. Modulation frequency was increased with respect to measurements reported in Section 4.2 to 50MHz.

Time delay between two modulated signals was set manually from 0 to 20ns with a step of 1ns, thus covering a complete modulation period ($T = \frac{1}{50MHz} = 20ns$). On Figure 4.14 APD output voltage dependence on time delay is represented for -8.6V of APD DC offset together with sine-

Table 4.6: APD and LED settings

APD modulation voltage settings:	
Parameter	Value
Frequency	50MHz
Offset	-8.6V
Amplitude p-p	3.5V
Waveform	sine
LED modulation settings:	
Parameter	Value
Frequency	50MHz
Offset	2V
Amplitude p-p	3V

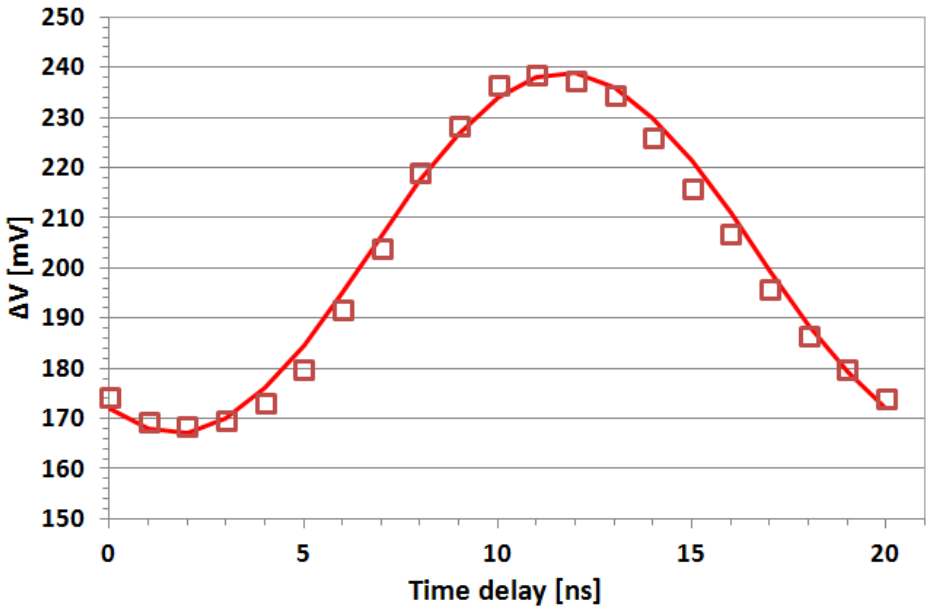

Figure 4.14: Phase sensitive pixel measurement of output dependence on time delay at 50MHz

wave fitting. As can be seen the dependence has sine-wave shape as was observed during measurements performed at 20MHz frequency.

Another measurement campaign was conducted to estimate the influ-

ence of DC offset and modulation amplitude on a demodulation contrast. Demodulation contrast was estimated from measurements by following equation (see Chapter 3 for more details):

$$C_D = \frac{\Delta V_{max} - \Delta V_{min}}{\Delta V_{max} + \Delta V_{min}} \tag{4.4}$$

Measurements were performed for offset values from -8.4 to -8.6V with 0.1V step and amplitude values 2V, 3V and 3.5V. The highest demodulation contrast of 17.2% was reached at 8.6V of APD DC offset and 3.5V amplitude.

Considering from the previous measurement two values of time delay 2ns and 11ns as the minimum and maximum of sine-wave output signal, respectively, the dependence of demodulation contrast on offset value variation of APD bias voltage was investigated. For these two values of time delay, APD bias voltage was changed from 0 to -9.3V. In Figure 4.15 output voltage dependence on APD bias for two cases is shown. As can be seen the difference between minimum and maximum values becomes notable at APD offset voltages from -8 to -9V, which is a range close to the breakdown. Figure 4.16 shows demodulation contrast in percent as a function of APD offset bias voltage, together with SNR of a peak-to-peak demodulated amplitude signal. These graphs show that though there is a maximum of demodulation contrast equal to 18% at -8.75V, the SNR experience its maximum earlier around -8.5V, thus optimum operation of the pixel is between these two values.

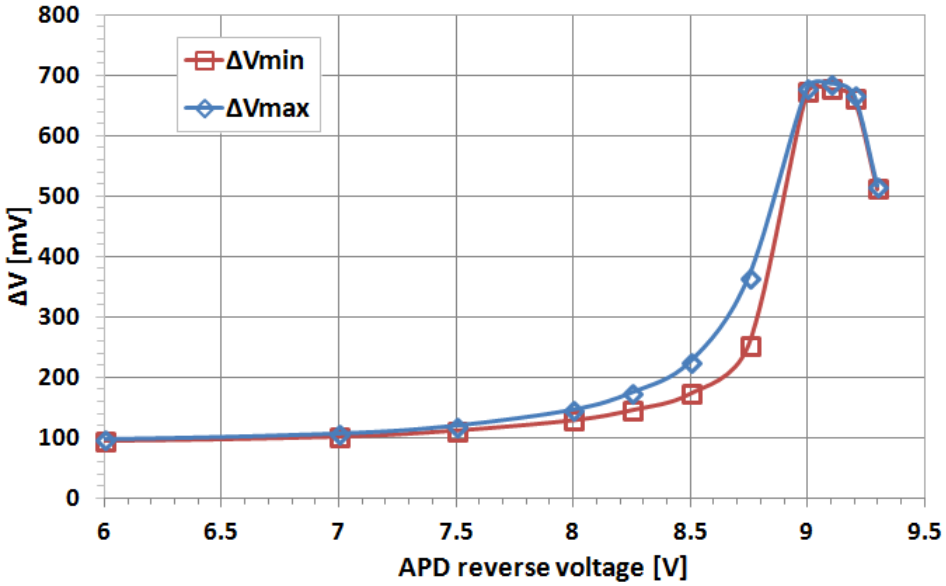

Figure 4.15: Phase sensitive pixel measurement of output voltage dependence on applied DC bias voltage of APD for two time delays

Parameters that limit demodulation contrast can be partially attributed to the employed light source that is not fast enough for that frequency. Hence, in order to proceed with measurements on the pixel, blue LED light source has to be replaced. Another reason that can explain the low contrast is the APD cathode connection to the amplifier input. With this circuit topology, electrons generated in the n-well/substrate junction are integrated by the charge amplifier, contributing to the output signal offset, but not to the demodulated signal.

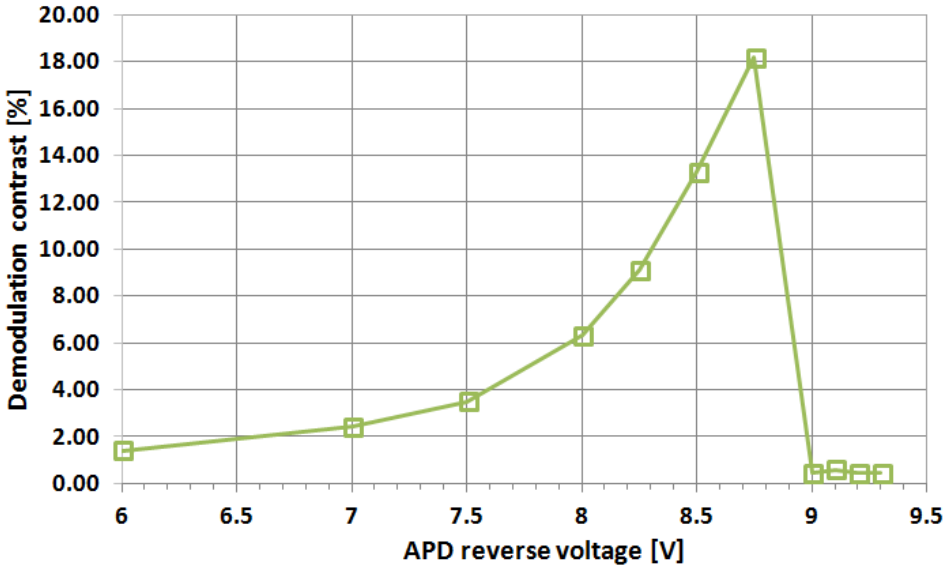

a

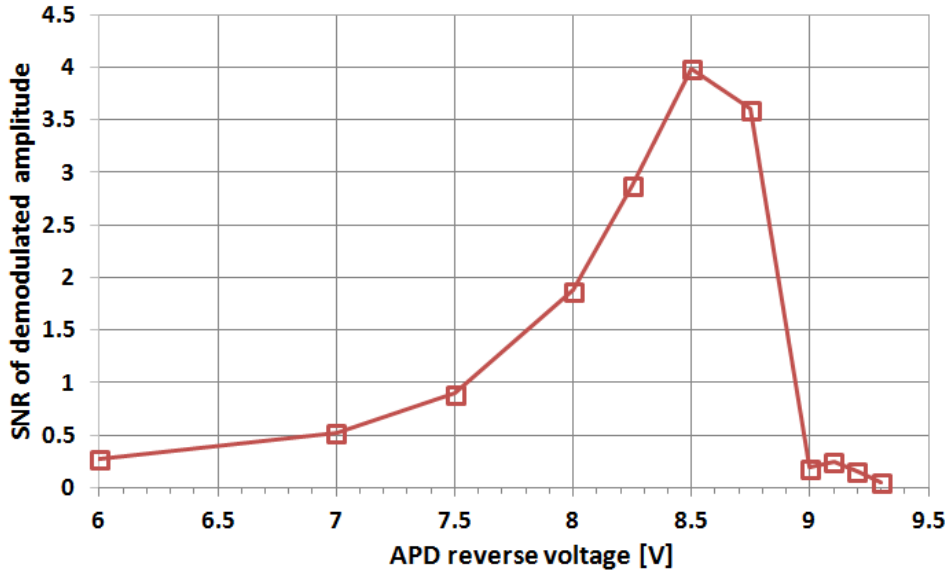

b

Figure 4.16: Phase sensitive pixel measurement at 50MHz: a - demodulation contrast as a function of applied DC bias voltage of APD; b - SNR of demodulated amplitude as a function of applied DC bias voltage of APD

Demodulation contrast
measurements at 100MHz modulation frequency

At first blue LED was replaced with ultraviolet LED working at 400nm wavelength. The reason behind the move into lower wavelength is that avalanche region of a CMOS APD is allocated close to the surface, thus lower wavelength light source should be more efficient. The setup for this measurement is the same illustrated in Figure 4.13 except for the functional generator that was replaced with HP 8101A pulse generator, which is able to generate higher frequencies than the one used before. In order to make the shape of the modulation signal closer to a sine-wave form the trapezoidal waveform was chosen. Table 4.7 lists the settings applied to APD and LED during measurements.

Table 4.7: APD and LED settings at 100MHz

APD modulation voltage settings:	
Parameter	Value
Frequency	100MHz
Offset	-8.25V
Amplitude p-p	3V
Waveform	trapezoidal
LED modulation settings:	
Parameter	Value
LED type	UV 400nm
Frequency	100MHz
Offset	3V
Amplitude p-p	6V

Since the generator cannot cover the whole period range of phase shift between signals at 100MHz modulation frequency, a part of the period that includes two extremums has been found. The output dependence

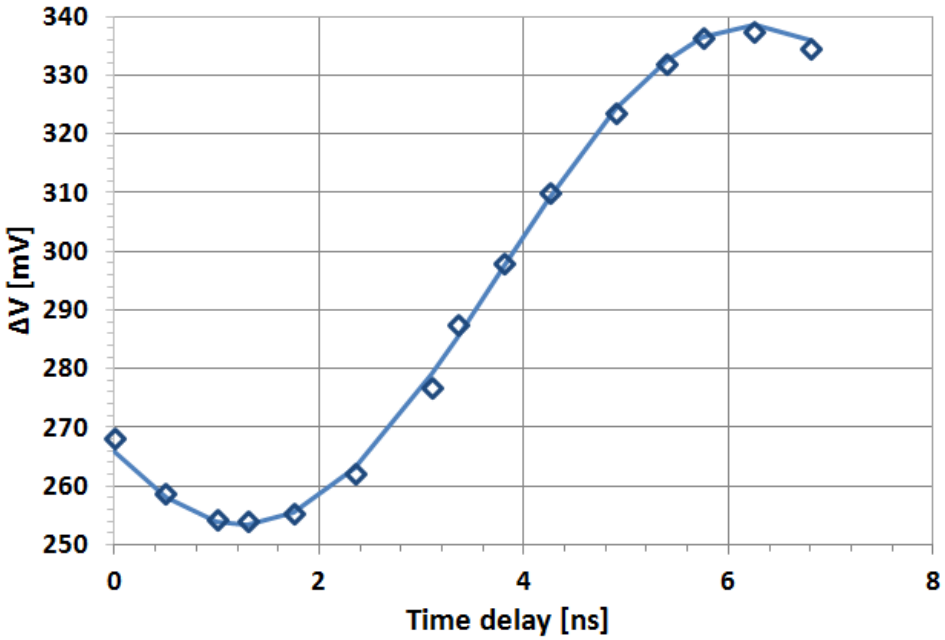

Figure 4.17: Phase sensitive pixel measurement of output dependence on time delay at 100MHz

on the phase shift is depicted in Figure 4.17 showing the same sine-wave behaviour. The maximum demodulation contrast was registered at 8.45V and is equal to 23.6%, whereas maximum SNR is registered at 8.3V and after that decreases.

Figure 4.18a,b shows demodulation contrast and SNR for three different modulation frequencies: 20MHz, 50MHz and 100MHz. As can be seen from the graphs with increase in modulation frequency demodulation contrast becomes higher, as well as SNR improves with a higher frequency.

It was not possible to perform further measurements at even higher frequencies due to the equipment limitations. However, experimental results obtained so far show the feasibility of APD implementation in a phase-sensitive pixel.

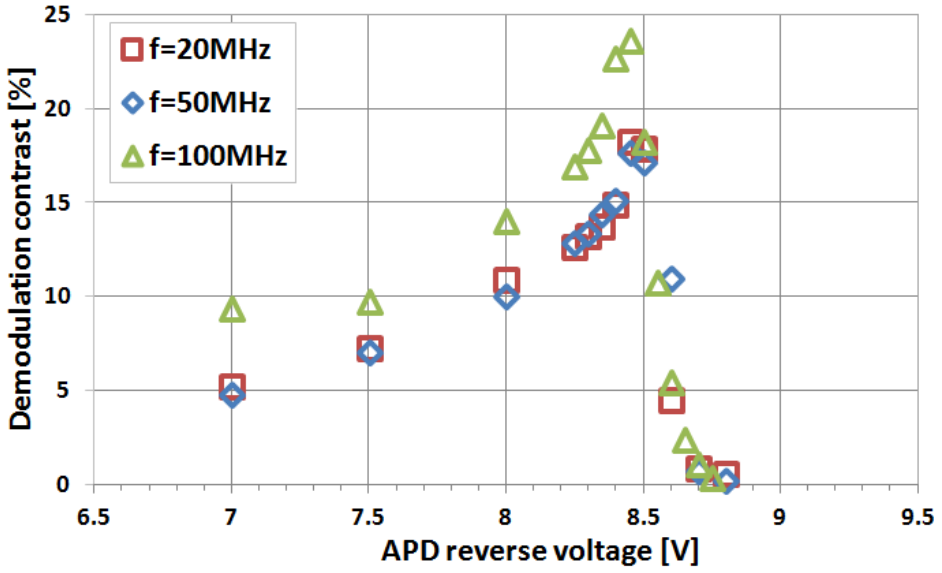

a

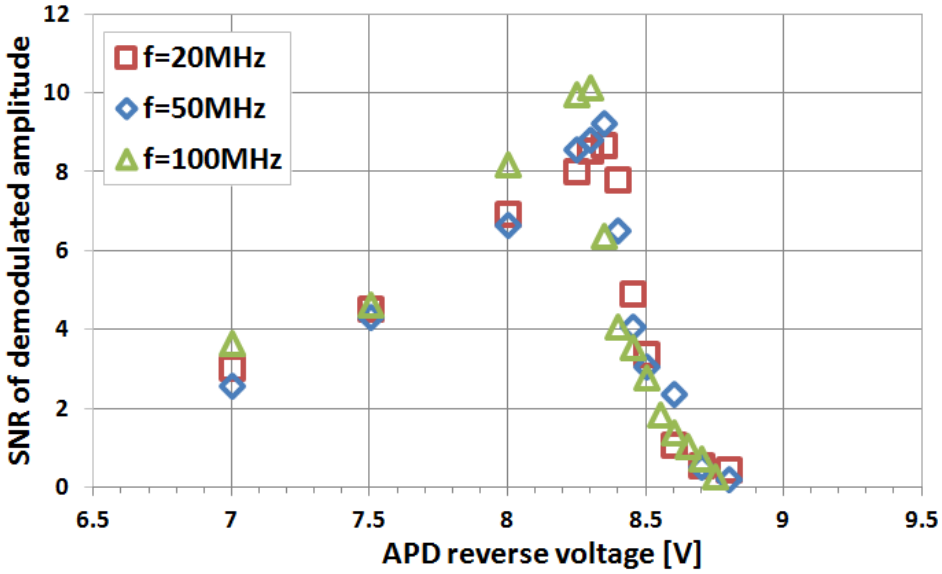

b

Figure 4.18: Phase sensitive pixel measurement at 100MHz: a - demodulation contrast as a function of applied DC bias voltage of APD; b - SNR of demodulated amplitude as a function of applied DC bias voltage of APD

4.3 Conclusion

In this chapter the implementation of a CMOS avalanche photodiode combining detection and demodulation in a single device was presented. After introducing the pixel concept, the design of the avalanche photodiode phase-sensitive pixel was described. In spite of low demodulation contrast, reported by these measurements, the obtained experimental results on the pixel structure have shown the feasibility of the proposed device for the phase detection task and open the way to a perspective implementation of a phase-sensitive pixel array based on this principle. This array could find application in Time-of-Flight 3D imaging, as well as fluorescence lifetime detection in the biomedical field. However, for further implementation different in-pixel amplifier scheme should be taken into consideration, in order to make it more suitable for the application of APD modulation signal.

Chapter 5

APD Image Sensor

In this chapter we will present a novel image sensor based on APDs for TOF ranging. In particular, pixel design and simulation will be described as well as sensor overall architecture. Furthermore, experimental results obtained on the fabricated sensor will be presented and discussed.

Sensor design and simulations were performed using Virtuoso schematic and layout editor of Cadence circuit simulation program [93]. Even though there exists a great variety of CMOS technologies, the AMS single poly four metal $0.35\mu m$ standard CMOS technology was chosen for this sensor implementation. The reason for this lies in the use of the same technology for the APD structure verification that demonstrated good gain uniformity and low noise performance, which increases the chance of successful realization of the sensor. Moreover, low fabrication cost in that technology is a strong advantage making it suitable for proof of concept purpose.

5.1 APD pixel

As was discussed in Chapter 4, pixel schematic should be reconsidered in order to improve circuit immunity to APD bias voltage modulation as well as to increase pixel demodulation contrast. For this reason one of the main constrains considered in the design of the in-pixel amplifier was low

bandwidth for high frequency modulation rejection. From the sensor point of view, the pixel specification should also comply with such parameters as low power consumption, high output range and high circuit compactness.

5.1.1 Pixel design

The main element of the pixel is a low-noise avalanche photodiode that has demonstrated sufficiently good performance for array implementation in Chapter 3. A p+/n-well junction forms the active area of the APD. The early breakdown at the edges of the junction has been avoided by means of a guard ring realized by merging two separate n-well regions made at a close distance from each other, thus isolating p-well diffusion from a p-type substrate. A cross section of the APD structure has been presented in Figure 4.2 of Chapter 4. Although the technology is not optimized for its fabrication, the reported APD offers a reasonable noise factor $F<4$ for an avalanche gain $M=10$ [71].

In contrast to the test pixel described in Chapter 4, the APD connection in the new pixel is reversed in order to achieve better demodulation contrast by avoiding the integration of photocurrent generated at the lower n-well/p-substrate junction. The anode of the APD is now connected to a charge sensitive amplifier (CSA), while the cathode can be modulated synchronously with the incident light signal.

To accomplish compactness and low power consumption requirements, a single-stage five-transistor differential amplifier is proposed as the in-pixel amplifier. This amplifier has a standard pMOS input configuration in order to achieve wide output swing [96]. The differential amplifier schematic is illustrated in Figure 5.1.

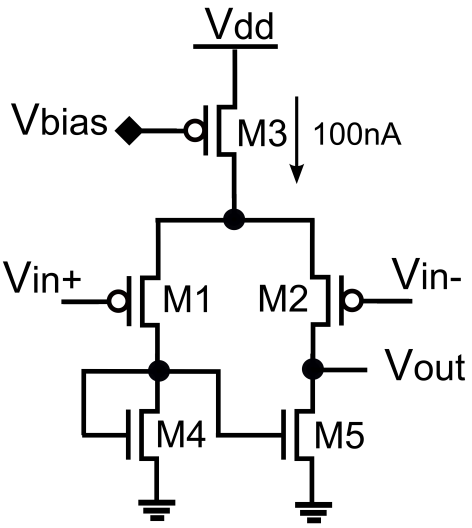

Figure 5.1: In-pixel differential amplifier

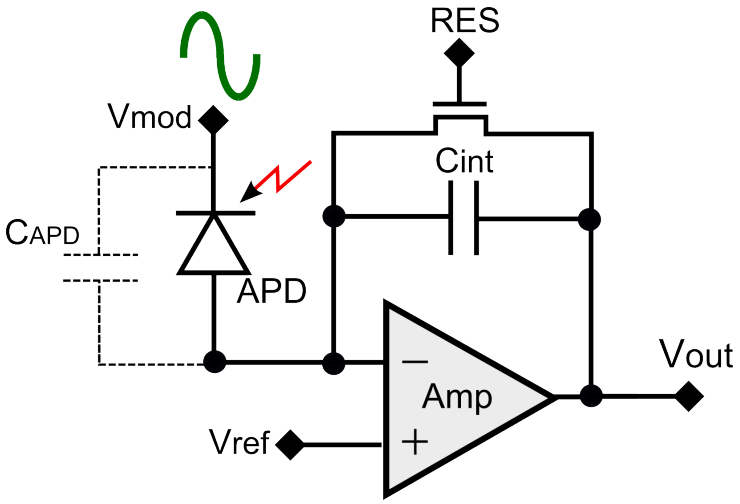

Figure 5.2: Pixel schematic

The CSA is realized with the differential amplifier, a feedback integration capacitor of 10fF, and a reset transistor. The pixel schematic diagram is reported in Figure 5.2. The main characteristics of the differential amplifier are listed in Table 5.1.

Table 5.1: In-pixel Amplifier Characteristics

Parameter	Value
Gain	47dB
GBWP	12MHz
f-3dB	50kHz
N transistors	6
Power consumption	330nW
Integration capasitance	10fF

5.1.2 Pixel simulation

Design and simulation was performed in the Cadence circuit simulation program, where the model of APD was implemented. The Current-Voltage characteristic, model equations and APD schematic are shown in Figure 5.3. The model equations were adopted from [64]. The breakdown voltage of this APD is 11.2 V. The capacitance of the avalanche photodiode is calculated with equation (5.1) and is equal $132fF$ for the chosen technology and APD size of $33\mu m \times 20\mu m$. In the equation A and P are the area and perimeter of the p/n-well diode, respectively, V is the reverse bias voltage. The remaining parameters in equation (5.1) were obtained from the process documentation for $0.35\mu m$ CMOS technology. Since the APD is realized in an n-well, an n-well/p-substrate diode with a capacitance of $63fF$ is also included in the model. APD photocurrent was modelled with a parallel current generator, controlled by an additional input, named *iph* (Figure 5.3c).

$$Cpn = \frac{A \cdot CJ}{(1 + V/PB)^{MJ}} + \frac{P \cdot CJSW}{(1 + V/PB)^{MJSW}} \tag{5.1}$$

The operation principle of the proposed pixel, using APD gain modulation to perform phase-sensitive detection of a modulated light signal was explained in Chapter 3 and 4. The APD is reverse biased with a DC voltage close to breakdown and a superimposed modulation voltage synchronous

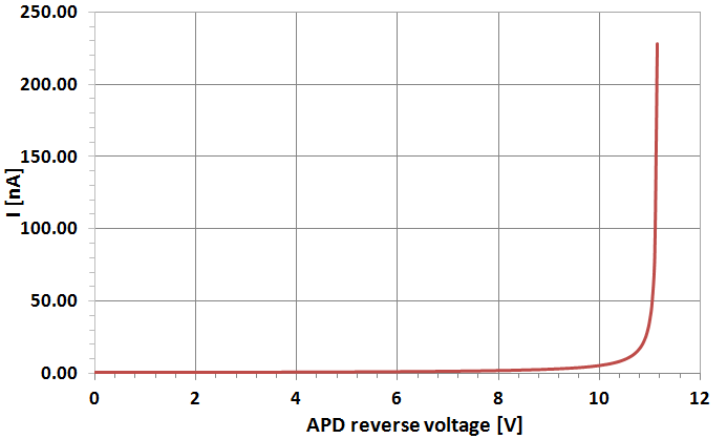

a

```
modul APD(vp, vn, iph);
inout vp, vn, iph;
electrical vp, vn, iph;
parameter real is = 1e-12 from (0:inf);
      real vacross, idark, M;
      analog begin
            vacross = V(vp, vn);
            idark = 1e-14 * pow(1/(1-pow(-vacross/11.18, 0.75)), 2.2);
            M = 1/(1-pow(-vacross/11.18, 1.7));
            I(vp, vn) <+ idark * (linexp(vacross/$vt) - 1) - M*V(iph);
      end
endmodule
```

b

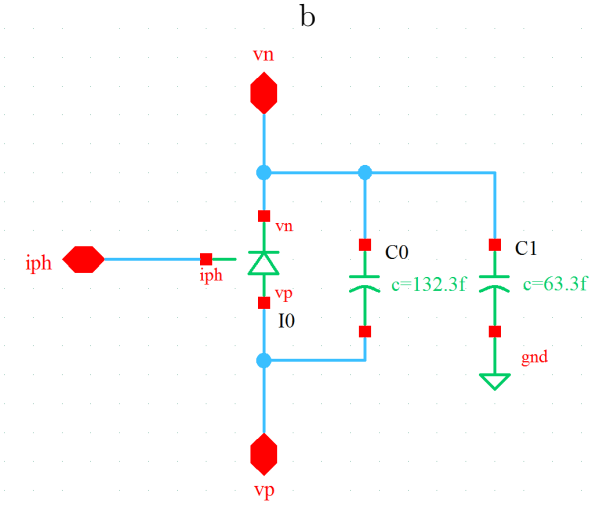

c

Figure 5.3: APD simulation model: a - current-voltage characteristic, b - implemented verilog model, c - APD schematic

with the incident light. Due to the modulation of the bias voltage, APD internal gain M is also affected by the modulation. In this condition, the detector integrated current is proportional to the correlation function $c(\tau)$ between the received modulated light signal $Popt(t)$ and internal gain $M(t)$ (equation (4.3)). The correlation current signal generated at the anode of the APD is integrated on a feedback capacitance $Cint$ of the charge sensitive amplifier, which is equal to 10fF. The output voltage of the CSA is proportional to the average current flowing through the APD during its illumination. Thus, the output voltage contains phase and intensity information required for a range image reconstruction.

A number of simulations has been performed to find optimal settings and device parameters. The most important simulation is one that evaluate pixel capability to work as an electro-optical demodulator, which shows pixel output dependence on a phase-shift between modulated optical and APD bias voltage signals. These simulations were performed with modulated signals applied to the cathode and iph inputs of the APD. The signal, which represents light intensity, has the amplitude value of 100pA and the DC offset of 100pA with the frequency equal to 20MHz. The modulated signal applied to the cathode of the APD has the amplitude value of 2.8V, the DC level of 11.2V and the same modulation frequency equal to 20MHz as for the light modulation signal. The phase of the signal is changed only for one input, in this case it is the iph input. For this simulation the phase was changed from 0 to 360 degrees with linear steps of 10 degrees. The transient analysis of the amplifier output is shown in Figure 5.4a. Figure 5.4b represents the dependence of the output voltage difference at the beginning and at $52\mu s$ integration time on the phase delay. The total integration time in the simulation is $45\mu s$. Simulation results verify the operation of the APD pixel as electro-optical demodulator. However, the demodulation contrast of this simulation reaches only 8%.

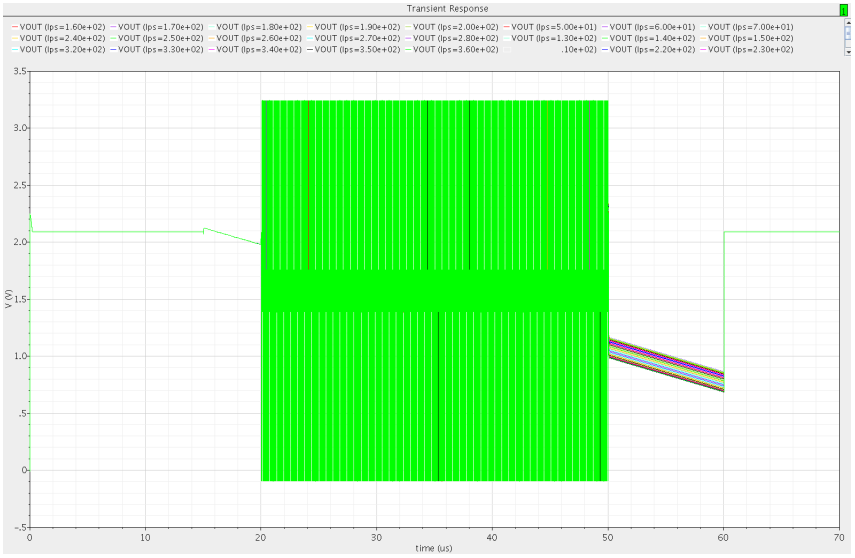

a

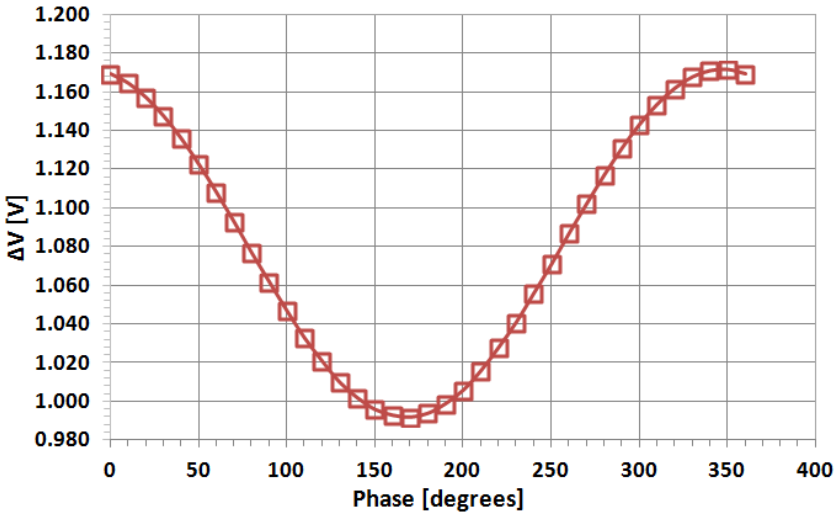

b

Figure 5.4: APD pixel simulation: a - transient simulation, b - output dependence on the phase shift

The reason for this was found at the input node of the CSA that was following the modulation voltage of the APD. This resulted in only 1V effective modulation amplitude of the APD. Hence, it was necessary to stabilize the input node of the in-pixel differential amplifier with the presence of modulation. For this purpose additional input capacitance was inserted at a pixel level. The simulation performed with the stabilisation capacitance at the amplifier input node has increased the effective modulation amplitude of the APD to 3V. This pixel has shown the demodulation contrast of 31% at 20MHz modulation frequency with the same settings described above. With additional adjustments of APD modulation amplitude and bias voltage the demodulation contrast higher than 50% was reached during simulations.

Since the in-pixel differential amplifier was designed to have low power consumption and to serve the purpose of a low pass filter to cut-off high frequency modulation it is not able to drive high capacitive load at a column level. Hence, a standard source follower buffer is required at a pixel level. A standard switch transistor is necessary in each pixel as well. The final schematic of the pixel is shown in Figure 5.5.

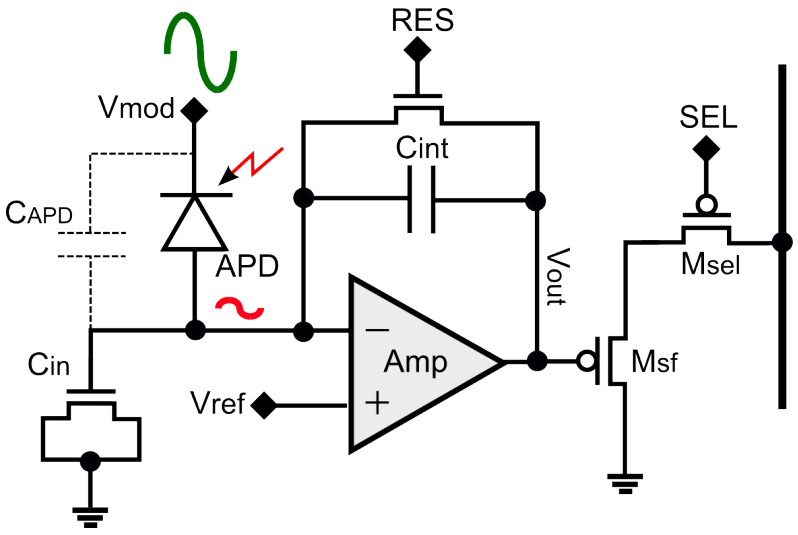

Figure 5.5: Final pixel schematic

5.1.3 Pixel layout

The APD has a rectangular shape with facet corners to avoid high electric field concentration at the corners of the structure. The size of the rectangular APD is $32.1 \times 18.7\mu m^2$ including a guard-ring structure and n-well contacts. The active area is $23.4 \times 10\mu m^2$. Sharing the n-well of all the APDs in a row allowed to obtain a $30\mu m$ pitch in the horizontal dimension.

Since the pixel should have a square shape the area allocated for in-pixel electronics is $30\mu m \times 11.3\mu m$ that is further reduced in vertical dimension due to the spacing restrictions applied to high voltage APD regions. This area is shared between five pMOS transistors, four nMOS transistors and one poly-poly capacitance. The input node stabilization capacitance is realized as a MOS-capacitance on an nMOS transistor. The total pixel size is $30 \times 30\mu m^2$ with 25.75% fill-factor. Table 5.2 summarizes the main pixel characteristics, while the layout of the pixel is sketched in Figure 5.6.

Table 5.2: Pixel Summary

Technology	$0.35\mu m$ standard CMOS 1P4M
Pixel pitch	$30\mu m$
Transistors per pixel	9
Fill-factor	25.75%
Photodetector type	CMOS Avalanche Photodiode (APD)
Pixel supply voltage	3.3V

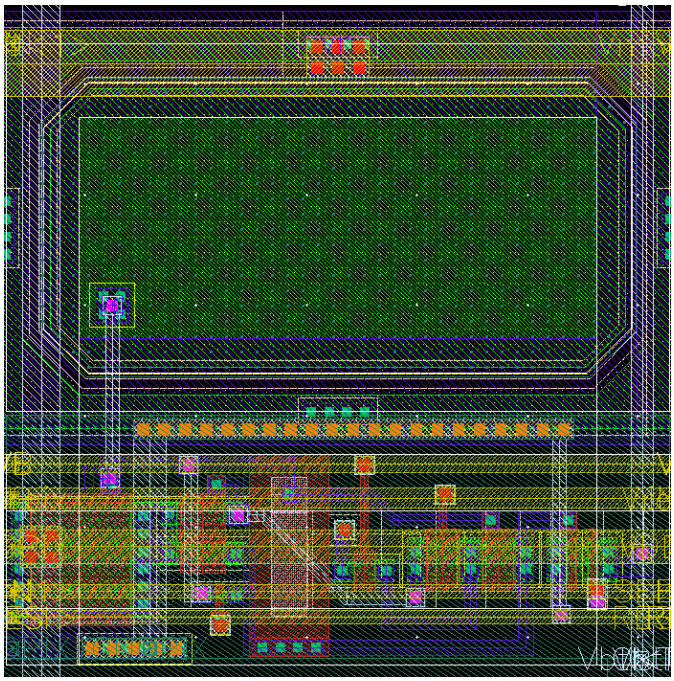

Figure 5.6: Pixel layout

5.2 APD sensor design

Regarding the rest of the sensor architecture, there are no major constrains, thus a standard sensor readout scheme can be employed.

The sensor architecture consists of a 64 x 64 pixel array as a core of the chip, row and column decoders, column amplifiers and an output buffer. Figure 5.7 shows the overall image sensor architecture. Both column amplifiers and output amplifier are based on a standard switch-capacitor scheme performing Double Delta Sampling operation to reduce the effect of Fixed Pattern Noise at pixel and column levels.

Two different readout modes were implemented. The first one was designed to perform a column DDS operation in order to remove FPN and partially kTC noise. The sensor is exposed to the light for the integration time $Tint$, and then the readout procedure starts. The timing of this first mode is depicted in Figure 5.8. Following the time specifications, a sin-

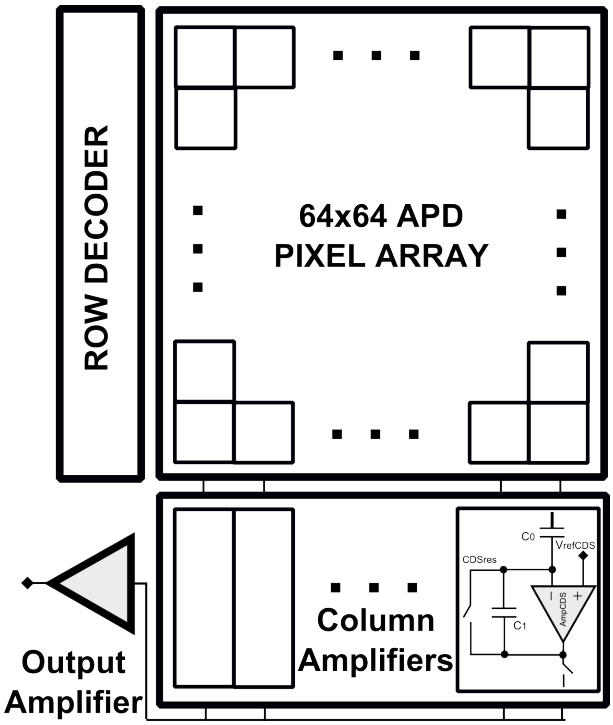

Figure 5.7: Sensor schematic

gle row should be readout in about 8μs, thus the whole array is readout in 512μs. Maximum data rate has been estimated around 10Msamples/s. Considering also the time spent for column DDS operation, the average data rate is 8Msamples/s.

The second readout scheme allows sensor to measure the absolute value of the pixel output without performing in this case a DDS operation at a column level. The timing diagram for the second mode is illustrated in Figure 5.9. The idea in this case is to acquire two images: one immediately after the pixel reset and the other after the integration time. Hence, calculation of the difference in these two images with the help of external software removes possible offsets introduced by smearing and kTC noise.

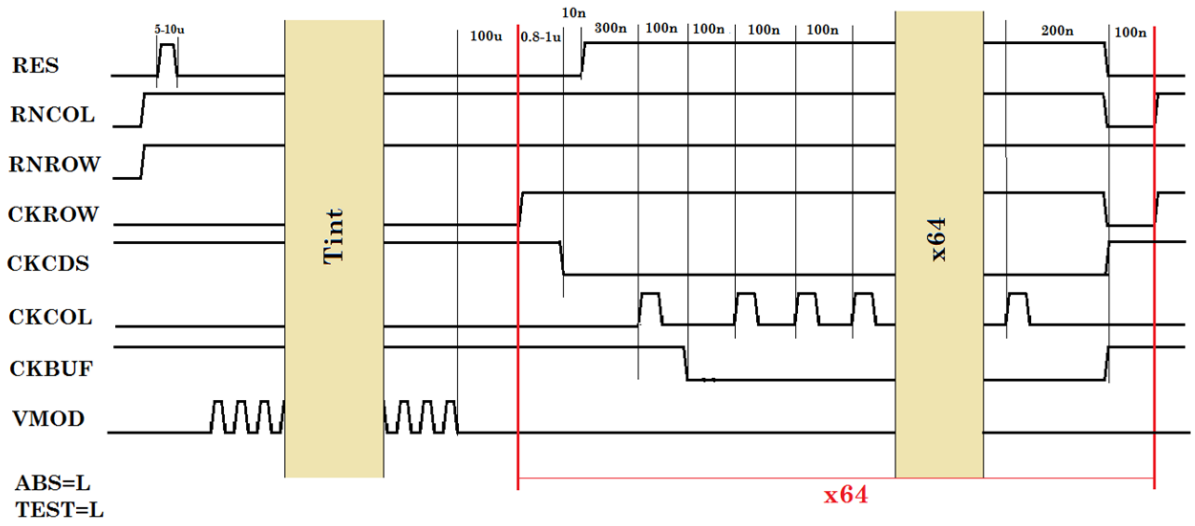

Figure 5.8: First readout mode: timing diagram for normal acquisition

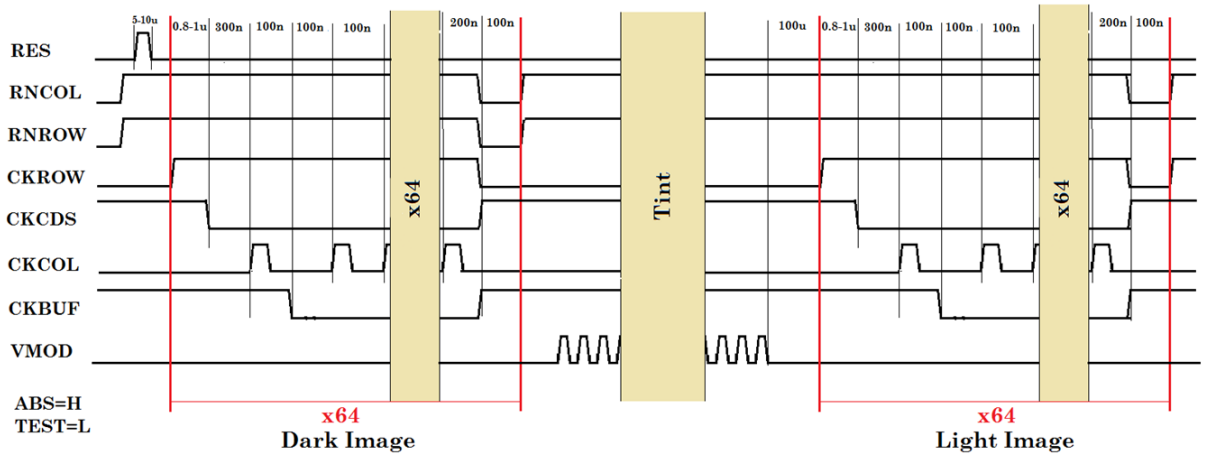

Figure 5.9: Second readout mode: timing diagram for double acquisition

5.3 Experimental results

The APD chip was fabricated in 0.35μm 1P4M standard CMOS technology. The sensor micrograph is shown in Figure 5.10, where the main functional blocks are highlighted. The 64 $\times$ 64 pixel array, the column amplifiers with column decoders, row decoders and the output buffer are allocated in a 3.1 $\times$ 2.4mm^2 area.

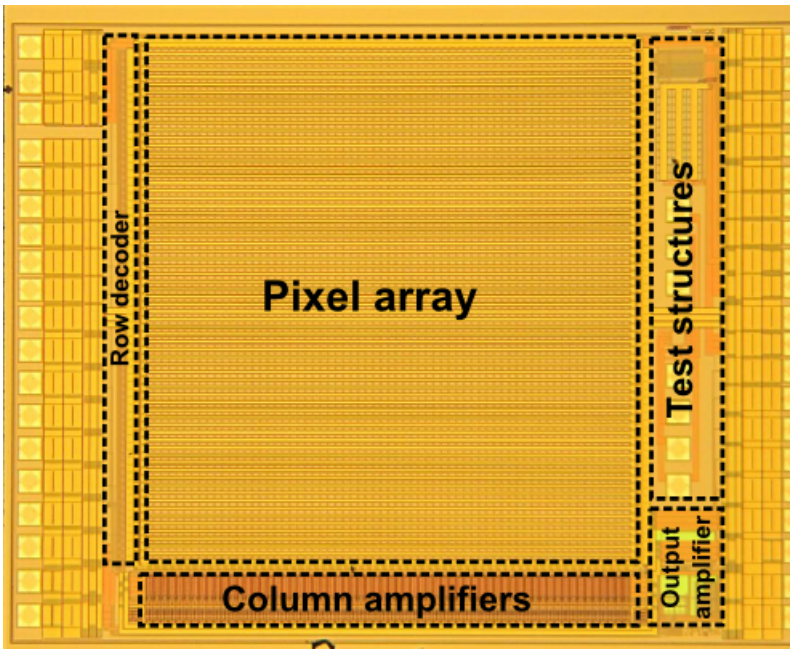

Figure 5.10: Chip micrograph

5.3.1 Setup description

The experimental setup used to measure the sensor performance is similar to one shown in Figure 4.13 of Chapter 4, except now measured data are processed on a computer with the help of a Labview software program [97]. In addition, control signals and modulation signals are generated by a digital board controlled by the same Labview program.

From the hardware point of view, the most delicate part of the setup is the generation and distribution of the modulation signals in the test board. The adopted circuit should have the possibility to be driven by an external instrument or by a pattern generator in order to implement the sensor control directly in digital form. The modulation voltage should be superimposed on the APD bias voltage, hence a high-pass filter should be employed. The scheme was estimate to drive 850pF load of the chip. For this purpose the schematic in Figure 5.11 was adopted.

All other voltage and current input references have standard range apart

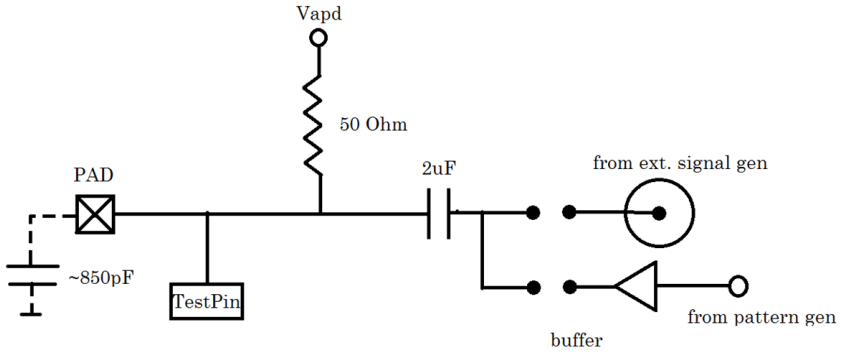

Figure 5.11: The scheme for the modulation circuit

from the voltage dedicated to the APD (11.5V typically), which can be generated by an external power supply or, in perspective, by an integrated DC/DC converter plus linear voltage regulator (Figure 5.12). The linear voltage regulator is required to suppress the ripples present after the DC/DC converter that degrades the performance of the device. Moreover, it offers more precise adjustment of APD bias voltage. The data conversion was performed by a 12-bit ADC of the acquisition board at 10Msamples/s.

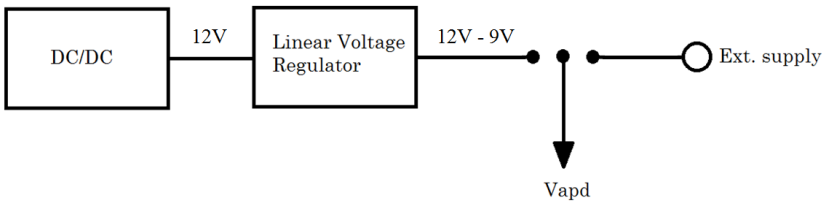

Figure 5.12: The scheme for the DC bias voltage

5.3.2 General sensor characterization

Measurements with constant light

The performance of the sensor as a 2D imager was characterized, showing a Fixed Pattern Noise in the dark lower than 0.5% and a dynamic range of 50.5dB at the avalanche gain M=10. The noise floor depends on the applied bias voltage, reaching a minimum of 26 electrons for a multiplication gain $M = 15$.

In order to evaluate sensor output signal and noise as a function of APD bias voltage, measurements were performed in the dark and with the presence of light. An ultraviolet LED with 400nm wavelength was used as a light source. Avalanche photodiode bias voltage was reversed and increased from 2.1 to 12.9V. The signal from the sensor was acquired through the National Instrument acquisition board and processed in the Labview program.

Figure 5.13 shows output signal, derived form the difference between light and dark signals, and pixel noise as a function of APD bias voltage.

Signal to Noise Ratio as a function of APD bias voltage is presented in

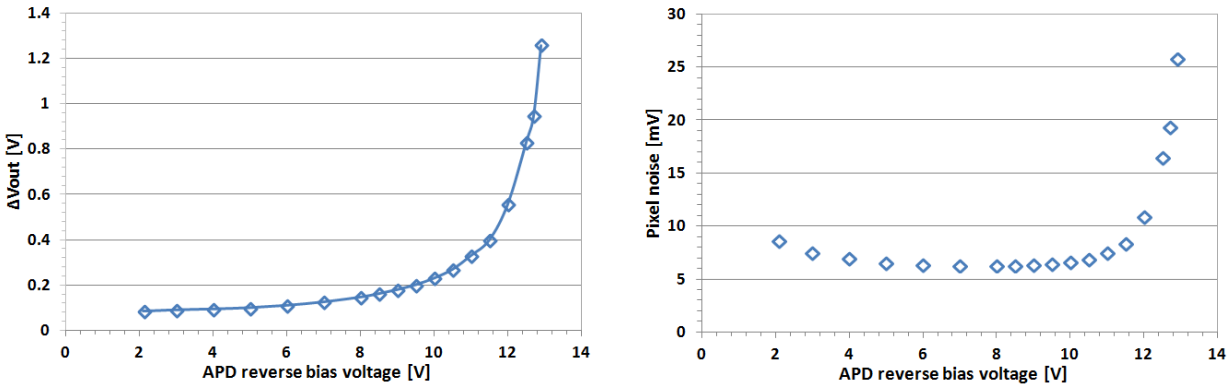

a b

Figure 5.13: Sensor measurement with ultraviolet LED: a - output signal as a function of APD bias voltage, b - pixel noise as a function of APD bias voltage

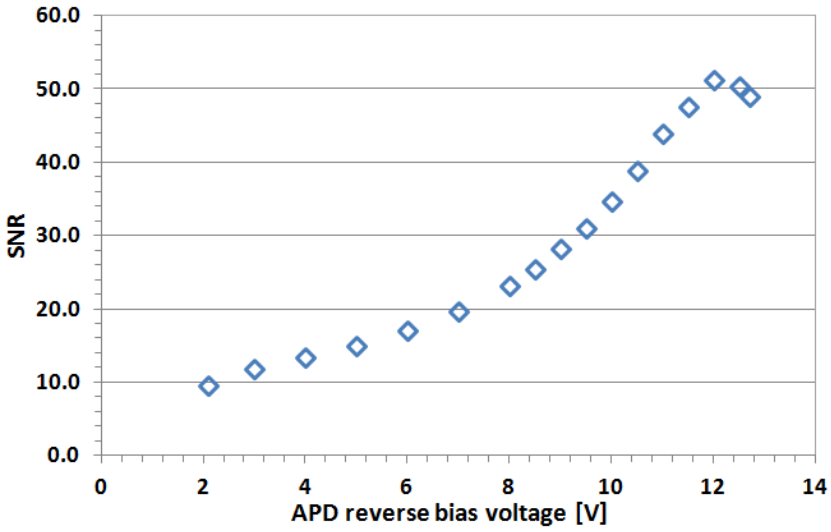

Figure 5.14: Phase sensitive pixel measurement of SNR in light and dark conditions

Figure 5.14. SNR experiences its maximum at 12V, where the multiplication factor M is equal to 6.

The dark current distribution among the pixels in the sensor was measured for different applied APD bias voltages. The dark current was derived from several measurements with different integration times, where noisy pixels were filtered. The maximum integration time is equal to 56ms. The cumulative distribution and histograms for several chosen voltages is illustrated in Figure 5.15. The measurement was performed at room temperature. The distribution of dark current in the sensor is similar in shape to Dark Count Rate distribution of SPAD arrays [98], histogram shows that most of the pixels have similar value of dark current, but part of the pixels have larger dark current values, represented as a long tail in the histogram. The number of pixels with higher dark current increases with applied bias voltage. In general pixels with higher dark current exist even in low biased photodiodes, as demonstrated at 5V biasing in the Figure 5.15a. The high dark current in the bad pixels is related to the presence of localized defects in the APDs. These defects are randomly distributed in

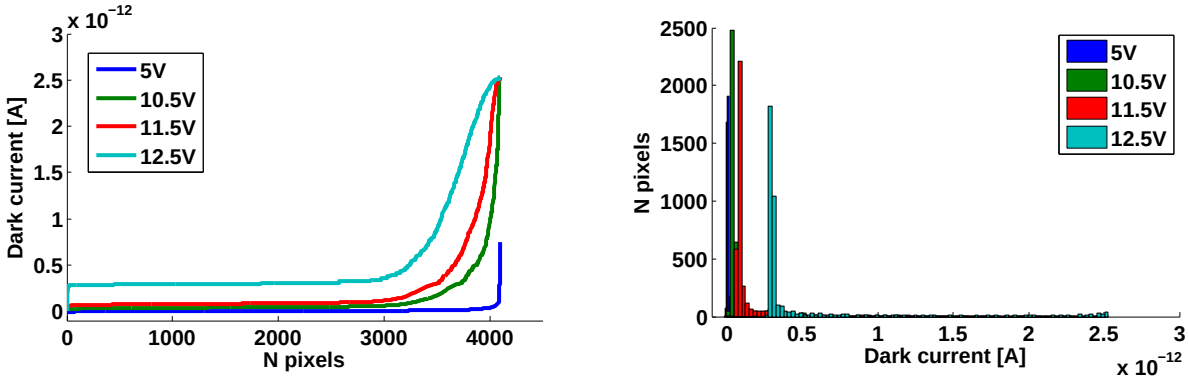

a b

Figure 5.15: Dark current distribution

the array. Some preliminary work performed on large APDs indicates that dark current is dominated by trap-assisted tunnelling, which is dominant at high electric fields in the presence of defects [76]. The most frequent value of dark current for different applied voltages is plotted in Figure 5.16. The dark current at 11.5V biasing is equal to 87fA.

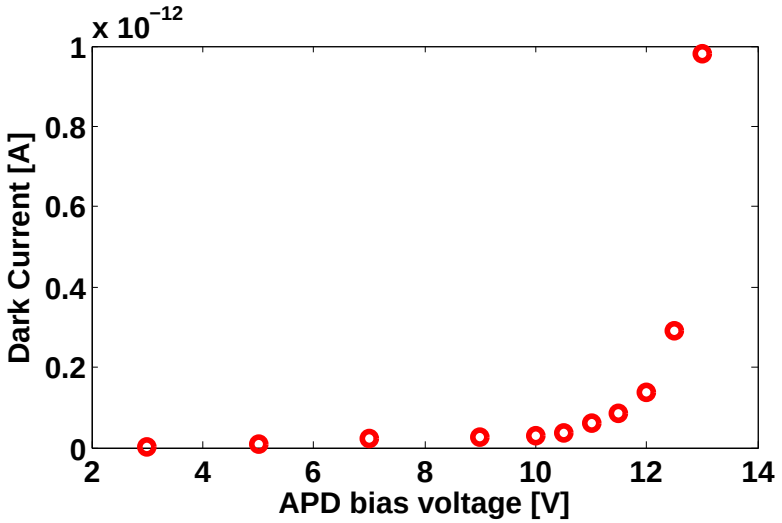

Figure 5.16: Dark current dependence on APD bias voltage

Next, the Photon Responce Non Uniformity (PRNU) of the sensor was measured. For this measurement the light source was changed to a red laser working at 650nm. Figure 5.17 shows the PRNU or spatial noise as a function of APD bias voltage and as a function of APD gain.

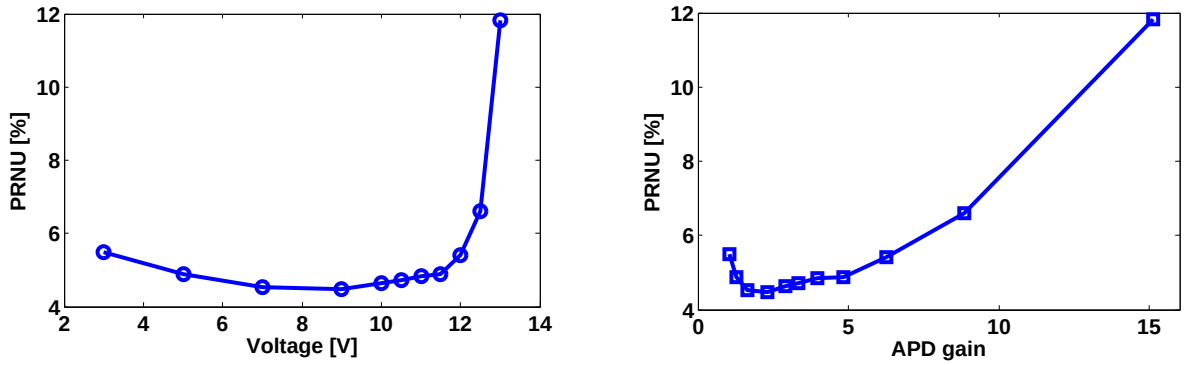

a b

Figure 5.17: PRNU measurement

Measurements with modulated light

A set of measurements was performed on a 64 × 64 pixel array with 200 3Dfps, corresponding to 800 2Dfps. A plain white target was placed at 1m distance from the sensor, the setup is depicted in Figure 5.20. The demodulation contrast and SNR of the demodulated signal estimated at different APD bias voltages at 25MHz modulation frequency are reported in Figure 5.18.

By increasing the average bias voltage, thus increasing the APD internal gain, an increase in the demodulation contrast is observed. Although a very high demodulation contrast exceeding 80% can be obtained, the SNR reaches its maximum at an intermediate value of bias voltage. As the bias approaches the APD breakdown voltage, the increase in the APD excess noise factor F, causes a loss of SNR. The maximum SNR is therefore determined by a tradeoff between demodulation contrast and noise factor.

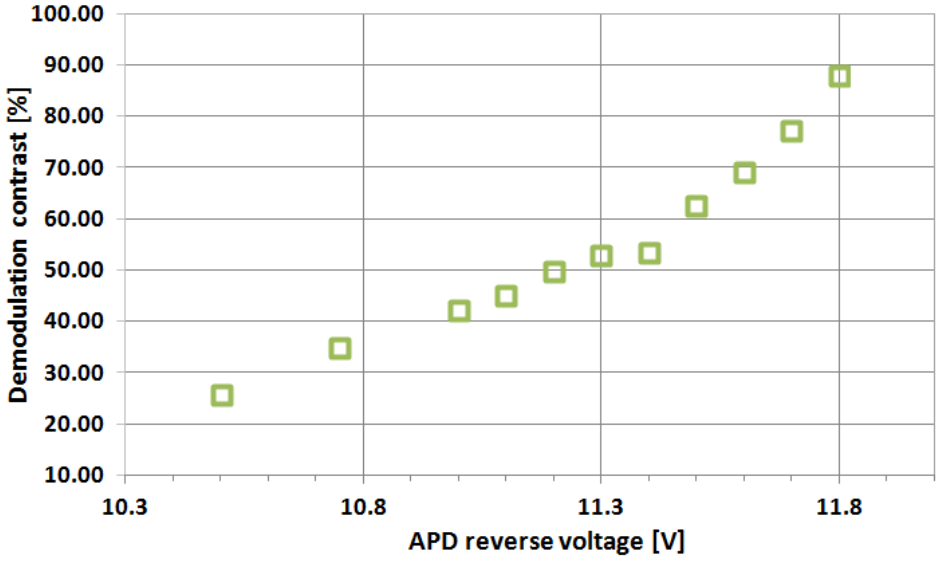

a

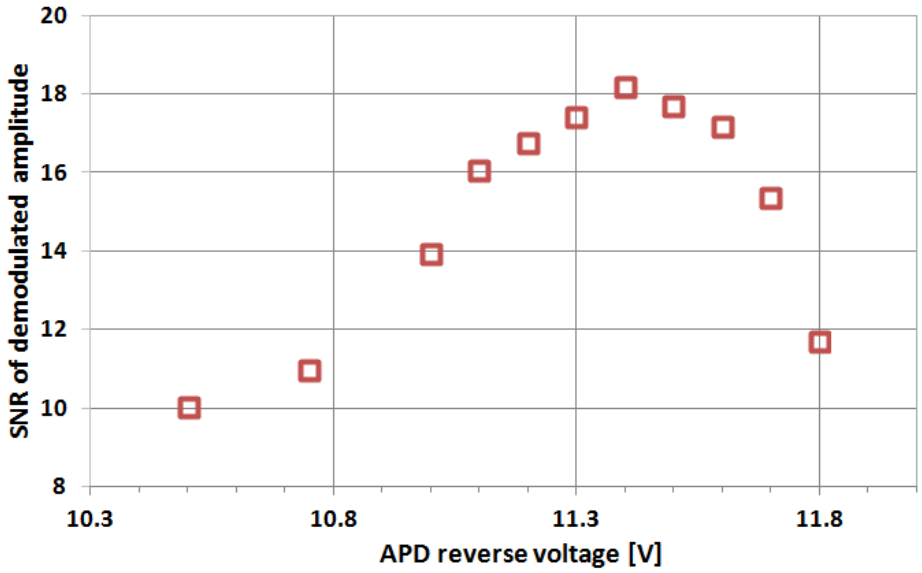

b

Figure 5.18: Sensor measurement at 25MHz: a - demodulation contrast as a function of applied DC bias voltage of APD; b - SNR of demodulated amplitude as a function of applied DC bias voltage of APD

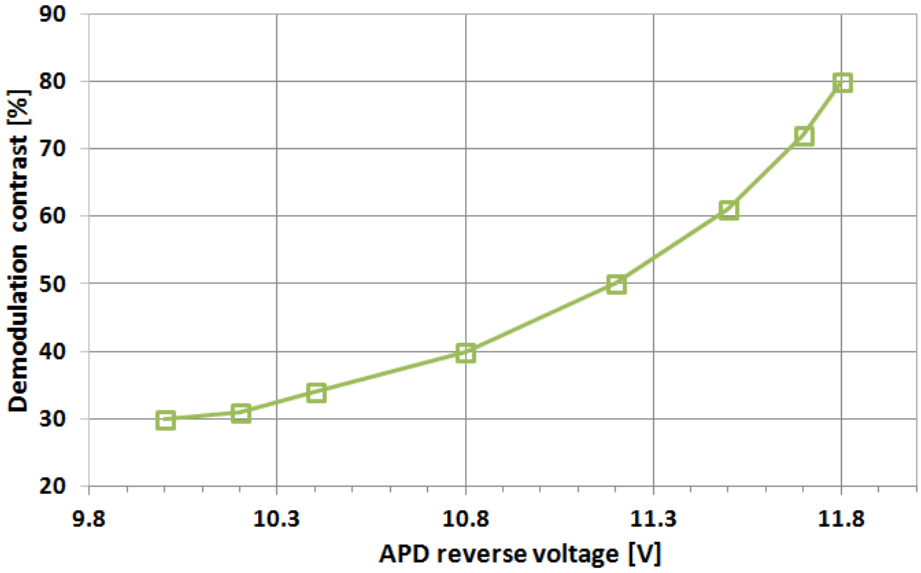

Figure 5.19: Demodulation contrast of single pixels at 200MHz modulation frequency

A characterization of single test pixels also contained in the chip was carried out to assess the maximum demodulation frequency for the APD. Demodulation contrast as high as 80% at 200 MHz modulation frequency was measured with a modulated laser source of 650nm. Figure 5.19 illustrates demodulation contrast as a function of APD bias voltage at 200MHz modulation frequency. This maximum frequency was limited by the available measurement setup where modulation signals were generated by an Anritsu digital data analyzer MP1632C. The rest of the setup is similar to the one in Figure 4.13 from Chapter 4.

In the successive measurements, the APD bias voltage of 11.5V was chosen as the optimal compromise in terms of good demodulation contrast (exceeding 60%) and high SNR. Tables 5.3 and 5.4 summarizes pixel and sensor performance, respectively.

Table 5.3: Pixel Characteristics

Process Technology	CMOS 1P4M 0.35μm
Pixel pitch	30μm
Fill factor	25.75%
Sensitivity	0.72xM V/spW @ 850nm
Dynamic Range	50.5dB @ M=10
Pixel noise	26 el. @ M=15
Demodulation contrast	80% @ 200MHz and 650nm

Table 5.4: Sensor Characteristics

Array size	64 x 64
Chip size	3.1mm x 2.4mm
Max frame rate	800fps for 2D 200fps for 3D
Supply voltage	3.3V
Chip current consumption	$<$ 15mA
FPN	$<$ 0.5%

5.3.3 Distance measurement

A 3D camera system was built using an illumination unit made of two high-power Infra-Red arrays with 850nm wavelength. The characterization of both the sensor and the complete range camera system were performed at 25MHz modulation frequency, the maximum allowed for the light source and available equipment. The non-ambiguity range D_{max} at 25MHz modulation frequency f_m is equal to 6m according to the expression (5.2). A DC bias voltage close to the breakdown with 2V peak-to-peak modulation signal was applied to the APD cathode.

$$D_{max} = \frac{c}{2 \cdot f_m} \tag{5.2}$$

The setup for this measurement is different from the one described before. The schematic setup and system photograph are illustrated in Figure 5.20a,b. In this case a plane white target is illuminated by the illumination

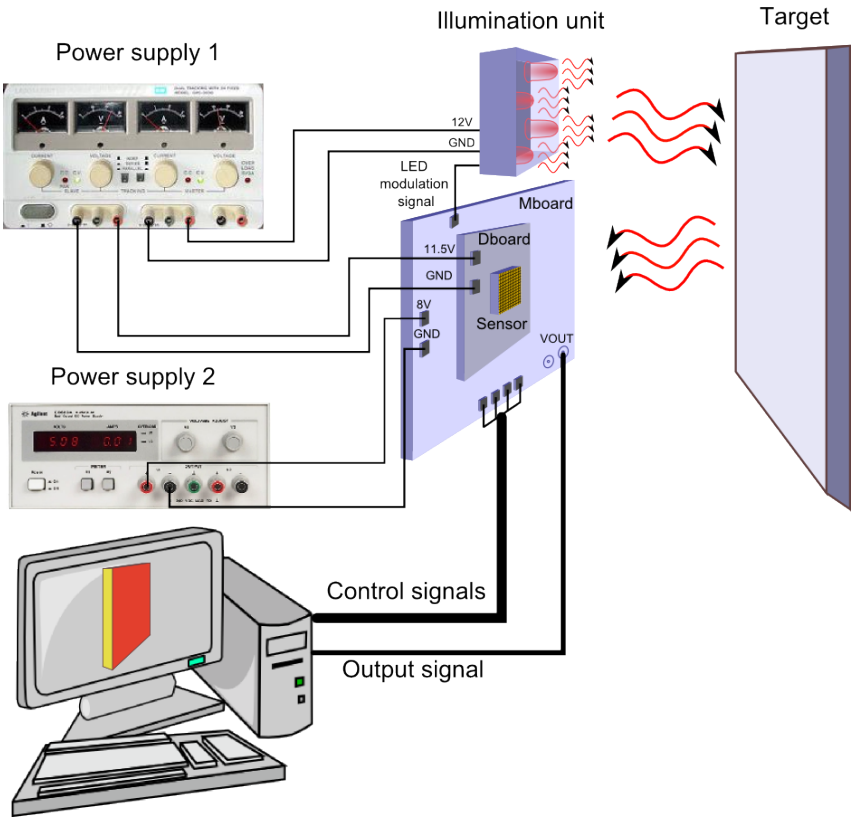

a

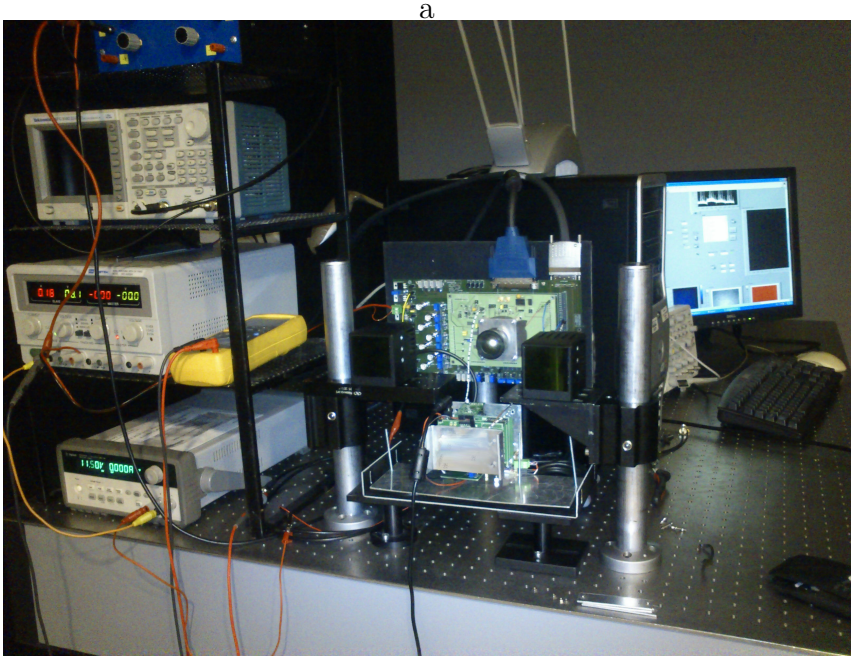

b

Figure 5.20: a - measurement setup, b - setup photograph

source of the 3D camera system and placed at different distances from the camera system.

Four sequential frames made with four $\pi/2$ phase shift steps between APD cathode and light modulation signal are acquired to form a 3D image, externally computed and reconstructed from a phase delay and intensity information in each pixel, as was described in Chapter 3. The distance measurement performance of the sensor was verified using two different 3D frame rates of 200fps and 50fps covering the range from 0.5m to 2m and from 2m to 4.75m, with 25MHz modulation frequency (Figure 5.21).

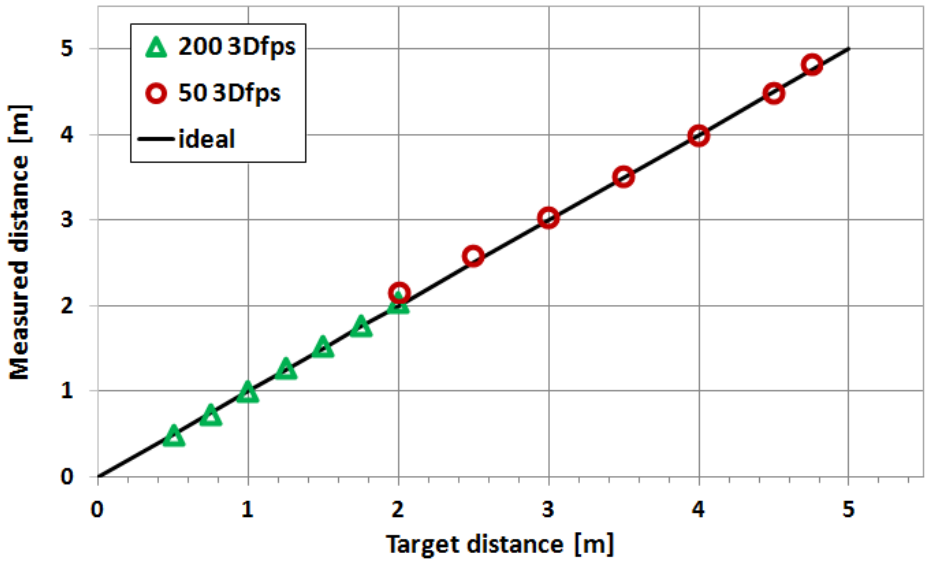

Figure 5.21: Distance measurement as a function of the distance to a plain white target

Figure 5.22 reports the measured distance precision as a function of target distance considering a Region of Interest of 32×32 pixels. The best precision of 1.9cm before sensor saturation, a distance non-uniformity of 1.1cm and distance nonlinearity lower than 1.7% at 50fps were obtained.

Two examples of range images are shown in Figure 5.23, where a 2D image representing the demodulated signal amplitude is shown together with a color-coded distance image and the corresponding image histogram.

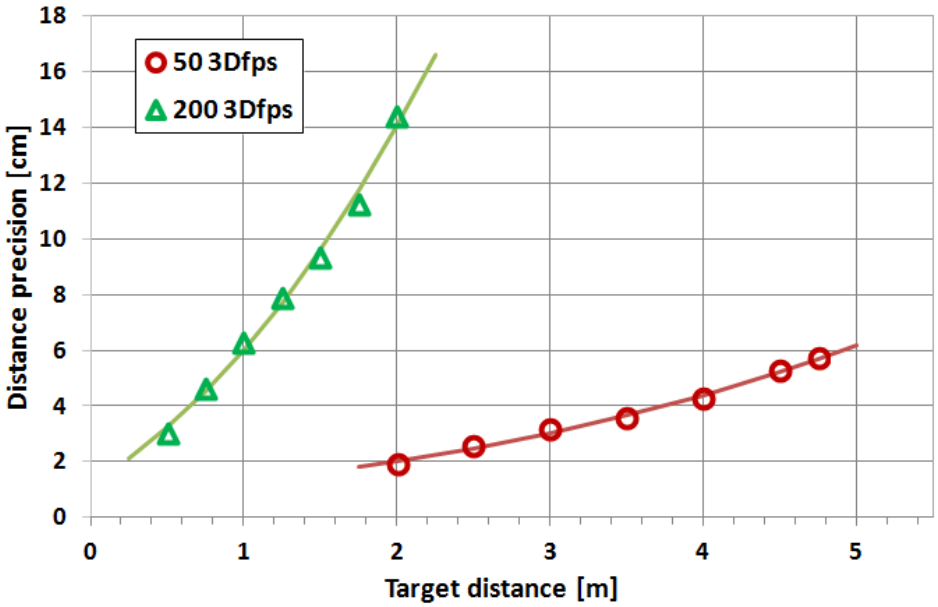

Figure 5.22: Distance precision as a function of the distance to a plain white target

The top image, where targets are located between 1 and 5m, corresponds to a single-shot frame from a video sequence acquired at 50 3Dfps. The bottom image illustrates a scene at a 3D frame rate of 200fps with the distance range from 0.5m to 1.1m averaged over 100 frames in order to reduce the effect of temporal noise.

The characteristics of the sensor and the camera system are summarized in Table 5.5.

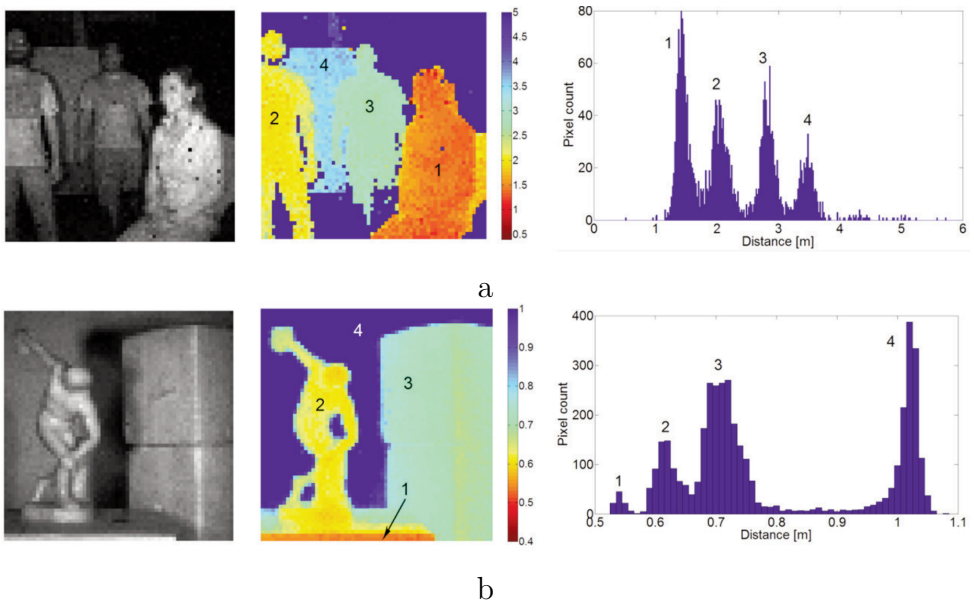

Figure 5.23: 2D, 3D images and image histograms: a - range image acquired at 50fps, b - range image acquired at 200fps averaging over 100 cycles

Table 5.5: Camera System Characteristics

Modulation frequency	25MHz	
Peak modulation current	260mA	
Illuminator type	2x4 - LED array 850nm	
Illuminator field of view	± 15deg FWHM	
Peak optical power	21 W/m^2 @ 1m	
Objective	f=6mm,F#=1.2	
Distance range	2m - 4.75m	@ 50 3Dfps
	0.5m - 2m	@ 200 3Dfps
Precision	1.9cm @ 2m	@ 50 3Dfps
	5.7cm @ 4.75m	@ 50 3Dfps
Distance FPN	1.1cm	@ 50 3Dfps
Distance non-linearity	<1.7%	2m - 4.75m range

Chapter 6

3D Camera Prototype Based on Linear-mode Gain-modulated Avalanche Photodiodes

A 3D camera prototype based on the 64 × 64 image sensor described in the previous chapter has been developed. The main requirements that have been taken into account are prototype size, APD DC biasing and modulation, as well as power supply filtering and USB operation.

Figure 6.1 shows a schematic block diagram of the camera prototype consisting of a prototype PCB with the sensor, an LED illumination unit and an FPGA board. Control signals for the sensor board and LED illumination unit are generated using the Opal Kelly XEM3050 FPGA board [99]. The FPGA board also acquires, processes and transmits received signals to a PC via USB connection. Visualization is provided on a laptop screen. In addition, the computer is utilized to provide FPGA with a firmware and control camera parameters such as integration time, reset time and some others. External power supply provides necessary power to FPGA and illumination units. FPGA board, in turn, provides power to the sensor board.

The FPGA board has dimensions of 75mm × 50mm that defines the size

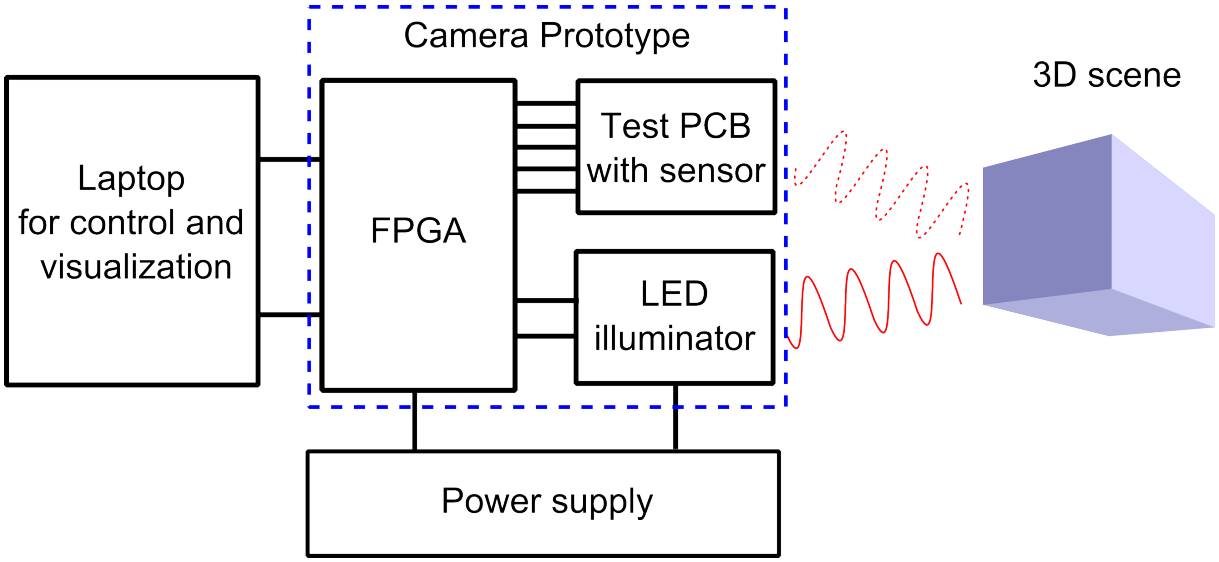

Figure 6.1: 3D camera prototype block diagram

of the prototype. Two boards are to be mounted together in a sandwich-like way, which provides the compactness necessary for the prototype.

The illumination unit consists of two boards hosting two IR LEDs each. Illumination boards are placed on two sides of the objective in order to avoid shadow effects. As a result illumination unit increases the dimensions of the prototype, which becomes 14cm in the length. The LEDs peak optical power is less than 1.8W. In addition, LEDs are covered with diffusers that have $\pm 24°$ FWHM angle.

Regarding the sensor board, following units are included:

- sensor
- APD DC bias voltage
- APD modulation driver
- reference current and voltage sources
- output buffer and Analog-to-Digital Converter unit

A surface mounted package for the sensor is used in order to save space for other units on the board. In general, number of hole-mounted components was kept as small as possible since they have to be mounted on both sides of the board. For this reason the only hole-mounted elements are jumpers and one trimmer for APD DC bias voltage adjustment.

APD DC bias voltage, realized on a charge pump circuit, converts 5V coming from FPGA board to 15V. Next, a linear voltage regulator adjusts APD DC voltage to a lower level controlled by the trimmer. In the camera prototype DC bias voltage level is set to 11.5V.

Regarding the APD modulation voltage, square-wave modulation signal comes from the FPGA board and enters the buffer stage to ensure sufficient power to modulate a high capacitive load of the sensor. The modulation amplitude coming to the sensor is 3V spanning from 0 to 3V.

The chip requires three reference voltages: the in-pixel amplifier reference voltage equal to 2.1V and two column amplifiers and output buffer reference voltages equal to 1.65V. Furthermore, two reference current sources of 10μA are utilized for sensor biasing. Vdd value of 3.3V required for the sensor is provided by the FPGA board directly.

ADC and output buffer are set to sample and digitize the input range from 1.65V to 3.3V. Next the digitized signal is processed by the software running on a PC, where the phase value is calculated from four acquisitions and further the distance is derived for each pixel. The visualization of the distance can be observed on a PC monitor, it is represented by dots or wire-frame in a colour code.

The example of a 3D image captured by the camera prototype and 2D image made by usual camera is shown in Figure 6.2a,b. This image was taken with 3ms integration time averaged by median and low-pass filters. Due to this the equivalent frame rate is 6 3Dfps. The images were acquired in indoor conditions with luminosity around 500lux.

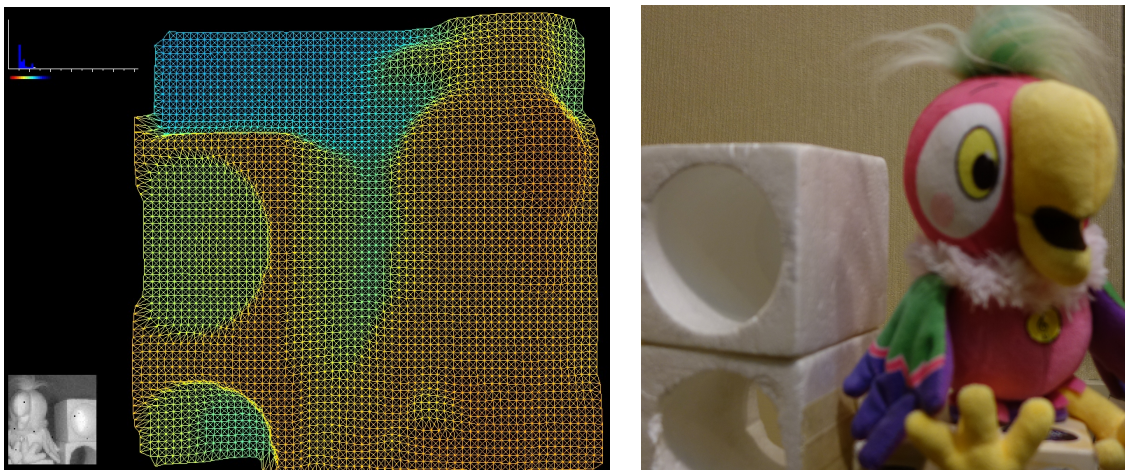

a b

Figure 6.2: Prototype examples of 3D image: a - 3D image, b - 2D image

The example of a high frame rate 3D video taken at 100 3Dfps under the same conditions follows below (Figure 6.3). The distance range is from 20cm to 80 cm and the integration time is 500us.

This video was shown during the presentation at the International Solid-State Circuit Conference in February 2013 [100]. The visualization of the video is slowed by a factor of 8 to make hitting moment more visible and to ensure good representation on a monitor, which is not capable of showing high frame rate video. In addition to the 3D video, a 2D video capturing the same scene is shown (Figure 6.4).

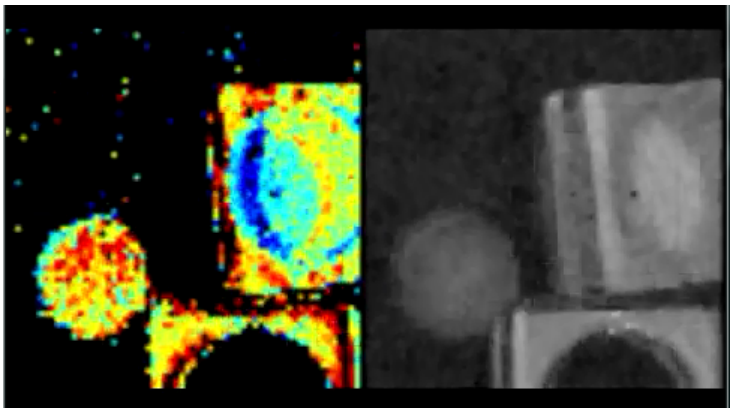

Figure 6.3: 3D video and correspondent 2D video captured with the camera prototype (In order to play video file click on the figure)

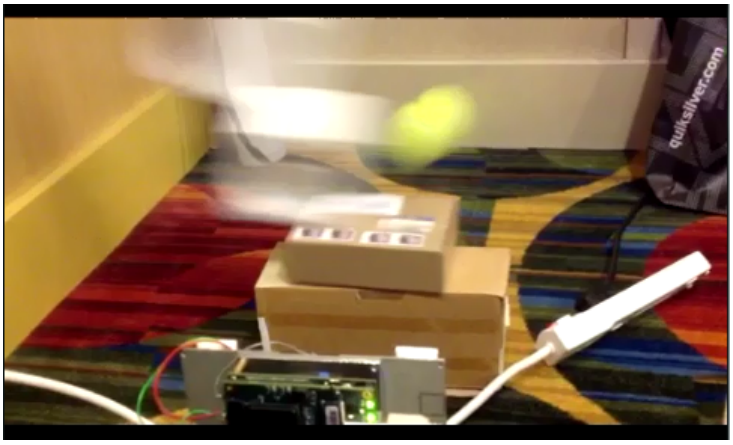

Figure 6.4: 2D video of the same scene acquired with usual camera at 25fps (In order to play video file click on the figure)

Figure 6.5: Demonstration of a video clip about 3D camera
(In order to play video file click on the figure)

An additional video clip was made about the 3D camera prototype[1], which is shown in Figure 6.5. This clip clearly visualize distance capturing with the camera. The distance range is from 30cm to 120cm. Integration time is 6ms, which corresponds to 30 3Dfps. Static objects placed at different distances cover the camera distance range. In addition, the scene includes a moving toy car with a motion amplitude of 25cm. In the last frames, showing a fast hand movement the frame rate was increased to 40 3Dfps.

[1] http://www.youtube.com/watch?v=CN5JLXOq2FY

The specification of the 3D camera prototype is summarized in Table 6.1. Figure 6.6 illustrates the complete 3D camera prototype, including a front plate in the second photograph.

Table 6.1: 3D Camera Prototype Summary

Parameter	Value
Distance measurement method	Phase-shift TOF
Detector type	CMOS Avalanche photodiode
Modulation frequency	25MHz
Illuminator type	2x2 - LED array
Illuminator wavelength	850nm
Peak optical power	< 1.8W
Objective	f=6mm,F#=1.2, S-mount
Max frame rate	120 3Dfps (limited by USB bandwidth)
Camera size	$14 \times 5 \times 6$cm
Power supply for illumination unit	12V, 500mA, nominal
Power supply for FPGA	5V, 500mA, nominal
Visualization	PC screen
Communication	via USB

Figure 6.6: 3D camera system prototype

Chapter 7

Conclusion

In this thesis a novel sensor implementation for distance measurement that can potentially lead to several improvements with respect to the state-of-the-art approaches has been proposed. The detector that can perform light sensing and demodulation required for I-TOF is a CMOS avalanche photodiode. Using the proposed approach, improvement in distance measurement precision and system power consumption can be obtained due to high bandwidth and sensitivity of an avalanche photodiode.

The successful implementation of a CMOS avalanche photodiode array is by itself the innovative aspect of this work. Together with this, application of the sensor for phase-shift Time-of-Flight measurement is also a novel approach in 3D camera systems.

The CMOS avalanche photodiode implementation for a 3D Time-of-Flight measurement can potentially improve several parameters with respect to known 3D TOF systems. Namely, high bandwidth of an avalanche photodiode for an Indirect Time-of-Flight measurement results in high applicable modulation frequency, in turn, modulation frequency has an influence on the precision in distance measurements. Next, high sensitivity of avalanche photodiodes due to the intrinsic multiplication of the signal can help to reduce the overall system power consumption, in particular to

allow us to utilize low power illumination unit, which is the main source of power consumption in the system.

7.1 Summary

In this PhD dissertation the demonstration of successful implementation of a CMOS APD sensor has been shown. The background for this implementation comes from the analysis of single pixel structures previously fabricated. Some considerations taken into account after single pixel characterization helped to improved the performance of the sensor. In particular, demodulation contrast as high as 85% was measured at 25MHz modulation frequency. Tests performed on single test pixels also included in the chip, demonstrated more than 80% demodulation contrast at 200MHz modulation frequency. The best distance precision of 1.9cm was achieved with the sensor at 2m distance. In addition, a frame rate as high as 200fps for 3D imaging was shown.

With respect to the state-of-the-art sensors our approach has demonstrated the best performance in terms of high demodulation contrast, high modulation frequency and high frame rate. Though the high frame rate can be attributed to the small sensor resolution. The precision of the sensor is comparable with the state-of-the-art sensors and can be further improved by increasing modulation frequency. The distance range can be improved by the employment of combined integration time for short and long ranges, although the maximum measured distance can only be increased by utilization of lower modulation frequency. The possible solution can be a switchable frequency mode.

After the demonstration of sufficiently good performance by the sensor, the design of a compact 3D camera prototype was considered. The design requirements and implementation have been discussed. A 3D cam-

era prototype based on the proposed approach was demonstrated at the ISSCC conference in February 2013. The camera developed in this thesis can find application in several domains, for instance, gaming, innovative user interfaces for gesture recognition, robotics in indoor environment and 3D modelling of cultural heritage. However, the improvement in certain parameters can lead to a broader expansion of the APD-based 3D camera system.

7.2 Future work

Future work can be separated into two activities, one related to 3D camera system improvement and another to investigation on the sensor side. On one hand the improvement of the camera system can be performed. For instance, the employment of IR filters will help to reject unwanted wavelengths and prevent the sensor from early saturation. This will increase camera robustness with the presence of ambient light, though might not be enough for outdoor application.

Next part that can be improved is the modulation signal distribution to the sensor. Current implementation does not allow high frequency modulation signal to reach and effectively modulate the array. In this work tests at high frequencies were performed only on a single test row. Proper coupling will reduce the loss of the high frequency signal. As a result, the ability to modulate the sensor at higher frequencies will offer not only improvement in distance measurement but also a new application in a biomedical field, where high frequency electro-optical mixers are used for fluorescence lifetime detection (FLIM) [7].

On the other hand, the investigation on the sensor side can be done. As a first step the resolution of the sensor can be increased in the same technological process. However, the increase in lateral resolution of the

sensor will enlarge the capacitive load that should be modulated, that will increase the power requirement for a driving circuit. In addition, the distribution of modulation signals should be taken in to account also inside the sensor. One possible solution to reduce APD capacitance is to shrink the size of a photodiode, however at some point the fill factor will be too small, because of guard ring size. Additional steps that can improve the performance of the sensor are implementation of DC/DC converter and ADC circuit inside the chip. That will further reduce the camera system size.

The analyses of technology scaling on the sensor performance is also of great interest as a further step. New APD structures and guard rings can be investigated, that can result in APD size reduction, hence increase in sensor resolution. Together with readout electronics size shrinking, the fill factor will benefit from technology scaling.

Bibliography

[1] David Droeschel, Dirk Holz, J Stuckler, and Sven Behnke. Using time-of-flight cameras with active gaze control for 3d collision avoidance. In *Robotics and Automation (ICRA), 2010 IEEE International Conference on*, pages 4035–4040. IEEE, 2010.

[2] Stephan Hussmann, Daniel Schauer, and Bruce MacDonald. Integration of a 3d-tof camera into an autonomous, mobile robot system. In *Instrumentation and Measurement Technology Conference, 2009. I2MTC'09. IEEE*, pages 547–552. IEEE, 2009.

[3] Cristiano Niclass, Mineki Soga, Hiroyuki Matsubara, and Satoru Kato. A 100m-range 10-frame/s 340× 96-pixel time-of-flight depth sensor in 0.18 μm cmos. In *ESSCIRC (ESSCIRC), 2011 Proceedings of the*, pages 107–110. IEEE, 2011.

[4] Sankaranarayanan Natarajan, Andreas Vogt, and Frank Kirchner. Dynamic collision avoidance for an anthropomorphic manipulator using a 3d tof camera. In *Robotics (ISR), 2010 41st International Symposium on and 2010 6th German Conference on Robotics (ROBOTIK)*, pages 1–7. VDE, 2010.

[5] Mohammadreza Asghari Oskoei and Huosheng Hu. Application of feature tracking in a vision based human machine interface for xbox. In *Robotics and Biomimetics (ROBIO), 2009 IEEE International Conference on*, pages 1738–1743. IEEE, 2009.

[6] Muhamad Risqi Utama Saputra, Guntur Dharma Putra, Paulus Insap Santosa, et al. Indoor human tracking application using multiple depth-cameras. In *Advanced Computer Science and Information Systems (ICACSIS), 2012 International Conference on*, pages 307–312. IEEE, 2012.

[7] Alessandro Esposito. Beyond range: Innovating fluorescence microscopy. *Remote Sensing*, 4(1):111–119, 2012.

[8] Francesco Ficorella, G-F Dalla Betta, L Viarani, M Perenzoni, D Stoppa, and L Gonzo. 3djam: A linear cmos sensor for 3d vision with merged i-tof and ot techniques. In *Research in Microelectronics and Electronics 2006, Ph. D.*, pages 261–264. IEEE, 2006.

[9] Lucio Pancheri, Nicola Massari, Matteo Perenzoni, Mattia Malfatti, and David Stoppa. A qvga-range image sensor based on buried-channel demodulator pixels in 0.18 μm cmos with extended dynamic range. In *Solid-State Circuits Conference Digest of Technical Papers (ISSCC), 2012 IEEE International*, pages 394–396. IEEE, 2012.

[10] François Blais. Review of 20 years of range sensor development. *Journal of Electronic Imaging*, 13(1), 2004.

[11] Shinnosuke Hirata, Minoru Kuribayashi Kurosawa, and Takashi Katagiri. Real-time ultrasonic distance measurements for autonomous mobile robots using cross correlation by single-bit signal processing. In *Robotics and Automation, 2009. ICRA'09. IEEE International Conference on*, pages 3601–3606. IEEE, 2009.

[12] Sorin Fericean, Albert Dorneich, Reinhard Droxler, and D Krater. Development of a microwave proximity sensor for industrial applications. *Sensors Journal, IEEE*, 9(7):870–876, 2009.

[13] KL Boyer and AC Kak. Color-encoded structured light for rapid active ranging. *Pattern Analysis and Machine Intelligence, IEEE Transactions on*, 1(1):14–28, 1987.

[14] Fabrizio De Nisi, Fiorenzo Comper, Lorenzo Gonzo, Massimo Gottardi, David Stoppa, Andrea Simoni, and J-A Beraldin. A cmos sensor optimized for laser spot-position detection. *Sensors Journal, IEEE*, 5(6):1296–1304, 2005.

[15] Shingo Mandai, Makoto Ikeda, and Kunihiro Asada. A 256× 256 14k range maps/s 3-d range-finding image sensor using row-parallel embedded binary. In *Solid-State Circuits Conference Digest of Technical Papers (ISSCC), 2010 IEEE International*, pages 404–405. IEEE, 2010.

[16] Primesense Kinect. (http://www.primesense.com/casestudies/kinect/).

[17] R Dändliker, Y Salvadé, and E Zimmermann. Distance measurement by multiple-wavelength interferometry. *Journal of optics*, 29(3):105, 1998.

[18] Michelson Interferometer. (https://wiki.engr.illinois.edu/display/bioe414/the+principles+behind+oct).

[19] Heliotis. (http://www.heliotis.ch/html/productsoverview.html).

[20] Brian F Aull, Andrew H Loomis, Douglas J Young, Richard M Heinrichs, Bradley J Felton, Peter J Daniels, and Deborah J Landers. Geiger-mode avalanche photodiodes for three-dimensional imaging. *Lincoln Laboratory Journal*, 13(2):335–349, 2002.

[21] Cristiano Niclass, Alexis Rochas, P-A Besse, and Edoardo Charbon. Toward a 3-d camera based on single photon avalanche diodes. *Se-*

lected Topics in Quantum Electronics, IEEE Journal of, 10(4):796–802, 2004.

[22] David Stoppa, Lucio Pancheri, Mauro Scandiuzzo, Mattia Malfatti, Gianmaria Pedretti, and Lorenzo Gonzo. A single-photon-avalanche-diode 3d imager. In *Solid-State Circuits Conference, 2005. ESSCIRC 2005. Proceedings of the 31st European*, pages 487–490. IEEE, 2005.

[23] David Stoppa, Lucio Pancheri, Mauro Scandiuzzo, Lorenzo Gonzo, Gian-Franco Dalla Betta, and Andrea Simoni. A cmos 3-d imager based on single photon avalanche diode. *Circuits and Systems I: Regular Papers, IEEE Transactions on*, 54(1):4–12, 2007.

[24] Richard J Walker, Justin A Richardson, and Robert K Henderson. A 128× 96 pixel event-driven phase-domain $\delta\sigma$-based fully digital 3d camera in 0.13 μm cmos imaging technology. In *Solid-State Circuits Conference Digest of Technical Papers (ISSCC), 2011 IEEE International*, pages 410–412. IEEE, 2011.

[25] Cristiano Niclass, Mineki Soga, Hiroyuki Matsubara, Masaru Ogawa, and Manabu Kagami. A 0.18μm cmos soc for a 100m-range 10fps 200× 96-pixel time-of-flight depth sensor. In *Solid-State Circuits Conference Digest of Technical Papers (ISSCC), 2013 IEEE International*, pages 488–489. IEEE, 2013.

[26] R Jeremias, W Brockherde, G Doemens, B Hosticka, L Listl, and P Mengel. A cmos photosensor array for 3d imaging using pulsed laser. In *Solid-State Circuits Conference, 2001. Digest of Technical Papers. ISSCC. 2001 IEEE International*, pages 252–253. IEEE, 2001.

[27] Robert Lange and Peter Seitz. Solid-state time-of-flight range camera. *Quantum Electronics, IEEE Journal of*, 37(3):390–397, 2001.

[28] G Bazin and B Journet. A new laser range-finder based on fmcw-like method. In *Instrumentation and Measurement Technology Conference, 1996. IMTC-96. Conference Proceedings.'Quality Measurements: The Indispensable Bridge between Theory and Reality'., IEEE*, volume 1, pages 90–93. IEEE, 1996.

[29] Bernard Journet and Gaëlle Bazin. A low-cost laser range finder based on an fmcw-like method. *Instrumentation and Measurement, IEEE Transactions on*, 49(4):840–843, 2000.

[30] David Dupuy and Marc Lescure. Improvement of the fmcw laser range-finder by an apd working as an optoelectronic mixer. *Instrumentation and Measurement, IEEE Transactions on*, 51(5):1010–1014, 2002.

[31] Markus-Christian Amann, Thierry Bosch, Marc Lescure, Risto Myllyla, and Marc Rioux. Laser ranging: a critical review of usual techniques for distance measurement. *Optical Engineering*, 40(1):10–19, 2001.

[32] David Dupuy, Marc Lescure, and Hélène Tap-Béteille. Analysis of an avalanche photodiode used as an optoelectronic mixer for a frequency modulated continuous wave laser range finder. *Journal of Optics A: Pure and Applied Optics*, 4(6):S332, 2002.

[33] ER Moutaye and H Tap-Beteille. Design of a cmos apd array for a 3-d camera based on the time of flight distance measurement. In *Instrumentation and Measurement Technology Conference (I2MTC), 2010 IEEE*, pages 443–446. IEEE, 2010.

[34] Thomas Spirig, Peter Seitz, Oliver Vietze, and Friedrich Heitger. The lock-in ccd-two-dimensional synchronous detection of light. *Quantum Electronics, IEEE Journal of*, 31(9):1705–1708, 1995.

[35] Ryohei Miyagawa and Takeo Kanade. Ccd-based range-finding sensor. *Electron Devices, IEEE Transactions on*, 44(10):1648–1652, 1997.

[36] Rudolf Schwarte, Zhanping Xu, Horst-Guenther Heinol, Joachim Olk, Ruediger Klein, Bernd Buxbaum, Helmut Fischer, and Juergen Schulte. New electro-optical mixing and correlating sensor: facilities and applications of the photonic mixer device (pmd). In *Lasers and Optics in Manufacturing III*, pages 245–253. International Society for Optics and Photonics, 1997.

[37] Thierry Oggier, Michael Lehmann, Rolf Kaufmann, Matthias Schweizer, Michael Richter, Peter Metzler, Graham Lang, Felix Lustenberger, and Nicolas Blanc. An all-solid-state optical range camera for 3d real-time imaging with sub-centimeter depth resolution (swissranger). In *Optical Systems Design*, pages 534–545. International Society for Optics and Photonics, 2004.

[38] Mesa Imaging. Mesa imaging (www.mesa-imaging.ch).

[39] SwissRanger^{TM} SR4000. Swissranger^{TM} sr4000 (http://www.mesa-imaging.ch/prodview4k.php).

[40] Dario Piatti and Fulvio Rinaudo. Sr-4000 and camcube3. 0 time of flight (tof) cameras: Tests and comparison. *Remote Sensing*, 4(4):1069–1089, 2012.

[41] Tobias Möller, Holger Kraft, Jochen Frey, Martin Albrecht, and Robert Lange. Robust 3d measurement with pmd sensors. *Range Imaging Day, Zürich*, 2005.

[42] PMDtechnologies gmbH. Pmdtechnologies gmbh (http://pmdtec.com/).

[43] Shaoji Kawahito, Izhal Abdul Halin, Takeo Ushinaga, Tomonari Sawada, Mitsuru Homma, and Yasunari Maeda. A cmos time-of-flight range image sensor with gates-on-field-oxide structure. *Sensors Journal, IEEE*, 7(12):1578–1586, 2007.

[44] David Stoppa, Nicola Massari, Lucio Pancheri, Mattia Malfatti, Matteo Perenzoni, and Lorenzo Gonzo. An 80× 60 range image sensor based on 10μm 50mhz lock-in pixels in 0.18 μm cmos. In *Solid-State Circuits Conference Digest of Technical Papers (ISSCC), 2010 IEEE International*, pages 406–407. IEEE, 2010.

[45] TY Lee, YJ Lee, DK Min, SH Lee, WH Kim, SH Kim, JK Jung, I Ovsiannikov, YG Jin, YD Park, et al. A 192× 108 pixel tof-3d image sensor with single-tap concentric-gate demodulation pixels in 0.13 μm technology. In *Electron Devices Meeting (IEDM), 2011 IEEE International*, pages 8–7. IEEE, 2011.

[46] Daniël Van Nieuwenhove, Ward van der Tempel, and Maarten Kuijk. Novel standard cmos detector using majority current for guiding photo-generated electrons towards detecting junctions. In *Proc. Annual Symposium of the IEEE/LEOS Benelux Chapter*, pages 229–232, 2005.

[47] Ward van der Tempel, Riemer Grootjans, Daniel Van Nieuwenhove, and Maarten Kuijk. A 1k-pixel 3d cmos sensor. In *Sensors, 2008 IEEE*, pages 1000–1003. IEEE, 2008.

[48] SoftKinetic. Softkinetic (http://www.softkinetic.com/en-us/solutions/depthsensecameras.aspx).

[49] Lucio Pancheri, David Stoppa, Nicola Massari, Mattia Malfatti, Lorenzo Gonzo, Quazi D Hossain, and Gian-Franco Dalla Betta. A

120x160 pixel cmos range image sensor based on current assisted photonic demodulators. In *SPIE Photonics Europe*, pages 772615–772615. International Society for Optics and Photonics, 2010.

[50] David Stoppa, Lucio Pancheri, Nicola Massari, Mattia Malfatti, Matteo Perenzoni, Gianmaria Pedretti, and Gian-Franco Dalla Betta. Time of flight image sensors in $0.18\mu m$ cmos technology: a comparative overview of different approaches. In *International Image Sensor Workshop (IISW),Hokkaido, Japan*, 2011.

[51] Seong-Jin Kim, Sang-Wook Han, Byongmin Kang, Keechang Lee, James DK Kim, and Chang-Yeong Kim. A three-dimensional time-of-flight cmos image sensor with pinned-photodiode pixel structure. *Electron Device Letters, IEEE*, 31(11):1272–1274, 2010.

[52] Seong-Jin Kim, James DK Kim, Sang-Wook Han, Byongmin Kang, Keechang Lee, and Chang-Yeong Kim. A 640× 480 image sensor with unified pixel architecture for 2d/3d imaging in 0.11 μm cmos. In *VLSI Circuits (VLSIC), 2011 Symposium on*, pages 92–93. IEEE, 2011.

[53] Seong-Jin Kim, Byongmin Kang, JDK Kim, Keechang Lee, Chang-Yeong Kim, and Kinam Kim. A 1920× 1080 3.65 μm-pixel 2d/3d image sensor with split and binning pixel structure in 0.11 pm standard cmos. In *Solid-State Circuits Conference Digest of Technical Papers (ISSCC), 2012 IEEE International*, pages 396–398. IEEE, 2012.

[54] Wonjoo Kim, Wang Yibing, Ilia Ovsiannikov, SeungHoon Lee, Yoondong Park, Chilhee Chung, and Eric Fossum. A 1.5 mpixel rgbz cmos image sensor for simultaneous color and range image capture. In

Solid-State Circuits Conference Digest of Technical Papers (ISSCC), 2012 IEEE International, pages 392–394. IEEE, 2012.

[55] B Buttgen, Felix Lustenberger, and Peter Seitz. Demodulation pixel based on static drift fields. *Electron Devices, IEEE Transactions on*, 53(11):2741–2747, 2006.

[56] Hamamatsu Photon. Si apd, s5343 to s5345, s9073 to s9075 (http://www.hamamatsu.com).

[57] Roland H Haitz. Studies on optical coupling between silicon p-n junctions. *Solid-State Electronics*, 8(4):417–425, 1965.

[58] Alice Biber, Peter Seitz, and Heinz Jäckel. Avalanche photodiode image sensor in standard silicon bicmos technology. *Sensors and Actuators A: Physical*, 90(1):82–88, 2001.

[59] S Cova, M Ghioni, A Lacaita, C Samori, and F Zappa. Avalanche photodiodes and quenching circuits for single-photon detection. *Applied optics*, 35(12):1956–1976, 1996.

[60] S Cova, A Longoni, and A Andreoni. Towards picosecond resolution with single-photon avalanche diodes. *Review of Scientific Instruments*, 52(3):408–412, 1981.

[61] Alexis Rochas, Alexandre R Pauchard, P-A Besse, Dragan Pantic, Zoran Prijic, and Rade S Popovic. Low-noise silicon avalanche photodiodes fabricated in conventional cmos technologies. *Electron Devices, IEEE Transactions on*, 49(3):387–394, 2002.

[62] S Cova, M Ghioni, A Lotito, I Rech, and F Zappa. Evolution and prospects for single-photon avalanche diodes and quenching circuits. *Journal of Modern Optics*, 51(9-10):1267–1288, 2004.

[63] S Tisa, A Tosi, and F Zappa. Fully-integrated cmos single photon counter. *Optics Express*, 15(6):2873–2887, 2007.

[64] Simon M Sze and Kwok K Ng. *Physics of semiconductor devices*. Wiley-interscience, 2006.

[65] George M Williams and Andrew S Huntington. Probabilistic analysis of linear mode vs. geiger mode apd fpas for advanced ladar enabled interceptors. In *Proceedings of SPIE*, volume 6220, pages 85–98, 2006.

[66] RJ McIntyre. Multiplication noise in uniform avalanche diodes. *Electron Devices, IEEE Transactions on*, 13(1):164–168, 1966.

[67] RJ McIntyre. Recent developments in silicon avalanche photodiodes. *Measurement*, 3(4):146–152, 1985.

[68] Christopher J Stapels, Michael R Squillante, William G Lawrence, Frank L Augustine, and James F Christian. Cmos-based avalanche photodiodes for direct particle detection. *Nuclear Instruments and Methods in Physics Research Section A: Accelerators, Spectrometers, Detectors and Associated Equipment*, 579(1):94–98, 2007.

[69] Young Soo Kim, In Sub Jun, and Kwang Hyun Kim. Design and characterization of cmos avalanche photodiode with charge sensitive preamplifier. *Nuclear Science, IEEE Transactions on*, 55(3):1376–1380, 2008.

[70] Gian-Franco Dalla Betta, Lucio Pancheri, and David Stoppa. High-sensitivity photodetectors in cmos technology for 3-d imaging. In *IEEE Lasers and Electro-Optics Society, 2008. LEOS 2008. 21st Annual Meeting of the*, pages 354–355. IEEE, 2008.

[71] Lucio Pancheri, Mauro Scandiuzzo, David Stoppa, and Gian-Franco Dalla Betta. Low-noise avalanche photodiode in standard 0.35-

μm cmos technology. *Electron Devices, IEEE Transactions on*, 55(1):457–461, 2008.

[72] Toshiyuki Shimotori, Kazuaki Maekita, Takeo Maruyama, and Koichi Iiyama. Characterization of apds fabricated by 0.18 μm cmos process in blue wavelength region. In *Opto-Electronics and Communications Conference (OECC), 2012 17th*, pages 509–510. IEEE, 2012.

[73] Myung-Jae Lee and Woo-Young Choi. A silicon avalanche photodetector fabricated with standard cmos technology with over 1 thz gain-bandwidth product. *Optics Express*, 18(23):24189–24194, 2010.

[74] Mohamed Atef, H Zimmermann, et al. Avalanche double photodiode in 40nm standard cmos technology. *Quantum Electronics, IEEE Journal of*, 49(3):350–356, 2013.

[75] Majeed M Hayat, Winslow L Sargeant, and Bahaa EA Saleh. Effect of dead space on gain and noise in si and gaas avalanche photodiodes. *Quantum Electronics, IEEE Journal of*, 28(5):1360–1365, 1992.

[76] G. A. M. Hurkx, D. B. M. Klaassen, and M. P. G. Knuvers. A new recombination model for device simulation including tunneling. *Electron Devices, IEEE Transactions on*, 39(2):331–338, 1992.

[77] B. Ciftcioglu, Jie Zhang, Lin Zhang, J.R. Marciante, J.D. Zuegel, R. Sobolewski, and Hui Wu. 3-ghz silicon photodiodes integrated in a 0.18-um cmos technology. *Photonics Technology Letters, IEEE*, 20(24):2069–2071, 2008.

[78] Koichi Iiyama, Hideki Takamatsu, and Takeo Maruyama. Hole-injection-type and electron-injection-type silicon avalanche photodi-

odes fabricated by standard $0.18\mu m$ cmos process. *Photonics Technology Letters, IEEE*, 22(12):932–934, 2010.

[79] Myung-Jae Lee, Holger Rucker, and Woo-Young Choi. Effects of guard-ring structures on the performance of silicon avalanche photodetectors fabricated with standard cmos technology. *Electron Device Letters, IEEE*, 33(1):80–82, 2012.

[80] Ehsan Kamrani, Frederic Lesage, and Mohamad Sawan. Premature edge breakdown prevention techniques in cmos apd fabrication. In *New Circuits and Systems Conference (NEWCAS), 2012 IEEE 10th International*, pages 345–348. IEEE, 2012.

[81] Gian-Franco Dalla Betta, Lucio Pancheri, David Stoppa, Robert Henderson, and Justin Richardson. *Avalanche Photodiodes in Submicron CMOS Technologies for High-Sensitivity Imaging*, pages 226–248. in Advances in Photodiodes, IntechOpen, 2011.

[82] Robert Lange. *3D time-of-flight distance measurement with custom solid-state image sensors in CMOS/CCD-technology.* PhD thesis, Universitätsbibliothek, 2000.

[83] Examples:. Mesa imaging (www.mesa-imaging.ch) pmd technologies (www.pmdtec.com) softkinetic (www.softkinetic.com) panasonic (www.pewa.panasonic.com/components/built-in-sensors/3d-image-sensors/d-imager/).

[84] Robert Lange, Peter Seitz, Alice Biber, and Stefan Lauxtermann. Demodulation pixels in ccd and cmos technologies for time-of-flight ranging. In *Proc. SPIE*, volume 3965, pages 177–188, 2000.

[85] Peter Gulden, Martin Vossiek, Patric Heide, and Rudolf Schwarte. Novel opportunities for optical level gauging and 3d-imaging with the

photoelectronic mixing device. *Instrumentation and Measurement, IEEE Transactions on*, 51(4):679–684, 2002.

[86] David Stoppa, Nicola Massari, Lucio Pancheri, Mattia Malfatti, Matteo Perenzoni, and Lorenzo Gonzo. A range image sensor based on 10-μm lock-in pixels in 0.18-μm cmos imaging technology. *IEEE journal of solid-state circuits*, 46(1):248–258, 2011.

[87] Danil Van Nieuwenhove, Ward van der Tempel, Riemer Grootjans, Johan Stiens, and Maarten Kuijk. Photonic demodulator with sensitivity control. *Sensors journal, IEEE*, 7(3):317–318, 2007.

[88] Cristiano Niclass, Claudio Favi, Theo Kluter, Frédéric Monnier, and Edoardo Charbon. Single-photon synchronous detection. *Solid-State Circuits, IEEE Journal of*, 44(7):1977–1989, 2009.

[89] Gerald Zach, Milos Davidovic, and Horst Zimmermann. A 16× 16 pixel distance sensor with in-pixel circuitry that tolerates 150 klx of ambient light. *IEEE journal of solid-state circuits*, 45(7):1345–1353, 2010.

[90] Matteo Perenzoni, Nicola Massari, David Stoppa, Lucio Pancheri, Mattia Malfatti, and Lorenzo Gonzo. A 160× 120-pixels range camera with on-pixel correlated double sampling and nonuniformity correction in 29.1 μm pitch. In *ESSCIRC, 2010 Proceedings of the*, pages 294–297. IEEE, 2010.

[91] A Esposito, T Oggier, HC Gerritsen, F Lustenberger, and FS Wouters. All-solid-state lock-in imaging for wide-field fluorescence lifetime sensing. *Opt. Express*, 13(24):9812–9821, 2005.

[92] D Dupuy, M Lescure, and M Cousineau. A fmcw laser range-finder based on a delay line technique. In *Instrumentation and Measurement*

Technology Conference, 2001. IMTC 2001. Proceedings of the 18th IEEE, volume 2, pages 1084–1088. IEEE, 2001.

[93] Cadence website [Online]. Available: www.cadence.com.

[94] Elisabetta Mazzuca. Caratterizzazione di fotodiodi a valanga realizzati in tecnologia cmos e progetto di un relativo circuito di lettura. Master's thesis, Tesi di Laurea Specialistica in Ingegneria delle Telecomunicazioni, University of Trento, 2008.

[95] Roberto Mittempergher. Caratterizzazione di pixel attivi cmos basati su fotodiodi a valanga e amplificatori di carica. *Bachelor thesis, Tesi di Laurea in Ingegneria delle Telecomunicazioni, University of Trento, 2010.*

[96] Behzad Razavi. Design of analog cmos integrated circuits. *McGraw-Hill, New York, NY*, 2001.

[97] Labview website [Online]. Available: www.ni.com/labview/.

[98] Justin A Richardson, Eric AG Webster, Lindsay A Grant, and Robert K Henderson. Scaleable single-photon avalanche diode structures in nanometer cmos technology. *Electron Devices, IEEE Transactions on*, 58(7):2028–2035, 2011.

[99] Opal Kelly XEM3050 website [Online]. Available: http://www.opalkelly.com/products/xem3050/.

[100] ISSCC 2013 program website [Online]. Available: http://www.miracd.com/isscc2013/webap/.